Western Graduate&PostdoctoralStudies

Western University
Scholarship@Western

Electronic Thesis and Dissertation Repository

8-12-2015 12:00 AM

Development of a small animal conformal irradiator with dual energy x-ray computed tomography imaging for kilovoltage dosimetry

Michael D. Jensen
The University of Western Ontario

Supervisor
Eugene Wong
The University of Western Ontario

Graduate Program in Medical Biophysics
A thesis submitted in partial fulfillment of the requirements for the degree in Doctor of Philosophy
© Michael D. Jensen 2015

Follow this and additional works at: https://ir.lib.uwo.ca/etd

Part of the Medical Biophysics Commons, Oncology Commons, and the Other Physics Commons

Recommended Citation

Jensen, Michael D., "Development of a small animal conformal irradiator with dual energy x-ray computed tomography imaging for kilovoltage dosimetry" (2015). *Electronic Thesis and Dissertation Repository*. 3046.
https://ir.lib.uwo.ca/etd/3046

This Dissertation/Thesis is brought to you for free and open access by Scholarship@Western. It has been accepted for inclusion in Electronic Thesis and Dissertation Repository by an authorized administrator of Scholarship@Western. For more information, please contact wlswadmin@uwo.ca.

DEVELOPMENT OF A SMALL ANIMAL CONFORMAL IRRADIATOR WITH DUAL ENERGY X-RAY COMPUTED TOMOGRAPHY IMAGING FOR KILOVOLTAGE DOSIMETRY

(Thesis format: Integrated Article)

by

Michael David Jensen

Graduate Program in Medical Biophyics

A thesis submitted in partial fulfillment
of the requirements for the degree of
Doctor of Philosophy

The School of Graduate and Postdoctoral Studies
The University of Western Ontario
London, Ontario, Canada

© Michael David Jensen 2015

Abstract

External beam radiotherapy has become technically sophisticated with image guided radiation therapy (IGRT) and intensity modulated radiation therapy (IMRT). These technologies allow for precise delivery of radiation to geometric targets in cancer patients. However, many questions remain on how to best define targets based on biological information, such as functional imaging, and how to combine radiation with other cancer therapies. To help answer these questions, small animal preclinical studies are needed to generate data to inform clinical trials. However, the precise radiation delivery capabilities of IGRT and IMRT have not been available in the preclinical labs. To enable translational experiments and to address the lack of preclinical radiotherapy technology, a commercial micro-CT was first developed into an image-guided conformal radiotherapy system in this thesis. Computerized asymmetric jaws were constructed, implemented and characterized for the system. A Monte Carlo dose calculation package was successfully configured for the system and verified with film measurements. Respiratory gated imaging and radiotherapy was demonstrated with a phantom and in animals. Secondly, accurate radiation dosimetry reduces uncertainties in preclinical experiments. To achieve accurate dose calculations in the kilovoltage x-ray range where photoelectric effects and Compton scattering dominate, knowledge of material composition and density is needed. Dual energy micro-CT was optimized (including choice of x-ray beam peak voltages, filtrations, and duration) and evaluated for the purpose of characterizing materials. Dual energy CT techniques developed for clinical scanners were adapted and examined for micro-CT. A set of micro-CT phantoms consisting of 11 plastic materials and solutions that spanned a relevant range of compositions was designed and constructed. Initial experiments found beam-hardening image artefacts limited accurate measurements. By switching to a more sensitive detector, x-ray spectra with additional beam filtration were possible and resulted in reduced beam-hardening effects. This improved dual energy micro-CT measurement accuracy of material composition and density. In conclusion, a small animal image-guided conformal radiotherapy system was developed and commissioned for preclinical studies. Dual energy micro-CT was demonstrated as a method to

characterize materials to improve kilovoltage dose calculation. This integrated micro-CT based small animal image-guided radiation platform has enabled numerous pre-clinical studies.

Keywords: Small animal image-guided radiation therapy, dual-energy x-ray micro-computed tomography, micro-CT

Co-Authorship Statement

This thesis contains material from manuscripts that were previously published. The copyright(s) agreements for these publications are provided in Appendix D: Permission to Reproduce Previously Published Materials.

This thesis contains two manuscripts published in scientific journals, and two manuscripts in preparation. Chapter 2 and appendix A together are an original manuscript entitled "Implementation and commissioning of an integrated micro-CT/RT system with computerized independent jaw collimation", and was published in the journal *Medical Physics* in July 2013. The manuscript was coauthored by M. D. Jensen, W. T. Hrinivich, J. A. Jung, D. W. Holdworth, M. Drangova, J. Chen and E. Wong. Chapter 3 is an original manuscript entitled "Determination of effective atomic numbers and electron densities with dual energy micro-CT measurements". The manuscript was coauthored by M. D. Jensen, J. Chen and E. Wong. Chapter 4 is an original manuscript entitled "Improved determination of effective atomic numbers and electron densities using dual energy micro-CT with optimized spectra and CMOS panel detector". The manuscript was coauthored by M. D. Jensen, S. Dawson, J. Chen and E. Wong. Appendix C is an original manuscript entitled "Study of the IMRT interplay effect using 4DCT Monte Carlo dose calculation", and was published in the journal *Physics in Medicine and Biology* in April 2012. The manuscript was coauthored by M. D. Jensen, A. Abdellatif, J. Chen and E. Wong.

As the principal author and PhD candidate, Michael D. Jensen contributed to the design, assembly and installation of experimental equipment developed in the thesis (collimator, phantoms, beam filters, phantoms), and the development of the corresponding control and analysis software. Additionally, M. D. Jensen acquired phantom and small animal data, performed data and statistical analysis, led interpretation of results, drafted manuscripts, and revised manuscripts for publication in response to reviews. Dr. E. Wong, as the principal author's supervisor, helped to determine the project objectives, provided mentorship, consulted on interpretation of results, provided editorial assistance and overall guidance. Dr. J. Chen consulted on interpretation of results, provided editorial assistance and overall guidance. Dr. M. Dran-

gova and Dr. D. W. Holdsworth provided expertise and editorial assistance for the manuscript they co-authored. W. T. Hrinivich and J. A. Jung assisted in film dosimetry (acquisition and analysis) and contributed editorial assistance on the manuscript they co-authored. S. Dawson assisted in spectral optimization and data acquisition and contributed editorial assistance on the manuscript she co-authored. A. Abdellatif assisted in data acquisition and contributed editorial assistance on the manuscript he co-authored.

Dedication

To my parents, David and Doris.

Acknowledgements

Part of the research presented in this thesis was funded by a Canadian Cancer Society Research Institute Grant (No. 700386) and/or a London Regional Cancer Program Small Grant Award. The micro-CT was funded by the Canadian Foundation for Innovation. The work presented in appendix C was supported by a complimentary license for NXEGS 1.12 provided by NX Medical Software LLC. Bryan Delodder and James J. Miller of Teledyne DALSA are recognised for providing a demonstration CMOS detector and technical assistance. Vladimir Varchena of CIRS Inc. is acknowledged for providing phantom composition data.

I am appreciative for the financial support I have received during my graduate career at Western. I acknowledge support from a Canadian Institute of Health Research Student Training Program Award (2009–2010), an Ontario Graduate Scholarship in Science and Technology (2010–2011), and a Schulich Graduate Scholarship, Department of Medical Biophysics (2008–2013).

The road to this thesis has had many hills and valleys, twists and turns. Along the journey, I've been fortunate to receive support and assistance from many people that has been instrumental to this work.

To my supervisor, Dr. Eugene Wong–thank you for your support, guidance and encouragement.

I thank my advisory committee members, Dr. Ting-Yim Lee and Dr. Giles Santyr, for their insight, expertise, advice, resources, and allowing me to learn from their research groups. I thank Drs. Jerry Battista and Grace Parraga for providing advice, writing support, and feedback during the drafting of this thesis. To Dr. Jeff Chen–thank you for your insight, expertise and advice. To Drs. David Holdsworth and Maria Drangova–thank you for expertise and insight, as well as your generosity in sharing tools, materials, and lab space. I thank Dr. Tamie Poepping for providing me with desk and lab space during a summer of Physics and Astronomy Building renovations. I thank Dr. Paula Foster for providing wet lab facilities and materials and Dr. Tim Scholl for MRI resources and support.

I wish to thank Frank Van Sas and Brian Dalrymple for constructing the collimator, beam filter wheel and other miscellaneous components from my (vague) drawings. I thank Marty Classens for machining the solid water phantoms. Thanks to Doug Hie for assistance with electronics and purchasing, as well as thanks to Phin Perquin for purchasing and shipping assistance. I thank Joseph Umoh and Hristo Nikolov for assistance with micro-CT issues and phantoms. Thanks to Yuhua Chen for helping me in Dr. Foster's lab. I thank Wendy Hough and Barb Barons for helping me through the paperwork.

I thank Del Archer for collaboration on creating and modifying micro-CT/RT software and the opportunity to commercialize a version of the collimator developed in this thesis. I thank Jeremy Gill for his assistance with micro-CT software and debugging. Thanks to Mike Cole for his expertise and skill in repairing and debugging the micro-CT.

I thank Jean-Guy Belliveau, Heeseung (Patrick) Lim, Elaine Hegarty, Donna Murrell, Kundan Thind and Niloufar Zarghami for trusting a portion of their projects to the micro-CT/RT, and for their patience when I struggled to keep the system running. Additional thanks to Elaine and Niloufar for assistance with animal handling and histology, and Patrick for the hyperpolarized MRI pilot experiment.

I thank the past and present members of the Wong lab: Ady Abdellatif, Jeff Craig, Doug Hoover, Tom Hrinivich, Nikolaj Jensen, Anthony Lausch, Iram Munawar, Mike Oliver, Bon Ryu and Niloufar Zarghami. I've been fortunate to work and learn alongside you. Thank you to Jongho (Andrew) Jung and Sarah Dawson for their contributions to the manuscripts.

Finally, thank you to my family and friends for their patience, understanding and support.

Contents

Abstract ii

Co-Authorship Statement iv

Dedication vi

Acknowlegements vii

Contents ix

List of Figures xiv

List of Tables xxi

List of Appendices xxiii

List of Abbreviations, Symbols, and Nomenclature xxiv

1 Introduction 1

1.1 Cancer . . . 1
1.2 Treatments for Cancer . . . 1
1.3 Development of radiation therapy . . . 2
1.3.1 Image guidance in radiation therapy . . . 3
1.3.2 Intensity modulation in radiation therapy (IMRT) . . . 6
1.4 Next generation radiotherapy: biological targeting . . . 7
1.5 Benefits of preclinical irradiation studies . . . 7
1.6 Current small animal irradiator technology . . . 9
1.6.1 Whole body irradiators (x-ray, radionuclide) . . . 9
1.6.2 Image guided conformal irradiators . . . 10
1.6.2.1 Small Animal Radiation Research Platform (SARRP) . . . 10
1.6.2.2 Toronto System . . . 13
1.6.2.3 Maastricht System . . . 14
1.6.2.4 Stanford System . . . 14
1.6.3 Current challenges in small animal irradiation . . . 16
1.6.3.1 Conformity, intensity modulation, planning . . . 16
1.6.3.2 Dose calculation with kV energies . . . 17
1.7 Dual-Energy Computed Tomography . . . 19

1.8 Research Goals and Objectives 19
1.9 Thesis Outline 20
1.9.1 Chapter 2: Implementation and commissioning of an integrated micro-CT/RT system with computerized independent jaw collimation 20
1.9.2 Chapter 3: Determination of effective atomic numbers and electron densities with dual energy micro-CT measurements 20
1.9.3 Chapter 4: Improved determination of effective atomic numbers and electron densities using dual energy micro-CT with optimized spectra and a CMOS panel detector 21
1.9.4 Chapter 5: Conclusions 21
1.10 References 22

2 Implementation and commissioning of an integrated micro-CT/RT system with computerized independent jaw collimation 27
2.1 Introduction 27
2.2 Materials and Methods 29
2.2.1 General design considerations 29
2.2.2 Hardware 30
2.2.2.1 Micro-CT/RT 30
2.2.2.2 Collimator 30
2.2.3 Software 32
2.2.4 System calibration and performance characterization 32
2.2.4.1 Jaw position calibration and accuracy assessment 33
2.2.5 Dosimetry 34
2.2.5.1 Measurements 34
2.2.5.1.1 Exposure settings 34
2.2.5.1.2 Jaw Transmission 34
2.2.5.1.3 Output 34
2.2.5.1.4 Radiochromic film processing 34
2.2.5.1.5 Absolute depth dose 35
2.2.5.1.6 Beam profiles 35
2.2.5.1.7 Beam profile with asymmetric field 35
2.2.5.2 Monte Carlo modeling 36
2.2.5.3 Focal spot size 36
2.2.6 Elliptical target 36
2.2.7 Image guidance 37
2.2.8 Respiratory gating 37
2.2.8.1 Example animal IGRT 38
2.3 Results 40
2.3.1 Collimator performance 40
2.3.2 Dosimetry 41
2.3.2.1 Output 41
2.3.2.2 Absolute depth dose 42
2.3.2.3 Beam profiles 42
2.3.2.4 Asymmetric field beam profile 43

2.3.2.5 Focal spot size . . . 45
2.3.3 Elliptical target . . . 45
2.3.4 Image guidance . . . 45
2.3.5 Gating . . . 45
2.3.6 Example animal IGRT . . . 47
2.4 Discussion . . . 48
2.5 Conclusion . . . 54
2.6 References . . . 55

3 Determination of effective atomic numbers and electron densities with dual energy micro-CT measurements 58
3.1 Introduction . . . 58
3.2 Methods . . . 61
3.2.1 Micro-CT scanner and image acquisition . . . 61
3.2.2 Dual energy computed tomography algorithm . . . 62
3.2.3 DECT scanning objects . . . 62
3.2.3.1 CIRS and Gammex phantom inserts . . . 62
3.2.3.2 Micro-CT specific plastics and solution phantoms . . . 62
3.2.3.2.1 Plastics phantom design . . . 65
3.2.3.2.2 Solution phantom design . . . 65
3.2.4 Small animal . . . 68
3.2.5 Comparison with theoretical values . . . 68
3.2.5.1 Impact of imaging artefacts (systematic uncertainties) . . . 68
3.2.5.2 Impact of imaging noise (random uncertainties) . . . 69
3.2.6 DECT for small animal . . . 69
3.3 Results . . . 69
3.3.1 Phantom scans . . . 69
3.3.1.1 Imaging arefacts . . . 76
3.3.1.2 Imaging noise . . . 77
3.3.2 Small animal scan . . . 78
3.4 Discussion . . . 78
3.5 Conclusion . . . 81
3.6 References . . . 82

4 Improved determination of effective atomic numbers and electron densities using dual energy micro-CT with optimized spectra and CMOS panel detector 84
4.1 Introduction . . . 84
4.2 Methods . . . 87
4.2.1 Micro-CT Hardware . . . 87
4.2.2 Spectrum Optimization (kVp, mAs and filter choice) . . . 87
4.2.3 Scanning protocols . . . 88
4.2.4 Image reconstruction and preprocessing . . . 89
4.2.4.1 Virtual monoenergetic image reconstruction . . . 89
4.2.5 Test materials . . . 90
4.2.6 Algorithms . . . 91

4.2.6.1 Definition of effective atomic number 91
4.2.6.2 Spectral based DECT method 91
4.2.6.3 Empirical polynomial fit DECT method 91
4.2.7 Analysis 92
4.2.7.1 Comparison of CMOS panel detector and optimized spectra with CCD detector 92
4.2.7.2 Comparison of polyenergetic images with virtual monoenergetic images 93
4.3 Results 93
4.3.1 Spectral Optimization 93
4.3.2 CMOS versus CCD with polyenergetic images and polynomial fit DECT method 97
4.3.3 Polynomial versus spectral fit DECT methods 97
4.3.4 CMOS monoenergetic versus polyenergetic; spectral versus polynomial fit DECT method 98
4.3.5 Beam hardening 100
4.4 Discussion 100
4.5 Conclusion 103
4.6 References 104

5 Conclusion and Future Work 107
5.1 Overview and Summary 107
5.2 Summary of conclusions 111
5.3 Limitations 111
5.4 Future Work 114
5.4.1 CMOS detector 114
5.4.2 Small animal tissue characterization 114
5.4.3 Inverse planning 115
5.4.4 Gated radiotherapy 115
5.4.5 Potential preclinical studies 116
5.5 Impact and Significance 117
5.6 References 117

Appendices 120

A Film processing details 120
A.1 Film processing 120
A.2 References 123

B Dual energy algorithms 124
B.1 Theoretical effective atomic number 124
B.2 Reduced Hounsfield unit 125
B.3 Spectral based DECT method 125
B.4 Empirical polynomial fit DECT method 126
B.5 References 127

C Study of the IMRT interplay effect using 4DCT Monte Carlo dose calculation 129
C.1 Introduction 129
C.2 Methods 131
C.2.1 Phantom, contours, IMRT plan and 4DCT acquisition 132
C.2.2 Delivery of treatment 135
C.2.3 Simulation of treatment 135
C.2.3.1 Log file processing 135
C.2.3.2 4DCT image phases 136
C.2.3.3 Monte Carlo dose calculations 136
C.2.4 Analysis 137
C.3 Results 137
C.4 Discussion 138
C.5 Conclusion 142
C.6 References 142

D Permission to Reproduce Previously Published Materials 145

E Animal Ethics Approval 162

Curriculum Vitae 165

List of Figures

1.1 Photo of a modern linear accelerator (linac) equipped with kilovoltage onboard x-ray imaging (∗), electronic portal dosimeter (megavoltage imaging) (†) and multileaf collimator (‡). All imaging components are retracted in (a). Imaging devices are all extended around a mock patient in (b). The multileaf collimator can produce many complex shapes, including letters (c) 3

1.2 Digitally reconstructed radiographs derived from CT used in treatment planning compared with projection kV images acquired prior to a therapy session. The anterior and lateral views are used to correct patient positioning by aligning skeletal or target landmarks in all dimensions. Courtesy Dr. J. Chen. 4

1.3 The planning CT image (lighter) is compared with the cone beam CT (darker). The cone beam CT acquired prior to treatment (using the onboard kilovoltage x-ray system) is aligned or registered with the planning CT to correct the patient position using both skeletal and soft tissue features. Courtesy Dr. J. Chen. . . . 5

1.4 Intensity Modulated Radiation Therapy (IMRT) treatment plan for a head and neck cancer patient displayed with transverse (a), coronal (b) and sagittal (c) views. Dose is displayed as a colourwash overlaid on the CT images. The three concave targets surrounding the brain stem are treated to different dose levels using intensity modulation and multiple beam directions. Concurrently, the dose is minimized to healthy organs, such as the brain, brain stem, spinal cord, parotid gland and mandible. Scale bar is 2 cm. Sample IMRT plan data from the Computational Environment for Radiotherapy Research (CERR) www.cerr.info 6

1.5 Example DCE-CT blood flow images of a subcutaneous xenograft hypovascular human colon tumour (LoVo) treated with an anti-angiogenic drug (Vandetanib) and followed for 6 days. A reduction in the blood flow in the rim of the tumour is observed over the treatment period (white arrow). Courtesy Drs. J. H. Tai and T.-Y. Lee 8

1.6 Irradiation of the right lung of a rat with a cobalt-60 source from below at the London Regional Cancer Program. The rat was anesthetized with isoflurane and held in a restraint box above the beam aperture. A radiochromic film was placed on the rat (yellow) to verify the radiation field location after irradiation (black semi-circle). Two parallel-opposed beams were delivered by first irradiating the animal in the prone position (a) and then rotating the restraint box so the rat was in the supine position (b). Photo credit: Dr. E. Wong. 9

1.7 The first version of the SARRP system. "Small animal radiation research platform (SARRP) with conformal irradiation and cone-beam computed tomography guidance capabilities. Maximal extent of system measures 3 ft. wide, 4 ft. long, and 6 ft. tall. It is equipped with wheels for ease of transport but rests on stops for stationary use. Camera-based electronic imaging system has since been replaced with a 21-cm × 21-cm flat panel amorphous silicon detector." Reprinted from Int. J. Radiat. Oncol. Biol. Phys., **71**(5), J. Wong, E. Armour, P. Kazanzides, I. Iordachita, E. Tryggestad, H. Deng, M. Matinfar, C. Kennedy, Z. Liu, T. Chan, O. Gray, F. Verhaegen, T. McNutt, E. Ford, and T. L. DeWeese, "High-Resolution, Small Animal Radiation Research Platform With X-Ray Tomographic Guidance Capabilities", 1591–1599, Copyright (2008), with permission from Elsevier. doi:10.1016/j.ijrobp.2008.04.025 12

1.8 "Pictures of the micro-IGRT (X-Rad 225Cx) unit. (a) The exterior of the self-shielded cabinet. (b) Interior, showing the C-arm setup with collimator and 3D linear translation stage. (c) Geometry of the system, with d_{SAD} = 30.7 cm, d_{SDD} = 64.5 cm, and d_{SCD} = 23 cm. The primary beam is collimated to cover the entire detector surface ($D_{width} \times D_{length}$ = 20.4 × 20.4 cm^2), giving a FOV_z = FOV_{xy} = 9.7 cm." Reprinted with permission from R. Clarkson, P. E. Lindsay, S. Ansell, G. Wilson, S. Jelveh, R. P. Hill, and D. A. Jaffray, Med. Phys. **38**, 845–856 (2011). Copyright 2011, American Association of Physicists in Medicine. doi:10.1118/1.3533947 13

1.9 Computerized collimator of the Stanford micro-CT/RT system. "The variable-aperture collimator in the microCT/RT system uses two disks with hexagonal shape that open and close like an iris camera. The disks are rotated 30° one with respect to the other to form a field of dodecagonal shape." Reprinted from Phys. Med. Biol. **54** (2009) 3723–3740, M. Rodriguez, H. Zhou, P. Keall, and E. Graves, "Commissioning of a novel microCT/RT system for small animal conformal radiotherapy", © Institute of Physics and Engineering in Medicine. Reproduced by permission of IOP Publishing. All rights reserved. doi:10.1088/0031-9155/54/12/008 15

1.10 Collimators for the SARRP system. "(a) Tertiary brass collimation inserts with dimensions of 30 mm × 30 mm, 3 mm × 3 mm, and 0.5 mm diameter for small animal radiation research platform. (b) Radiosurgery-like collimating cone assembly attached to primary collimator of the small animal radiation research platform for small field irradiation (<5 mm × 5 mm in dimension)." Reprinted from Int. J. Radiat. Oncol. Biol. Phys., **71**(5), J. Wong, E. Armour, P. Kazanzides, I. Iordachita, E. Tryggestad, H. Deng, M. Matinfar, C. Kennedy, Z. Liu, T. Chan, O. Gray, F. Verhaegen, T. McNutt, E. Ford, and T. L. DeWeese, "High-Resolution, Small Animal Radiation Research Platform With X-Ray Tomographic Guidance Capabilities", 1591–1599, Copyright (2008), with permission from Elsevier. doi:10.1016/j.ijrobp.2008.04.025 16

1.11 Mass Energy-Absorption Coefficient (MEAC) for three ICRU-44 tissues: adipose, skeletal muscle and cortical bone. The MEAC is closely related to absorbed radiation dose. At kilovoltage energies below 225 kVp the MEAC differs between the three tissues due to photoelectric absorption, which is dependent on the chemical composition of the tissue. To calculate the dose accurately at kilovoltage energies, both the density and chemical composition of the tissue is needed. For comparison, at the cobalt-60 energies, the MEAC differs little between the three tissue types and only density information is needed. The chemical composition has negligible effect on the dose at megavoltage energies. Data from Hubbell and Seltzer. 18

2.1 CAD rendering of the computer controlled collimator (a). Photo of the jaws mounted on the Micro-CT bore (b). X1 jaw motor and position encoder are visible in lower right of the figure. Y jaw rack and pinion motor drive is visible in upper right of the figure. Photo of micro-CT gantry before collimator installation (c). The collimator mounts onto the micro-CT bore, sitting above the detector assembly. The support electronics mount onto the gantry. 31

2.2 Sample of the respiratory waveform and gating window produced by the small animal monitoring system. Inspiration coincides with the valleys in the waveform. Shown at the top is the ungated x-ray exposure protocol of 25 ms pulses separated by 220 ms. For a gated delivery the exposure is triggered by the beginning of the gated window. The exposure duration is chosen to achieve close to a 10 percent duty cycle. For this figure, the respiration period is approximately 1080 ms, with an exposure duration of 125 ms. 39

2.3 Motion phantom used to test respiratory gating functionality. A speed adjustable rotating cam causes a platform to move sinusoidally, with a solid water block and radiochromic film. Simultaneously, an elastic band is stretched, compressing the small animal respiratory pillow creating the gating signal for the micro-CT scanner. 39

2.4 Relative output factors for field sizes ranging from 2×2 to 60×60 mm^2 as measured with EBT2 film (+) and ion chamber (o), and calculated by Monte Carlo (–×–) (a). All measurements were normalized to the 50×50 mm^2 field. Error bars for the film are shown. Absolute depth dose in solid water, EBT2 Film and Monte Carlo, for square fields of size 2, 20 and 40 mm^2 (b). Film dose is shown as solid lines with error bars; Monte Carlo dose is shown as dashed lines. 41

2.5 Beam profiles at 12 mm depth in a $70 \times 70 \times 22$ mm^3 solid water block. Film profiles have been normalized to ion chamber scaled Monte Carlo. Left-Right (a) and Superior-Inferior (b) profiles of a 40×40 mm^2 field. Left-Right (c) and Superior-Inferior (d) profiles of a 5×5 mm^2 field. Left-Right (e) and Superior-Inferior (f) profiles of a 10×10 mm^2 field, offset from the central axis by 25 mm. Solid lines are film measurements, dashed lines are Monte Carlo. 44

2.6 Irradiation of an elliptical target (major axis 20 mm, minor axis 10 mm.), measured on EBT2 film. Dose distribution of nine field plan (a) and thirty-one field plan (b). Scale bar is 5 mm. Perpendicular dose profiles through the center of the dose distribution for the nine field plan (c) and the thirty-one field plan (d). Solid lines are the horizontal profiles; dashed lines are the vertical profiles. . . . 46
2.7 Image guided irradiation of off-axis BB with 5×5 mm^2 fields from four directions. Three 2.3 mm diameter BBs are visible. The bottom left BB was targeted for irradiation. Relative dose contours. Scale bar is 5 mm. The four beams with parameters are: (Gantry, X1 mm, X2 mm) (0°,−2.5,−7.5), (45°,−3.0,−8.0), (90°,−0.5,−5.5), (135°,4.0,−1.0). 47
2.8 Ungated (a) and gated (b) irradiation of an EBT2 film on a motion platform. Peak to peak motion of 5 mm. 48
2.9 Micro-CT images of an anesthetized rat. Transverse ungated (a) and gated (b) slices showing the lungs and heart. Sagittal ungated (c) and gated (d) slices through the left lung. Note the motion blur artifacts on the diaphragm boundary and lung sub-structure are reduced by gated image acquisition. However, cardiac motion blur is still evident, as the acquisition was only respiratory gated. The same hardware systems and techniques used to perform the gated image acquisition are used to deliver a gated therapy. 49
2.10 Image guidance of AP irradiation field. Fluoroscopy images without (a) and with (b) collimator in treatment position. Field was adjusted with image guidance to shield heart and diaphragm. Monte Carlo dose verification for AP-PA parallel opposed beam plan; transverse (c), sagittal (d) and coronal (e) slices shown. Scale bar is 10 mm. 50
2.11 An axial slice (a) of a 14×14 mm^2 parallel opposed fields irradiating the right lung to a total dose of 20 Gy delivered in 2 fractions. The bones in the scan field of view (the thorax) were segmented (b). Approximately 10% of the bone is receiving a dose above 5 Gy as shown in the dose volume histogram (e). The bone V_{5Gy} is 0.25 cm^3, which is approximately 2% of the total body bone volume of 14 cm^3 including the tail, estimated from a total body micro-CT scan. An axial slice (c) of a 10×10 mm^2 lateral parallel opposed fields irradiating a brain tumour to a total dose of 20 Gy delivered in 2 fractions. The skull was segmented (d). Approximately 10% of the skull is receiving a dose above 5 Gy (e). The bone V_{5Gy} is 0.4 cm^3, which is approximately 3% of the total body bone volume. 53

3.1 Images of the plastics phantoms, with the main body constructed of PMMA. Insert materials are labelled. Corresponding mid-phantom CT slices acquired at 70 kVp (a) and 120 kVp (b) displayed with the same window and level. . . . 66
3.2 Images of the solutions phantoms with insert solutions labelled. For $CaCl_2$ solutions, the g/mL is labelled, and for alcohol (EtOH), the percentage EtOH by volume is labelled. Corresponding mid-phantom CT slices acquired at 70 kVp (a), (c), (e) and 120 kVp (b), (d), (f) are displayed with the same window and level. 67

3.3 Effective atomic number (a), (c), (e), (g) and relative electron density (b), (d), (f), (h) are shown for the same slice of the large and small plastics phantoms. Material labels are shown in figure 3.1. 71
3.4 Effective atomic number are shown in (a), (c), (e) and relative electron density (b), (d), (f) for the solution phantoms. Insert materials are vials of solutions labelled in figure 3.2. 72
3.5 Combined phantom results are shown for small and large plastic phantoms, ethanol and calcium chloride solutions, CIRS and Gammex inserts. Error bars are the standard deviation of the voxel values in the ROI. Theoretical versus measurement values of effective atomic number (a) and relative electron density (b) are plotted with a dashed unity line. Note a linear correction is applied to the CCD detector data in chapter 4 that was not applied here. 73
3.6 Comparison of Hounsfield units scanned at 70 kVp (a) and 120 kVp (b), effective atomic numbers (Z_{eff}) (c), relative electron density ($\rho_e/\rho_{e,w}$) (d), relative errors of Z_{eff} (e) and $\rho_e/\rho_{e,w}$ (f), of material inserts inside the plastic phantoms. Materials are labelled according to names defined in table 3.2. The materials in the larger phantom are labelled to indicate whether the materials are in the outer ("Large Outer") or inner ("Large Inner") rings. They are compared to those inside the smaller phantoms. Error bars indicate the standard deviation of the pixels within the regions of interest. 74
3.7 Comparison of Hounsfield units scanned at 70 kVp (a) and 120 kVp (b), effective atomic numbers (Z_{eff}) (c), relative electron density ($\rho_e/\rho_{e,w}$) (d), relative errors of Z_{eff} (e) and relative errors of relative electron density $\rho_e/\rho_{e,w}$ (f), of $CaCl_2$ solutions. Indicated in the plots are the amounts of $CaCl_2$ in g/100 mL in the solutions. Multiple bars per concentration indicate a repeated measurement. Error bars indicate the standard deviation of the pixels within the regions of interest. 75
3.8 Relative differences in effective atomic numbers (Z_{eff}) and relative electron density ($\rho_e/\rho_{e,w}$) for ethanol solutions (a,b), CIRS inserts (c,d) and Gammex inserts (e,f). Multiple bars per material indicate a repeated measurement. Error bars indicate the standard deviation of the pixels within the regions of interest. . . . 76
3.9 Axial CT images acquired at 70 kVp of a mouse at the diaphragm (a) and head (d). Corresponding Z_{eff} (b,e) and relative electron density (c,f) images are also shown. 78

4.1 Plot of filtered spectrum used with the CCD detector and the CMOS detector. CCD 70 kVp (4.5 mmAl) and 120 kVp (1.0 mmCu + 4.5 mmAl). CMOS detector 60 kVp (0.4 mmCu + 4.5 mmAl) and 100 kVp (0.8 mmSn + 4.5 mmAl). All spectra normalized to the unit area under the curve. 93
4.2 Polyenergetic CT images of the large plastics phantom at 60 kVp (a) and 100 kVp (b). The plastic inserts are labelled in (a). The CT images were processed with the polynomial fit DECT method to produce the effective atomic number image (c) and relative electron density image (d). 94

4.3 Polynomial fit calculated effective atomic number (a,b) and relative electron density (c,d) plotted against their theoretical values for the CMOS detector (a,c) and CCD detector (b,d). Note a linear correction was applied to the CCD detector data (b,d) that was not applied to the same data in chapter 3. 95
4.4 Plots of the polynomial fits of the orders (2,4,6) for the CMOS and CCD detector acquired data. Effective atomic number (EAN) is plotted against dual energy ratio (DER) of attenuation coefficients for CMOS (a) and CCD (b). Low energy (LE) RED polynomial for CMOS (c) and CCD (d) are plotted against EAN. High energy (HE) RED polynomial for CMOS (e) and CCD (f) are plotted against EAN. 96
4.5 An illustration of the reduction of the cupping artefacts in the large plastics phantom. Axial CT slice of the phantom showing the position of the line profile (a). Line profiles of the low energy CT image volumes with spectra of 70 kVp and 60 kVp (b). Line profiles of the high energy CT image volumes with spectra of 120 kVp and 100 kVp (c). 101
4.6 Comparison of the difference in HU mean values for each location to the mean of the group for 5 plastic materials. The plastics phantoms were scanned with the new CMOS detector (60 and 100 kVp) and the old CCD detector (70 and 120 kVp). Error bars represent the standard deviation inside the region of interest in HU. Insert locations are plotted in order, left to right: large phantom inner ring, large phantom outer ring and small phantoms. Scanning x-ray spectra are color coded. 101

A.1 EBT2 film calibration curve fit of film net optical density to dose. Size of marker indicates standard deviation of netOD values. 122

C.1 Overview of the 4D CT with respiratory and MLC position data simulation. Gated delivery is shown. Linac and respiration log files are synchronized in time using the beam on and beam enable flags. The delivery is then divided into 400 ms samples (dashed boxes), containing linac state and patient respiratory information. Each of the samples is matched with the appropriate 4DCT phase image using the patient respiration phase information. Each time sample containing delivered MU is then simulated using the Monte Carlo dose computation. The series of dose matrices are then registered back to the base phase of the 4DCT scan, and summed to obtain the total dose. Areas of the beam enable/beam on graph where the gating window is open but no MU are delivered, are locations where the leaves are repositioning for the next IMRT segment. . . 133
C.2 End of Inhale (EOI) CT scan of 1D motion phantom in axial (a), sagittal (b) and coronal (c) view with contours for the concave target. Photograph of 1D motion phantom (d). 134

C.3 Coronal plane dose distributions for the concave target plan: a) no motion and b) continuous isocentre shift. Coronal plane dose difference between: c) discrete isocentre shift; d) 4DCT; e) 4DCT delivery average; f) 4DCT plan average; and continuous isocentre shift. Coronal plane of 3D gamma map (2%, 2 mm) between: g) discrete isocentre shift; h) 4DCT; i) 4DCT delivery average; j) 4DCT plan average; and continuous isocentre shift. 139
C.4 Coronal plane dose distributions for the integrated boost plan: a) no motion and b) continuous isocentre shift. Coronal plane dose difference between: c) discrete isocentre shift; d) 4DCT; e) 4DCT delivery average; f) 4DCT plan average; and continuous isocentre shift. Coronal plane of 3D gamma map (2%, 2 mm) between: g) discrete isocentre shift; h) 4DCT; i) 4DCT delivery average; j) 4DCT plan average; and continuous isocentre shift. 140

List of Tables

1.1 Comparison of select image-guided small animal irradiation systems. 11

2.1 Beam profile characteristics from EBT2 film measurements at isocenter and 12 mm depth 43

3.1 Clinical electron density phantom inserts. CT density phantom insert material values for physical density and relative electron density are from manufacturer data. Insert material effective atomic number was calculated using manufacturer elemental composition data. 63

3.2 Materials used in custom phantoms. Molecular formula corresponds to the primary component of the plastic. Additives, such as stabilizers or dyes were not considered in the calculation of the relative electron density or effective atomic number. Physical density values are from supplier data sheets, and verified by measurement. Ethanol and calcium chloride solutions were prepared with de-ionized water. 64

3.3 Comparisons of uncertainties in effective atomic number (Z_{eff}) and relative electron density ($\rho_e/\rho_{e,w}$) in conjunction with imaging noise (in HU) with and without median noise filtering in the HU images. Reported values are the median (minimum–maximum) standard deviations (std dev) of the respective quantity of interest within regions of interests in the small plastic phantoms and the EtOH solution phantoms. 77

4.1 Scanning protocol characteristics. 88

4.2 Material Properties. Gammex inserts marked with * were not scanned with the CCD version of the micro-CT. 90

4.3 Root mean square error (RMSE) and residuals of EAN and RED from the polynomial fit DECT method and spectral DECT method. 98

4.4 Root mean square error (RMSE) and residuals of EAN and RED from the polynomial fit DECT method and spectral DECT method. 99

4.5 Summary of percent difference between theory and measurement of EAN and RED for material sets (Plastics and Gammex), input images sets (polyenergetic and virtual monoenergetic) and DECT algorithms (Spectral and Polynomial fit) for the CMOS detector. 100

5.1 Comparison of select image-guided small animal irradiation systems with the system developed in this thesis. 112

C.1 3D Gamma analysis (2%, 2 mm) comparing 4D methods to gold standard continuous isocentre shift method. 138

List of Appendices

A Film processing details 120
B Dual energy algorithms 124
C Study of the IMRT interplay effect using 4DCT Monte Carlo dose calculation . 129
D Permission to Reproduce Previously Published Materials 145
E Animal Ethics Approval 162

List of Abbreviations, Symbols, and Nomenclature

4DCT	four-dimensional computed tomography
AP	anteriorposterior
CAD	computer-aided design
CBCT	cone-beam computed tomography
CCD	charge-coupled device
CERR	Computational Environment for Radiotherapy Research
CMOS	complementary metal-oxide-semiconductor
CT	computed tomography
DCE-CT	dynamic contrast-enhanced computed tomography
DECT	dual energy computed tomography
DEmCT	dual energy micro-computed tomography
DER	dual energy ratio
DNA	deoxyribonucleic acid
EAN	effective atomic number
FOV	field-of-view
GI	gastrointestinal
HE	high energy

HU	Hounsfield unit
ICRU	International Commission on Radiation Units and Measurements
IGRT	image guided radiation therapy
IMRT	intensity modulated radiation therapy
LE	low energy
linac	linear accelerator
LRCP	London Regional Cancer Program
micro-CT	micro-computed tomography
micro-CT/RT	micro-computed tomography/radiation therapy
MLC	multi-leaf collimator
MR	magnetic resonance
MRI	magnetic resonance imaging
MU	monitor unit
OD	optical density
PA	posterioranterior
ρ	physical density
$\rho_e/\rho_{e,w}$	relative electron density
RED	relative electron density
RT	radiation therapy
RMSE	root mean square error
SARRP	Small Animal Radiaiton Research Platform
Z_{eff}	effective atomic number

Z_{med}	effective atomic number of medium
Z_w	effective atomic number of water

Chapter 1

Introduction

1.1 Cancer

Cancer is a class of diseases characterized by uncontrolled cell growth. Mutations are changes in the information encoded in the DNA of the cell that can cause the overexpression of pro-growth oncogenes, or inactivation of tumour suppressor genes. When the balance between oncogenes and tumour suppressors is sufficiently upset to favour oncogenes, the cell can continuously divide. The cells can gain several additional characteristics through succeeding mutations and acquire an invasive cancer phenotype. The characteristics of metastatic cancer are often described as the Hallmarks of Cancer, proposed by Hannah and Weinberg.[1,2]

Cancer is prevalent in Canadian society, with 45.1% of men and 41.4% of women predicted to be diagnosed within their lifetime.[3] The survival rates for cancers vary greatly, even among some of the most common cancers. The Canadian five-year relative survival rate for breast cancer is 88%, contrasted to 17% for lung cancer.[3]

1.2 Treatments for Cancer

The treatment of cancer can broadly be divided into three categories: surgery, radiation therapy, and systemic therapy (chemotherapy, biologic therapy).[4–8] Surgery is often the preferred treatment for early localized disease, i.e. cancers that have not spread to either local lymph nodes or

more distant organ sites.[4] Radiation therapy is frequently used for locally advanced disease, irradiating both the primary tumour and surrounding tissue, and lymph nodes that likely harbour undetected cancer cells.[5] In some instances, radiation therapy can be the primary treatment for early localized disease. For example, early and moderately advanced laryngeal cancer can be initially treated with radiation therapy with the more invasive laryngectomy reserved for relapse.[9] Systemic therapies, such as chemotherapy, are used to treat systemic disease that has spread to distant sites.[6,8] The three treatments are often combined to provide a treatment protocol optimized for each cancer type and stage. For example, radiation and chemotherapy can be administered to reduce the tumour bulk prior to surgery, or after surgery to combat residual occult disease.[4–6,10]

Traditional chemotherapeutics have been cytotoxic compounds that preferentially kill dividing cells.[6,11] Hence they kill cancer cells, but also normal replicating cells such as hair, gastrointestinal, and haematopoietic cells.[6,11] The death of normal cells results in many of the adverse reactions of these drugs.[6,11] Newer targeted pharmaceutical compounds have been developed to interfere with specific cellular pathways associated with cancer and are aimed at reducing collateral toxicity.[8,11]

1.3 Development of radiation therapy

Development of radiation therapy for the period after the Second World War has been primarily one of technological advancement.[12–17] While it is known that fast growing cells, such as cancer, tend to be more sensitive to radiation and cytotoxic chemotherapy than slower growing cells, radiation can be spatially confined unlike a systemic drug.[11] Therefore, one of the overarching goals of radiotherapy development for the past several decades has been to increase the accuracy and precision with which ionizing radiation can be delivered to targeted regions in cancer patients.[12,16,18] Improved anatomical imaging by CT and MRI allowed improved accuracy through better target identification and localization during treatment planning.[12,13,19,20]

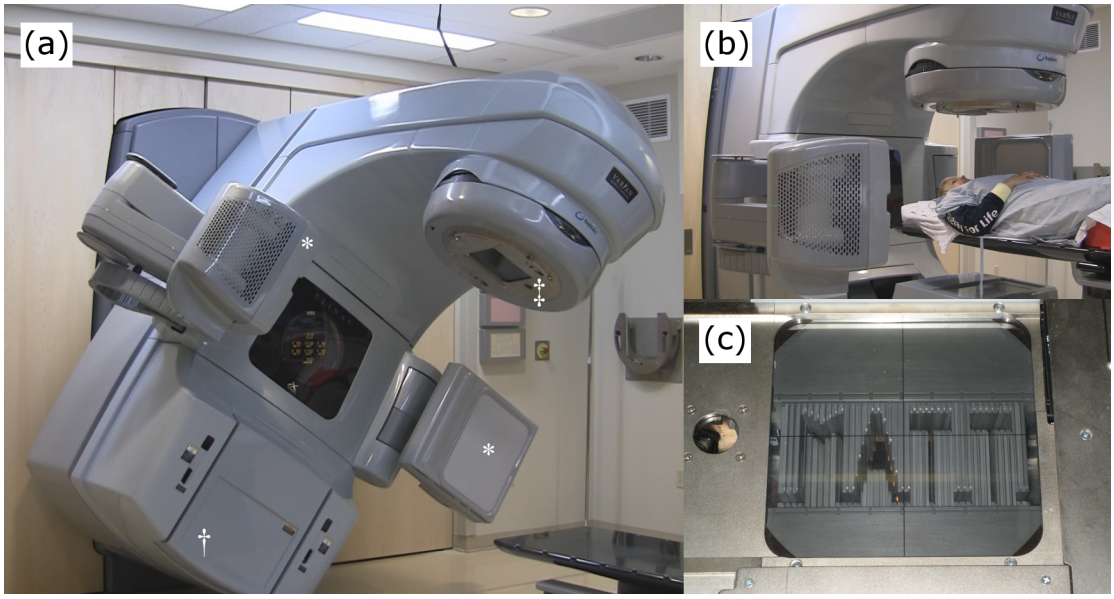

Figure 1.1: Photo of a modern linear accelerator (linac) equipped with kilovoltage onboard x-ray imaging (∗), electronic portal dosimeter (megavoltage imaging) (†) and multileaf collimator (‡). All imaging components are retracted in (a). Imaging devices are all extended around a mock patient in (b). The multileaf collimator can produce many complex shapes, including letters (c)

Collimation technologies combined with image guidance during therapy have allowed for increased precision in radiation delivery to targeted zones.[15,16]

1.3.1 Image guidance in radiation therapy

The addition of an imaging system to the radiation treatment unit allows for the patient to be imaged prior to therapy that often spans weeks of daily treatments. Many linear accelerators (linacs) come equipped with on-board x-ray imaging and electronic portal dosimeter (figure 1.1).[15,20] This allows for 2D static radiographs (figure 1.2), 2D motion fluoroscopy and 3D cone-beam CT (figure 1.3).[13,15,20,21] The pre-treatment or images concurrent with treatment are used to correct patient setup errors or monitor position during treatment.[13,20,22] In addition to improving the accuracy of conventional radiation therapy, image guidance enables the targeting confidence required for advanced techniques like stereotactic radiosurgery with ablative radiation doses.[15,16]

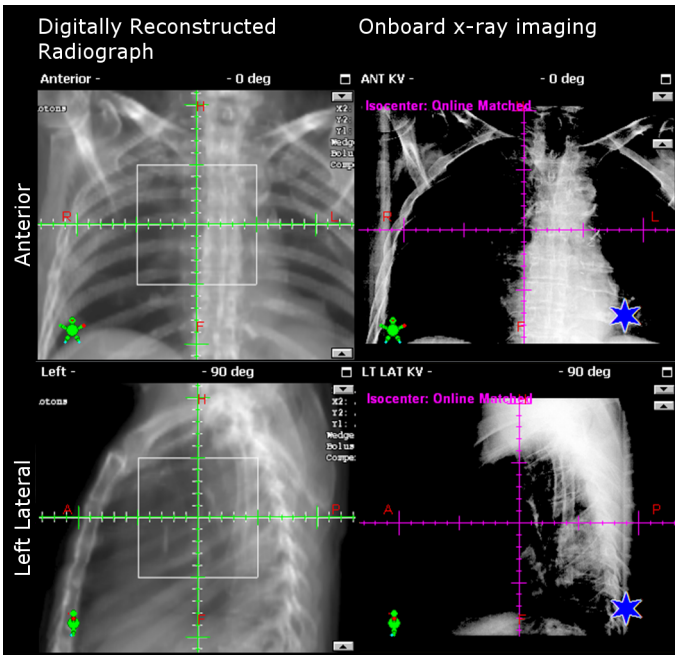

Figure 1.2: Digitally reconstructed radiographs derived from CT used in treatment planning compared with projection kV images acquired prior to a therapy session. The anterior and lateral views are used to correct patient positioning by aligning skeletal or target landmarks in all dimensions. Courtesy Dr. J. Chen.

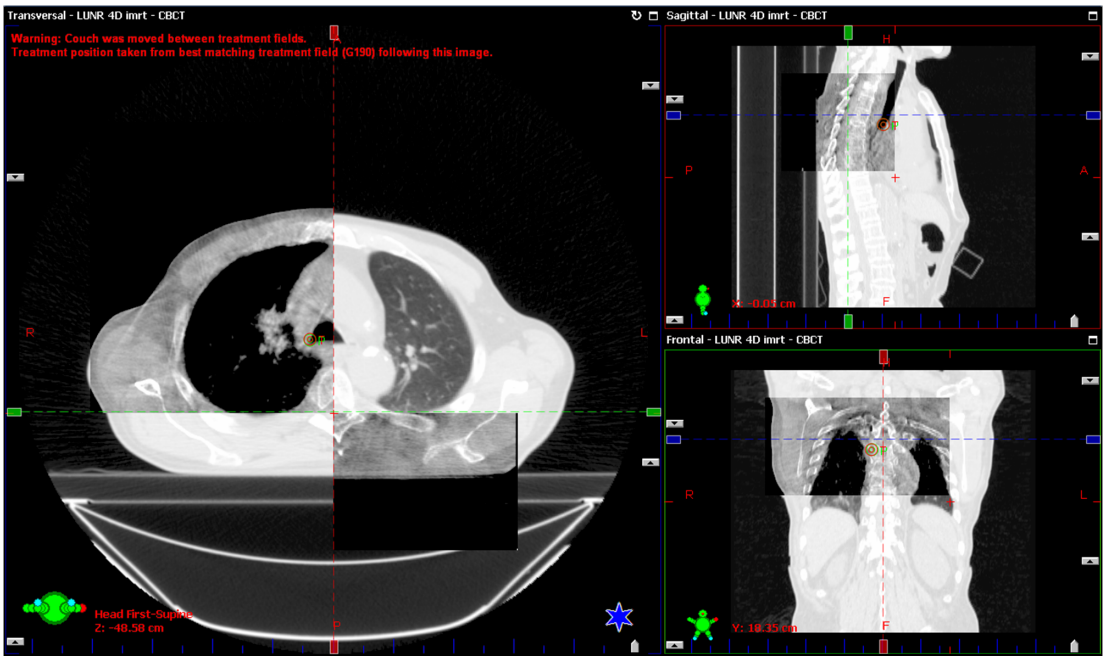

Figure 1.3: The planning CT image (lighter) is compared with the cone beam CT (darker). The cone beam CT acquired prior to treatment (using the onboard kilovoltage x-ray system) is aligned or registered with the planning CT to correct the patient position using both skeletal and soft tissue features. Courtesy Dr. J. Chen.

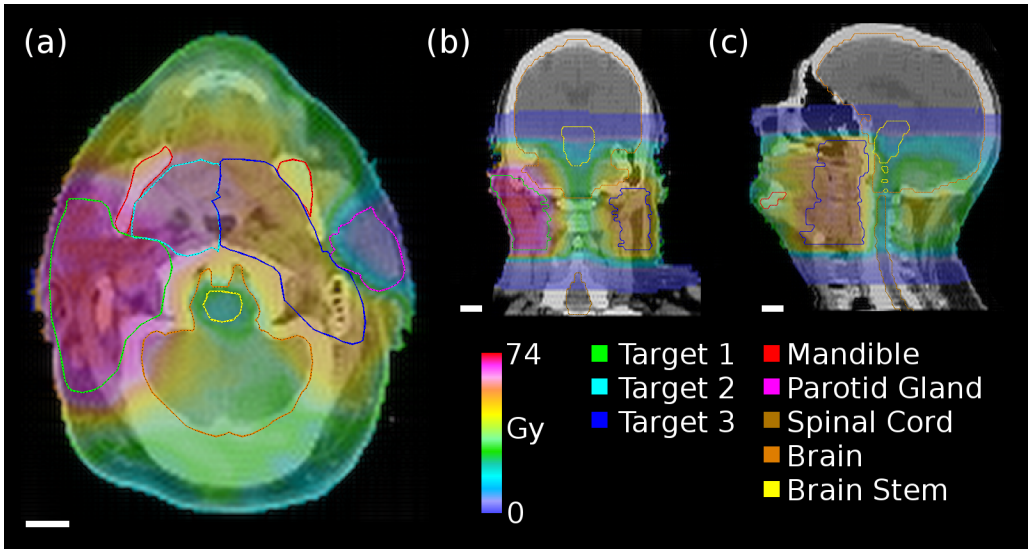

Figure 1.4: Intensity Modulated Radiation Therapy (IMRT) treatment plan for a head and neck cancer patient displayed with transverse (a), coronal (b) and sagittal (c) views. Dose is displayed as a colourwash overlaid on the CT images. The three concave targets surrounding the brain stem are treated to different dose levels using intensity modulation and multiple beam directions. Concurrently, the dose is minimized to healthy organs, such as the brain, brain stem, spinal cord, parotid gland and mandible. Scale bar is 2 cm. Sample IMRT plan data from the Computational Environment for Radiotherapy Research (CERR) www.cerr.info

1.3.2 Intensity modulation in radiation therapy (IMRT)

Conforming the radiation dose to complex anatomical structures that may be concave required the development of complex beam shaping hardware and treatment planning software.[15,16,18] A collimation device, called a multi-leaf collimator (MLC) is shown in figure 1.1c. Intensity modulation allows the precise delivery of a uniform radiation dose to a complex shape at depth in the patient.[16,18] By shaping and confining the therapeutic dose to the targeted cancer, the surrounding health structures can receive lower doses and treatment complications can be minimized in normal tissues.[23] An IMRT treatment plan for a head and neck cancer patient is presented in figure 1.4. The concave targets are irradiated with different dose levels while minimizing dose to healthy structures.

1.4 Next generation radiotherapy: biological targeting

The technical development of radiation therapy has achieved remarkable accuracy and precision in depositing radiation dose in a geometric sense.[12] However, questions remain on how best to use this very accurate and precise tool if the target is delineated with much uncertainty.[12] To do so requires further understanding and exploitation in cancer radiobiology, such as biological target volumes proposed by Ling et al.[24] or dose painting.[25] While radiotherapy has progressed on a technological path, concurrently the understanding of cancer biology has greatly improved. Currently, pharmaceuticals are being developed to act on specific targets of cancer cells.[8,26] Genome sequencing allows for the identification of specific mutations in cancers.[27] Molecular imaging allows the probing of the biological entities and their function in patients.[28,29] This wealth of biological information has not been fully exploited in the treatment of cancer with targeted therapy.[20,26] Genome information is used to identify patients who are likely or unlikely to respond to new targeted drug therapies. For example, the drug vemurafenib targets the mutant B-Raf protein (V600E or V600K), part of a pathway that mediates cell growth signals.[30] Many melanomas have mutated BRAF genes,[31] and a clinical trial demonstrated identifying melanoma patients with the V600E or V600K mutant variant of BRAF and treating with vemurafenib.[32] However, radiation therapy has been slower to utilize this new biological information. As new surgical techniques and pharmaceutical compounds become available, their combination with radiation therapy will need to be optimized to “hit” tumour cells more specifically and spare normal cells.[26]

1.5 Benefits of preclinical irradiation studies

Drug development is heavily dependent on preclinical animal studies to evaluate the effectiveness and safety of candidate drug compounds. Preclinical animal studies provide a complex living system to test any new therapeutic agent under well controlled conditions, allowing cost-effective, intensive and invasive data collection not ethically possible during human clin-

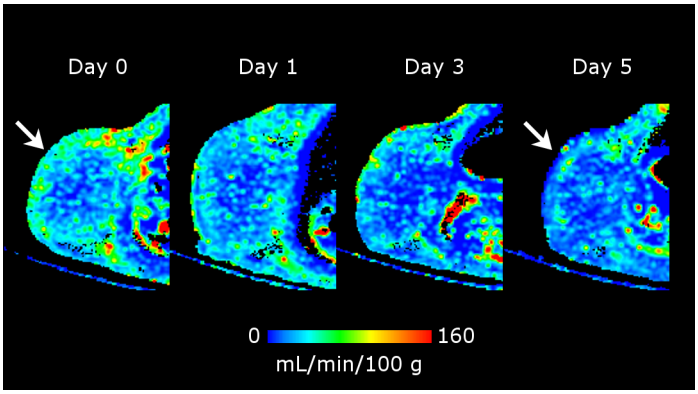

Figure 1.5: Example DCE-CT blood flow images of a subcutaneous xenograft hypovascular human colon tumour (LoVo) treated with an anti-angiogenic drug (Vandetanib) and followed for 6 days. A reduction in the blood flow in the rim of the tumour is observed over the treatment period (white arrow). Courtesy Drs. J. H. Tai and T.-Y. Lee

ical trials. The potential drawback of the down-scaled experiments is that the animal model may not mimic the human situation.[33]

An example preclinical trial is briefly presented. Tissue hemodynamics can be measured with dynamic contrast enhanced CT (DCE-CT).[34] The hemodynamic characteristics of the tumour at diagnosis and how it changes over the course of therapy are potential prognostic and predictive biomarkers.[35] While DCE-CT images have been acquired as part of clinical trials, the frequency of imaging cannot match that possible in a preclinical trial. A preclinical investigation with an anti-angiogenic drug treatment monitored by frequent DCE-CT is presented in figure 1.5. Radiation therapy development has not traditionally used preclinical studies, because the objective of improving dose conformity and targeting accuracy was deemed self-evident and did not require preclinical evidence to justify a clinical trial. **As the focus is shifting to biologically-targeted radiotherapy, preclinical studies with animals are needed to generate evidence to support clinical trials**.

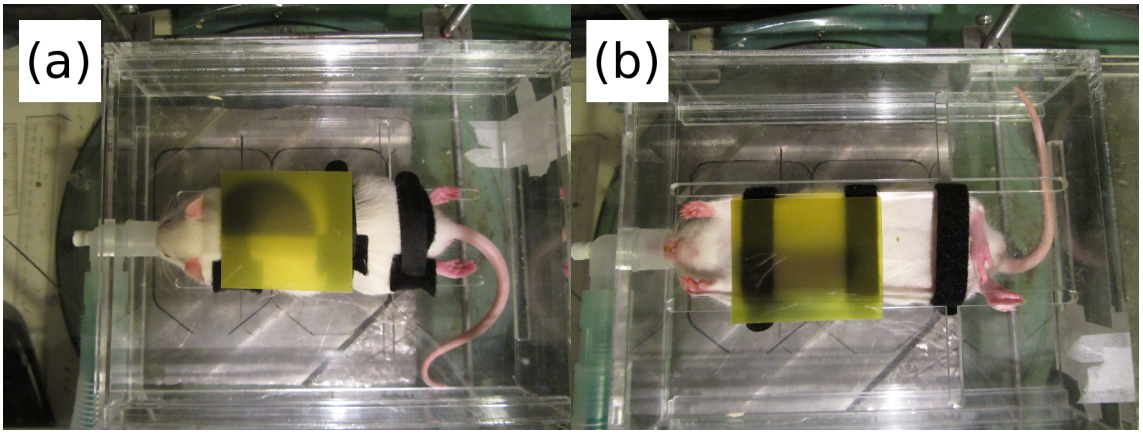

Figure 1.6: Irradiation of the right lung of a rat with a cobalt-60 source from below at the London Regional Cancer Program. The rat was anesthetized with isoflurane and held in a restraint box above the beam aperture. A radiochromic film was placed on the rat (yellow) to verify the radiation field location after irradiation (black semi-circle). Two parallel-opposed beams were delivered by first irradiating the animal in the prone position (a) and then rotating the restraint box so the rat was in the supine position (b). Photo credit: Dr. E. Wong.

1.6 Current small animal irradiator technology

1.6.1 Whole body irradiators (x-ray, radionuclide)

Laboratory irradiation of animals has traditionally been simple.[36] Often the irradiation study only required gross targeting, if any targeting at all. Many studies irradiated the entire animal, or a large portion, such as half the animal or a limb. Collimation of the field when present is usually done by using shaped lead blocks that are manually placed.[37,38] Whole body irradiator cabinets containing a radioactive or x-ray source are often used for bone marrow ablation studies. These can be used for radiation therapy studies also by adding lead shielding above the animal. However, this setup lacks any image guidance to visualize sub-dermal targets. Irradiation devices from the clinic have been adapted for small animals. This can vary from using superficial x-ray units and cobalt-60 sources to state-of-the-art linear accelerators. The simpler approaches, like a superficial unit[39] or cobalt source are similar to the irradiator cabinet with no image guidance and complex lead shielding. Locally at the London Regional Cancer Program, an old cobalt-60 source has been used for small animal irradiation, as shown in fig-

ure 1.6. Advanced linear accelerators are sized for irradiating human patients, so while they have image guidance and advanced beam collimation, adaptation to the sizes of small animals is challenging. Often even with an advanced accelerator, the irradiation plan is simplified to whole or partial body irradiation.[40]

1.6.2 Image guided conformal irradiators

Several research investigators have developed image-guided conformal irradiators specifically for small animal studies. The 2011 review by Verhaegen el al.[36] covers the development of a number of preclinical irradiators. This section will concentrate on two systems that were commercialized and a third system more closely related to the work presented in this thesis. Table 1.11 provides an overview of the system capabilities.

1.6.2.1 Small Animal Radiation Research Platform (SARRP)

The Small Animal Radiation Research Platform (SARRP) (figure 1.7) was originally developed at Johns Hopkins University (Baltimore, MD).[41,42] This was one of the first complete systems reported in the literature for image-guided conformal irradiation. Since the initial publication, the system has undergone extensive development resulting in a mature commercial product now currently sold by XSTRAHL Ltd. (Surrey, UK). The mechanics of the SARRP allow for many non-coplanar beam directions, as the animal couch allows for translation in 3 dimensions and rotation. CT acquisition is dependent upon rotation of the couch, but the gantry rotation is restricted and the imaging detector is stationary. The x-ray tube and generator is capable of operation up to 225 kVp and is used as both the imaging and therapeutic source. The initial design was unshielded and required lead curtains or a shielded room. Subsequent commercial development added a self-shielding cabinet, as well as an additional portal imaging detector placed on the beam exit side of the animal. A planning system (Muriplan) is commercially available. Recently, a symmetric jaw collimator and respiratory-gated shutter system became

	SARRP (Johns Hopkins)	X-Rad 225Cx (Toronto and Masstricht)	Stanford University
Maximum accelerating potential (kVp)	225	225	120
Interchangeable beam filters	Yes	Yes	No
Dose rate (Gy/min)	4	4	2
Collimation	Fixed cones (Jaw option recently available)	Fixed cones	Computerized variable aperature
Field sizes	Circular and Square 0.5 mm ⊘ – 10 mm × 10 mm	Circular and Square 1.0 mm ⊘ – 10 mm × 10 mm	Pseudo-circular 0.1 – 6 cm ⊘
Beam direction	non-coplanar	coplanar	coplanar
Asymmetric/off-axis fields	No	No	No
Stage translation	3D + rotation	3D	3D (contrained by CT bore)
Respiratory Gating	No (Gated shutter option recently available)	No	No
Image resolution (μm)	130	200	49
Targeting accurracy (μm)	200	200	100
Dose calculation and planning system	Muriplan (Commericial)	SmART-Plan (Maastro Clinic, Commercial)	RT_Image (Stanford, in-house)

Table 1.1: Comparison of select image-guided small animal irradiation systems.

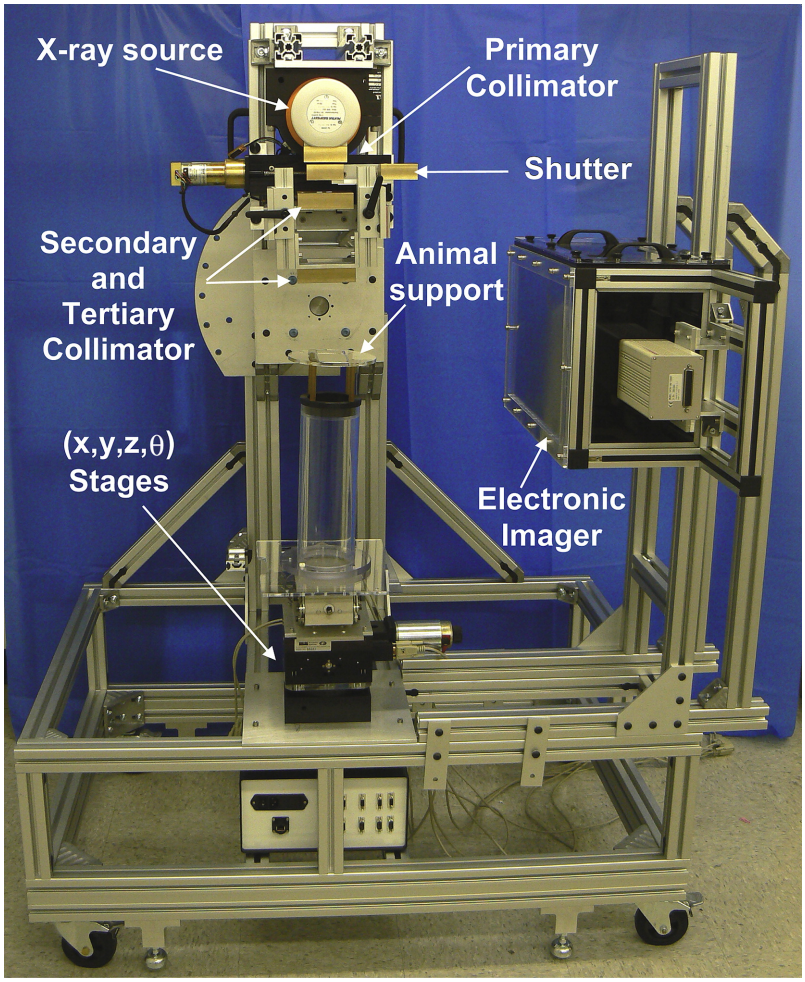

Figure 1.7: The first version of the SARRP system. "Small animal radiation research platform (SARRP) with conformal irradiation and cone-beam computed tomography guidance capabilities. Maximal extent of system measures 3 ft. wide, 4 ft. long, and 6 ft. tall. It is equipped with wheels for ease of transport but rests on stops for stationary use. Camera-based electronic imaging system has since been replaced with a 21-cm × 21-cm flat panel amorphous silicon detector." Reprinted from Int. J. Radiat. Oncol. Biol. Phys., **71**(5), J. Wong, E. Armour, P. Kazanzides, I. Iordachita, E. Tryggestad, H. Deng, M. Matinfar, C. Kennedy, Z. Liu, T. Chan, O. Gray, F. Verhaegen, T. McNutt, E. Ford, and T. L. DeWeese, "High-Resolution, Small Animal Radiation Research Platform With X-Ray Tomographic Guidance Capabilities", 1591–1599, Copyright (2008), with permission from Elsevier. doi:10.1016/j.ijrobp.2008.04.025

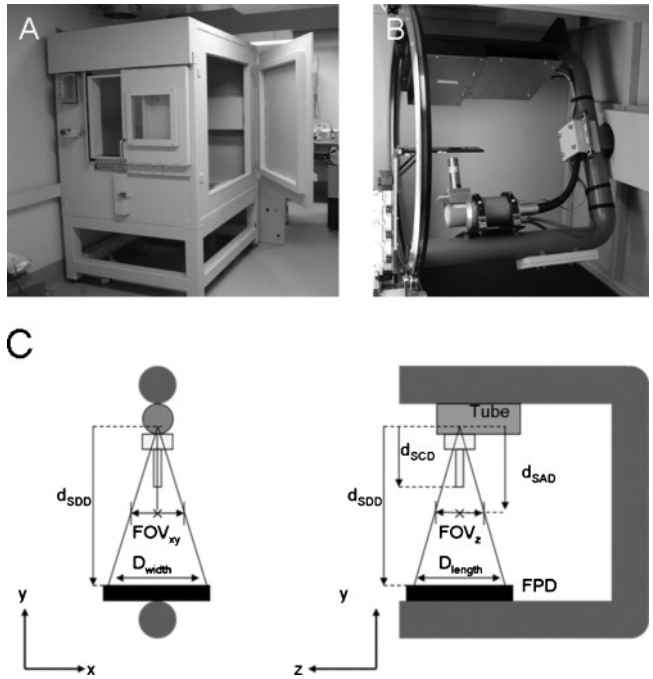

Figure 1.8: "Pictures of the micro-IGRT (X-Rad 225Cx) unit. (a) The exterior of the self-shielded cabinet. (b) Interior, showing the C-arm setup with collimator and 3D linear translation stage. (c) Geometry of the system, with d_{SAD} = 30.7 cm, d_{SDD} = 64.5 cm, and d_{SCD} = 23 cm. The primary beam is collimated to cover the entire detector surface ($D_{width} \times D_{length}$ = 20.4 × 20.4 cm^2), giving a FOV_z = FOV_{xy} = 9.7 cm." Reprinted with permission from R. Clarkson, P. E. Lindsay, S. Ansell, G. Wilson, S. Jelveh, R. P. Hill, and D. A. Jaffray, Med. Phys. **38**, 845–856 (2011). Copyright 2011, American Association of Physicists in Medicine. doi:10.1118/1.3533947

available after the second chapter of this thesis was published.[17] However, demonstrations of these new SARRP accessories have not yet been documented in the literature.

1.6.2.2 Toronto System

The group at Princess Margaret Cancer Centre (Toronto, ON) developed the X-Rad 225Cx in partnership with Precision X-Ray Inc. (North Bradford, CT). Depicted in figure 1.8, the X-Rad 225Cx is based on a C-arm geometry, restricting treatment beams to a coplanar geometry.[43] CT image acquisition is more conventional, with a fully rotating x-ray source and detector. Similar to the SARRP, the X-Rad 225Cx uses a 225 kVp x-ray tube and generator for both imaging and therapy. Additionally, this system comes with a self-shielded cabinet.

1.6.2.3 Maastricht System

The group at Maastricht University Medical Center (Maastricht, Netherlands) purchased a X-Rad 225Cx system and developed a number of enhancements. Electronic portal imaging devices (EPIDs) have been used to measure the therapeutic radiation beam exiting the human patient to verify the dose delivered during therapy.[44] The Maastricht group brought EPID verification dosimetry to small animal radiotherapy.[45] They modified a Monte Carlo code to continue particle transport beyond the irradiated object and scored them on a plane corresponding the EPID. The virtual portal dosimetry images were compared to film measurements with an agreement within 5% for fields larger than 4 mm. Another contribution was a fast analytical source model to generate particles for Monte Carlo dose calculations.[46] Monte Carlo modelling of the x-ray tube and collimators for the small fields desired for small animal therapy remain a challenge. The fast analytical source model was developed to investigate improved collimator design and faster dose calculations for treatment planning. A small animal treatment planning system (SmART-Plan) was developed and validated at Maastricht and is now available as a commercial product sold by Precision X-Ray Inc.[47]

1.6.2.4 Stanford System

The Stanford group took a different approach, and instead of building a new radiotherapy system from scratch, decided to modify a micro-CT into an image-guided irradiator.[48,49] The benefit of this approach is that most of the system components and functionality is pre-existing, and only a few additions and modifications are required. The main addition was the construction of a computerized collimator (figure 1.9) that allowed for arbitrarily-sized dodecagonal (twelve sided) fields that are referred to as pseudo-circular fields.[50]

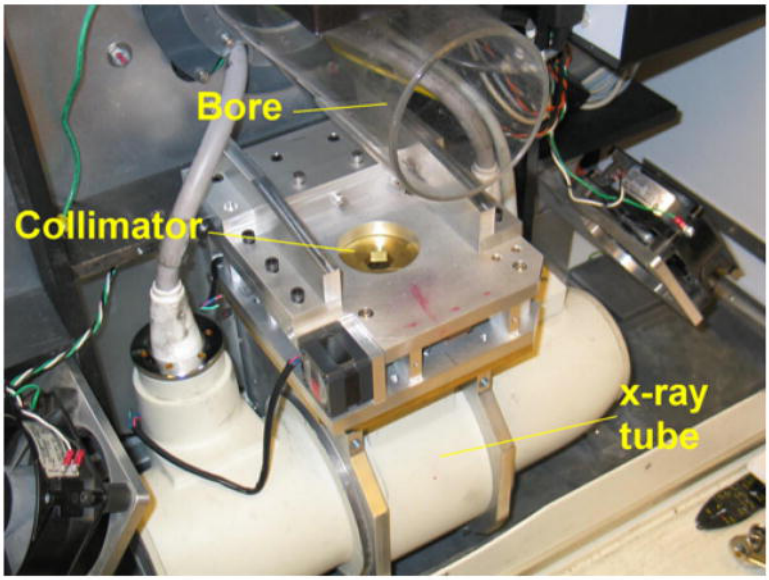

Figure 1.9: Computerized collimator of the Stanford micro-CT/RT system. "The variable-aperture collimator in the microCT/RT system uses two disks with hexagonal shape that open and close like an iris camera. The disks are rotated 30° one with respect to the other to form a field of dodecagonal shape." Reprinted from Phys. Med. Biol. **54** (2009) 3723–3740, M. Rodriguez, H. Zhou, P. Keall, and E. Graves, "Commissioning of a novel microCT/RT system for small animal conformal radiotherapy", © Institute of Physics and Engineering in Medicine. Reproduced by permission of IOP Publishing. All rights reserved. doi:10.1088/0031-9155/54/12/008

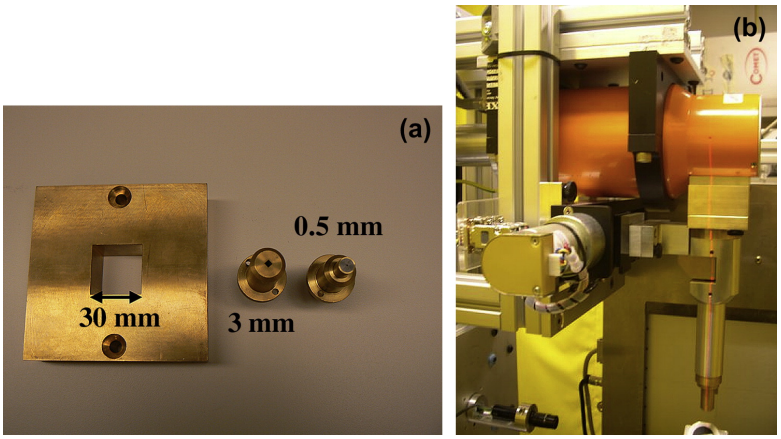

Figure 1.10: Collimators for the SARRP system. "(a) Tertiary brass collimation inserts with dimensions of 30 mm × 30 mm, 3 mm × 3 mm, and 0.5 mm diameter for small animal radiation research platform. (b) Radiosurgery-like collimating cone assembly attached to primary collimator of the small animal radiation research platform for small field irradiation (<5 mm × 5 mm in dimension)." Reprinted from Int. J. Radiat. Oncol. Biol. Phys., **71**(5), J. Wong, E. Armour, P. Kazanzides, I. Iordachita, E. Tryggestad, H. Deng, M. Matinfar, C. Kennedy, Z. Liu, T. Chan, O. Gray, F. Verhaegen, T. McNutt, E. Ford, and T. L. DeWeese, "High-Resolution, Small Animal Radiation Research Platform With X-Ray Tomographic Guidance Capabilities", 1591–1599, Copyright (2008), with permission from Elsevier. doi:10.1016/j.ijrobp.2008.04.025

1.6.3 Current challenges in small animal irradiation

With the development of various hardware platforms for image-guided conformal small animal irradiation, several challenges remain.

1.6.3.1 Conformity, intensity modulation, planning

The commercial irradiator systems available are limited by their simple beam shaping. The set of fixed cones (figure 1.10) that are manually changed limit the conformal abilities of a single beam. Unlike the multileaf collimators of clinical linear accelerators that can create complex shapes, these commercial preclinical systems are constrained to pre-set circular and square fields. The Stanford system can create any arbitrarily sized dodecagonal (pseudo-circular) field allowing more flexibility, but still is quite limited compared to a clinical system. The lack of beam-shaping hardware limits the options for implementing intensity modulation on a small animal. While a small pencil beam could be scanned to create a complex intensity pattern, it is

less efficient than a single shaped field. In addition to beam-shaping hardware, there is no sophisticated small animal treatment planning system. The previously mentioned Muriplan and SmART-Plan are visualization and analysis platforms for forward planning and dose calculation. They currently are not capable of inverse-planning complex intensity modulation delivery plans as is the case in human irradiation.

In the clinical realm, many techniques for managing respiration, such as gating and breath coaching techniques have been investigated and applied.[21,51] Similar respiratory motion management techniques for small animals have largely been unexplored.

1.6.3.2 Dose calculation with kV energies

Small animals irradiation systems use kilovoltage x-ray sources because this energy is sufficient for penetrating the small size of the animals.[36] Clinical systems use more penetrating megavoltage beams to be able to treat internal tumours to sufficient dose without depositing toxic doses closer to the surface. However for small animals, especially mice, megavoltage beam characteristics are less suitable and could potentially under-irradiate tumour portions at shallower depths; the dose build-up region of a megavoltage beam could be more than half the thickness of a mouse![36] The build-up and scatter characteristics of a kilovoltage beam are therefore more suitable for small animals.[36] The drawback of a kilovoltage beam is the proportion of photoelectric absorption in the dose deposition. For a megavoltage beam, the vast majority of dose deposition is by incoherent (Compton) scattering, requiring only knowledge of electron density to compute dose deposition. At kilovoltage energies, accounting for photoelectric absorption is necessary, requiring knowledge of both the atomic composition and electron density to compute dose accurately. Figure 1.11 illustrates the differences in mass energy-absorption for three tissues at varying photon energies.[52] This suggests the need for dual energy CT imaging that can produce maps of electron density and atomic number.[53]

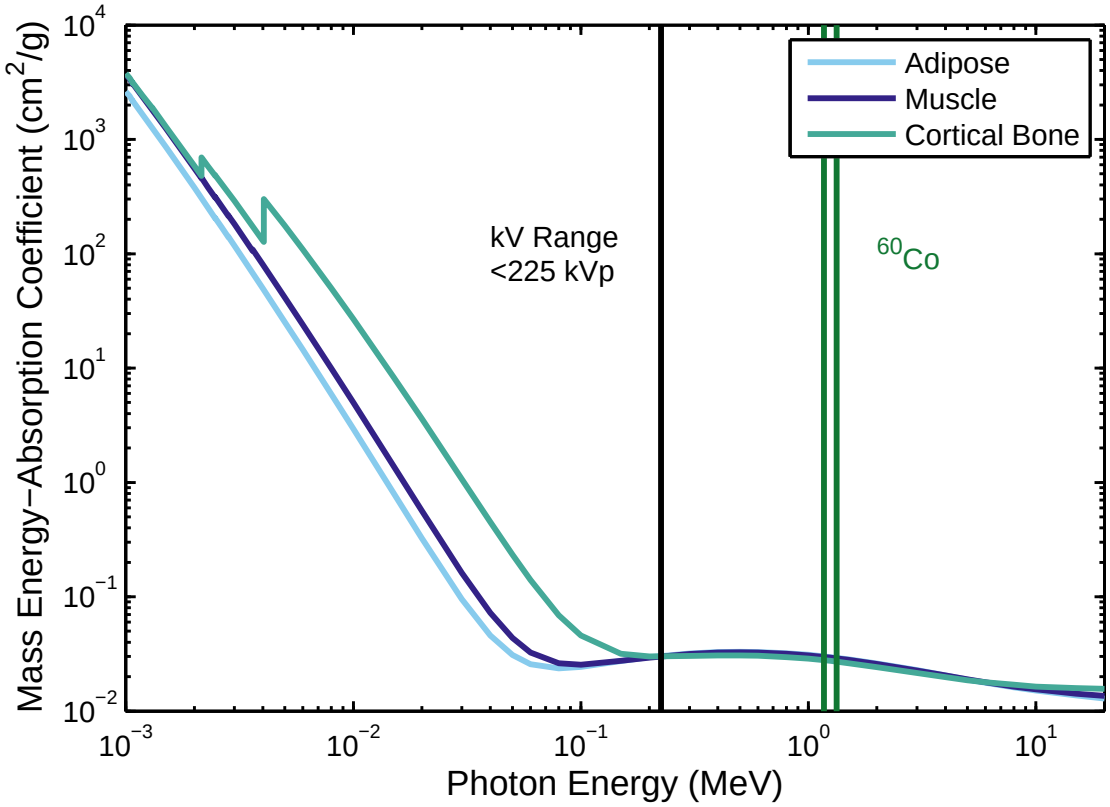

Figure 1.11: Mass Energy-Absorption Coefficient (MEAC) for three ICRU-44 tissues: adipose, skeletal muscle and cortical bone. The MEAC is closely related to absorbed radiation dose. At kilovoltage energies below 225 kVp the MEAC differs between the three tissues due to photoelectric absorption, which is dependent on the chemical composition of the tissue. To calculate the dose accurately at kilovoltage energies, both the density and chemical composition of the tissue is needed. For comparison, at the cobalt-60 energies, the MEAC differs little between the three tissue types and only density information is needed. The chemical composition has negligible effect on the dose at megavoltage energies. Data from Hubbell and Seltzer.

Monte Carlo dose calculation techniques are generally recognized as the most accurate dose computation method.[54] This method models individual particles interacting with atoms in materials in a given geometry.

1.7 Dual-Energy Computed Tomography

Signal in a kV x-ray image is dependent upon two factors, the electron density (e per cm^3) and the atomic number of the interrogated tissues. If imaging at a single energy, or fixed energy spectrum, and only measuring an integrated transmission value, it is not possible to distinguish a high density low atomic number material from a low density high atomic number material. One way to distinguish these two cases is to use two energies, or modified spectra. Dual energy computed tomography (DECT) acquires two image sets at two different x-ray energies. Using the information from images at two energies, it is possible to distinguish the high density low atomic number material from a low density high atomic number material.[55,56]

1.8 Research Goals and Objectives

The research goal of this thesis was to develop the technology and techniques in small animal image-guided radiation therapy to address some of the challenges identified in the previous sections (i.e. maximum animal size, complex collimation, beam gating, dual-energy CT for Monte Carlo dose calculation). The specific aims included:

1. Develop a system with asymmetric fields that could treat off-axis tumours in rats
2. Gated therapy for irradiation of thoracic and abdominal tumours
3. Commission the micro-CT/RT irradiator and Monte Carlo dose calculator
4. Dual energy micro-CT to measure effective atomic number and relative electron density for more accurate Monte Carlo dose calculations

1.9 Thesis Outline

1.9.1 Chapter 2: Implementation and commissioning of an integrated micro-CT/RT system with computerized independent jaw collimation

The design, construction and commissioning of an image-guided conformal small animal irradiator is documented in this chapter. Computer controlled motorized independent jaws were designed, built, installed and commissioned for a commercial micro-CT scanner. The addition of the jaws with other modifications converted the micro-CT into a micro-CT/RT system. The design addressed the limitations of other pre-existing systems by allowing **asymmetric fields** under computer control and gated delivery. This chapter is adapted from the research article, "Implementation and commissioning of an integrated micro-CT/RT system with computerized independent jaw collimation" published in Medical Physics, 2013, July 12;40(8): 081706 by M. D. Jensen, W. T. Hrinivich, J. A. Jung, D. W. Holdworth, M. Drangova, J. Chen, and E. Wong.

1.9.2 Chapter 3: Determination of effective atomic numbers and electron densities with dual energy micro-CT measurements

Image-guided small animal irradiators employ kilovoltage photon beams (120 kVp to 320 kVp) where the radiation dose is strongly dependent on the atomic number of the absorbing medium due to photoelectric absorption. Dual energy CT (DECT) can measure the relative electron density (RED) and effective atomic number (EAN) independently and has been demonstrated with clinical human CT scanners. We apply previously published DECT algorithms to micro-CT images and experimentally investigate the feasibility of measuring the effective atomic number and relative electron density. A large number of test materials, including custom designed phantoms, are examined with dual energy micro-CT for verification of results. While we found

measurement of effective atomic number and relative electron density generally feasible, beam-hardening artifacts were found to impact accuracy negatively. This chapter is adapted from the research article, "Determination of effective atomic numbers and electron densities with dual energy micro-CT measurements" by M. D. Jensen, J. Chen, and E. Wong.

1.9.3 Chapter 4: Improved determination of effective atomic numbers and electron densities using dual energy micro-CT with optimized spectra and a CMOS panel detector

The work of chapter 3 identified beam-hardening artefacts as a hindrance to accurate effective atomic number and relative electron density measurement with dual energy micro-CT. Optimization of the x-ray spectra by additional filters narrows the spectral width and reduces beam-hardening artefacts. The increased filtering also reduces the photon flux, requiring a more sensitive detector to acquire images. We examine the improvement in measuring the effective atomic number and relative electron density using harder spectra and a flat panel detector. Additionally, four dual-energy CT processing methods are compared. This chapter is adapted from the research article, "Improved determination of effective atomic numbers and electron densities using dual energy micro-CT with optimized spectra and a CMOS panel detector" by M. D. Jensen, S. Dawson, J. Chen, and E. Wong.

1.9.4 Chapter 5: Conclusions

In the final chapter, the conclusions of the prior chapters are summarized. Future work is discussed. In summary, a small animal irradiator has been designed and constructed with a more versatile collimation system and dual energy on-board CT scanning for image guidance. Dual energy micro-CT was investigated for measuring phantom and in vivo tissue density and atomic number for improving Monte Carlo dose calculation. This addresses some of the

limitations of previously-available systems and will enable preclinical investigations into the radiobiology of the biologically-guided radiotherapy of the future.

1.10 References

[1]D. Hanahan and R. A. Weinberg, "The hallmarks of cancer", Cell **100**, 57–70 (2000).

[2]D. Hanahan and R. A. Weinberg, "Hallmarks of cancer: the next generation", Cell **144**, 646–674 (2011).

[3]Canadian Cancer Society's Advisory Committee on Cancer, *Canadian Cancer Statistics 2014*, tech. rep. (Canadian Cancer Society, Toronto, ON, 2014).

[4]F. R. Eilber, "Principles of cancer surgery", in *Cancer treatment*, edited by C. M. Haskell and J. S. Berek, 5th ed. (W. B. Saunders Company, Philadelphia, PA, 2001) Chap. 5, pp. 47–52.

[5]R. G. Parker and H. R. Withers, "Principles of radiation oncology", in *Cancer treatment*, edited by C. M. Haskell and J. S. Berek, 5th ed. (W. B. Saunders Company, Philadelphia, PA, 2001) Chap. 5, pp. 52–62.

[6]C. M. Haskell, "Principles of cancer chemotherapy", in *Cancer treatment*, edited by C. M. Haskell and J. S. Berek, 5th ed. (W. B. Saunders Company, Philadelphia, PA, 2001) Chap. 5, pp. 62–86.

[7]M. S. Mitchell, "Principles of biologic therapy", in *Cancer treatment*, edited by C. M. Haskell and J. S. Berek, 5th ed. (W. B. Saunders Company, Philadelphia, PA, 2001) Chap. 5, pp. 86–103.

[8]T. Pham and L. Holle, *Cancer therapy: prescribing and administration basics* (Jones & Bartlett Learning, Burlington, MA, 2015), p. 4.

[9]W. M. Mendenhall, A. A. Mancuso, R. J. Amdur, and J. W. Werning, "Laryngeal cancer", in *Perez and Brady's principles and practice of radiation oncology*, edited by E. C. Halperin, D. E. Wazer, C. A. Perez, and L. W. Brady, 6th ed. (Wolters Kluwer Health/Lippincott Williams & Wilkins, Philadelphia, PA, 2013) Chap. 47, pp. 850–868.

[10]D. N. Kim, M. Story, and H. Choy, "Basic concepts of chemotherapy and irradiation interaction", in *Perez and Brady's principles and practice of radiation oncology*, edited by E. C. Halperin, D. E. Wazer, C. A. Perez, and L. W. Brady, 6th ed. (Wolters Kluwer Health/Lippincott Williams & Wilkins, Philadelphia, PA, 2013) Chap. 32, pp. 604–623.

[11]E. J. Hall and A. J. Giaccia, *Radiobiology for the radiologist*, 6th ed. (Wolters Kluwer Health/Lippincott Williams & Wilkins, Philadelphia, PA, 2006).

[12]A. Ahnesjö, B. Hårdemark, U. Isacsson, and A. Montelius, "The IMRT information process–mastering the degrees of freedom in external beam therapy", Phys. Med. Biol. **51**, R381–R402 (2006).

[13]L. A. Dawson and M. B. Sharpe, "Image-guided radiotherapy: rationale, benefits, and limitations", Lancet Oncol. **7**, 848–858 (2006).

[14]D. I. Thwaites and J. B. Tuohy, "Back to the future: the history and development of the clinical linear accelerator", Phys. Med. Biol. **51**, R343–R362 (2006).

[15]D. Verellen, M. D. Ridder, and G. Storme, "A (short) history of image-guided radiotherapy", Radiother. Oncol. **86**, 4–13 (2008).

[16]J.-Y. Jin, N. Wen, L. Ren, C. Glide-Hurst, and I. J. Chetty, "Advances in treatment techniques", Cancer J. **17**, 166–176 (2011).

[17]K. T. Butterworth, K. M. Prise, and F. Verhaegen, "Small animal image-guided radiotherapy: status, considerations and potential for translational impact", Brit. J. Radiol. **88**, 20140634 (2015).

[18]T. Bortfeld, "IMRT: a review and preview", Phys. Med. Biol. **51**, R363–79 (2006).

[19]T. R. Mackie, J. Kapatoes, K. Ruchala, W. Lu, C. Wu, G. Olivera, L. Forrest, W. Tome, J. Welsh, R. Jeraj, P. Harari, P. Reckwerdt, B. Paliwal, M. Ritter, H. Keller, J. Fowler, and M. Mehta, "Image guidance for precise conformal radiotherapy", Int. J. Radiat. Oncol., Biol., Phys. **56**, 89–105 (2003).

[20]W. Schlegel, "If you can't see it, you can miss it: the role of biomedical imaging in radiation oncology", Radiat. Prot. Dosim. **139**, 321–326 (2010).

[21]S. Webb, "Motion effects in (intensity modulated) radiation therapy: a review", Phys. Med. Biol. **51**, R403–R425 (2006).

[22]J. Boda-Heggemann, F. Lohr, F. Wenz, M. Flentje, and M. Guckenberger, "kV cone-beam CT-based IGRT: a clinical review", Strahlenther. Onkol. **187**, 284–91 (2011).

[23]K. Nakamura, T. Sasaki, S. Ohga, T. Yoshitake, K. Terashima, K. Asai, K. Matsumoto, Y. Shioyama, and H. Honda, "Recent advances in radiation oncology: intensity-modulated radiotherapy, a clinical perspective", Int. J. Clin. Oncol. **19**, 564–569 (2014).

[24]C. C. Ling, J. Humm, S. Larson, H. Amols, Z. Fuks, S. Leibel, and J. A. Koutcher, "Towards multidimensional radiotherapy (MD-CRT): biological imaging and biological conformality", Int. J. Radiat. Oncol., Biol., Phys. **47**, 551–560 (2000).

[25]S. M. Bentzen and V. Gregoire, "Molecular imaging-based dose painting: a novel paradigm for radiation therapy prescription", Semin. Radiat. Oncol. **21**, 101–110 (2011).

[26]T. Z. Vern and W. Small, Jr., "Targeted therapies: definitions, limitations, and future directions", in *Combining targeted biological agents with radiotherapy: current status and future directions*, edited by W. Small, Jr. (Demos Medical Publishing, New York, NY, 2008) Chap. 1, pp. 1–15.

[27]E. R. Mardis and R. K. Wilson, "Cancer genome sequencing: a review", Hum. Mol. Genet. **18**, R163–R168 (2009).

[28]D. A. Torigian, S. S. Huang, M. Houseni, and A. Alavi, "Functional imaging of cancer with emphasis on molecular techniques", CA-Cancer J. Clin. **57**, 206–224 (2007).

[29]G. A. M. S. van Dongen, A. J. Poot, and D. J. Vugts, "PET imaging with radiolabeled antibodies and tyrosine kinase inhibitors: immuno-PET and TKI-PET", Tumor Biol. **33**, 607–615 (2012).

[30]C. Peyssonnaux and A. Eychène, "The Raf/MEK/ERK pathway: new concepts of activation", Biol. Cell **93**, 53–62 (2001).

[31]H. Davies, G. R. Bignell, C. Cox, P. Stephens, S. Edkins, S. Clegg, J. Teague, H. Woffendin, M. J. Garnett, W. Bottomley, N. Davis, E. Dicks, R. Ewing, Y. Floyd, K. Gray, S. Hall, R. Hawes, J. Hughes, V. Kosmidou, A. Menzies, C. Mould, A. Parker, C. Stevens, S. Watt, S. Hooper, R. Wilson, H. Jayatilake, B. A. Gusterson, C. Cooper, J. Shipley, D. Hargrave, K. Pritchard-Jones, N. Maitland, G. Chenevix-Trench, G. J. Riggins, D. D. Bigner, G. Palmieri, A. Cossu, A. Flanagan, A. Nicholson, J. W. C. Ho, S. Y. Leung, S. T. Yuen, B. L. Weber, H. F. Seigler, T. L. Darrow, H. Paterson, R. Marais, C. J. Marshall, R. Wooster, M. R. Stratton, and P. A. Futreal, "Mutations of the BRAF gene in human cancer", Nature **417**, 949–54 (2002).

[32]G. A. McArthur, P. B. Chapman, C. Robert, J. Larkin, J. B. Haanen, R. Dummer, A. Ribas, D. Hogg, O. Hamid, P. A. Ascierto, C. Garbe, A. Testori, M. Maio, P. Lorigan, C. Lebbé, T. Jouary, D. Schadendorf, S. J. O'Day, J. M. Kirkwood, A. M. Eggermont, B. Dréno, J. A. Sosman, K. T. Flaherty, M. Yin, I. Caro, S. Cheng, K. Trunzer, and A. Hauschild, "Safety and efficacy of vemurafenib in BRAF(V600E) and BRAF(V600K) mutation-positive melanoma (BRIM-3): extended follow-up of a phase 3, randomised, open-label study", Lancet Oncol. **15**, 323–32 (2014).

[33]I. W. Y. Mak, N. Evaniew, and M. Ghert, "Lost in translation: animal models and clinical trials in cancer treatment", Am. J. Transl. Res. **6**, 114–118 (2014).

[34]M. Ingrisch and S. Sourbron, "Tracer-kinetic modeling of dynamic contrast-enhanced MRI and CT: a primer", J. Pharmacokinet. Pharmacodyn. **40**, 281–300 (2013).

[35]C. Marcus, V. Ladam-Marcus, C. Cucu, O. Bouché, L. Lucas, and C. Hoeffel, "Imaging techniques to evaluate the response to treatment in oncology: current standards and perspectives", Crit. Rev. Oncol. Hematol. **72**, 217–238 (2009).

[36]F. Verhaegen, P. Granton, and E. Tryggestad, "Small animal radiotherapy research platforms", Phys. Med. Biol. **56**, R55–R83 (2011).

[37]M. A. Khan, J. Van Dyk, I. W. T. Yeung, and R. P. Hill, "Partial volume rat lung irradiation; assessment of early dna damage in different lung regions and effect of radical scavengers", Radiother. Oncol. **66**, 95–102 (2003).

[38]N. S. Bese, C. Umay, S. Serdengecti, N. Kepil, N. Sut, T. Altug, and A. Ober, "The impact of trastuzumab on radiation-induced pulmonary fibrosis: results of an experimental study", Med. Oncol. **27**, 1415–9 (2010).

[39]Z. N. Rabbani, J. Mi, Y. Zhang, M. Delong, I. L. Jackson, K. Fleckenstein, F. K. Salahuddin, X. Zhang, B. Clary, M. S. Anscher, and Z. Vujaskovic, "Hypoxia inducible factor 1α signaling in fractionated radiation-induced lung injury: role of oxidative stress and tissue hypoxia", Radiat. Res. **173**, 165–74 (2010).

[40]T. Eldh, F. Heinzelmann, a. Velalakan, W. Budach, C. Belka, and V. Jendrossek, "Radiation-induced changes in breathing frequency and lung histology of C57BL/6J mice are time- and dose-dependent", Strahlenther. Onkol. **188**, 274–81 (2012).

[41]J. Wong, E. Armour, P. Kazanzides, I. Iordachita, E. Tryggestad, H. Deng, M. Matinfar, C. Kennedy, Z. Liu, T. Chan, O. Gray, F. Verhaegen, T. McNutt, E. Ford, and T. DeWeese, "High-resolution, small animal radiation research platform with x-ray tomographic guidance capabilities", Int. J. Radiat. Oncol., Biol., Phys. **71**, 1591–1599 (2008).

[42]M. Matinfar, E. Ford, I. Iordachita, J. Wong, and P. Kazanzides, "Image-guided small animal radiation research platform: calibration of treatment beam alignment", Phys. Med. Biol. **54**, 891–905 (2009).

[43]R. Clarkson, P. Lindsay, S. Ansell, G. Wilson, S. Jelveh, R. Hill, and D. Jaffray, "Characterization of image quality and image-guidance performance of a preclinical microirradiator", Med. Phys. **38**, 845–856 (2011).

[44]W. van Elmpt, L. McDermott, S. Nijsten, M. Wendling, P. Lambin, and B. Mijnheer, "A literature review of electronic portal imaging for radiotherapy dosimetry", Radiother. Oncol. **88**, 289–309 (2008).

[45]P. V. Granton, M. Podesta, G. Landry, S. Nijsten, G. Bootsma, and F. Verhaegen, "A combined dose calculation and verification method for a small animal precision irradiator based on onboard imaging", Med. Phys. **39**, 4155–4166 (2012).

[46]P. V. Granton and F. Verhaegen, "On the use of an analytic source model for dose calculations in precision image-guided small animal radiotherapy", Phys. Med. Biol. **58**, 3377–3395 (2013).

[47]S. J. van Hoof, P. V. Granton, and F. Verhaegen, "Development and validation of a treatment planning system for small animal radiotherapy: SmART-Plan", Radiother. Oncol. **109**, 361–366 (2013).

[48]H. Zhou, M. Rodriguez, F. Van Den Haak, G. Nelson, R. Jogani, J. Xu, X. Zhu, Y. Xian, P. Tran, D. Felsher, P. Keall, and E. Graves, "Development of a micro-computed tomography-based image-guided conformal radiotherapy system for small animals", Int. J. Radiat. Oncol., Biol., Phys. **78**, 297–305 (2010).

[49]M. Rodriguez, H. Zhou, P. Keall, and E. Graves, "Commissioning of a novel microCT/RT system for small animal conformal radiotherapy", Phys. Med. Biol. **54**, 3727–3740 (2009).

[50]E. Graves, H. Zhou, R. Chatterjee, P. Keall, S. Gambhir, C. Contag, and A. Boyer, "Design and evaluation of a variable aperture collimator for conformal radiotherapy of small animals using a microCT scanner", Med. Phys. **34**, 4359–4367 (2007).

[51]P. Keall, G. Mageras, J. Balter, R. Emery, K. Forster, S. Jiang, J. Kapatoes, D. Low, M. Murphy, B. Murray, C. Ramsey, M. Van Herk, S. Vedam, J. Wong, and E. Yorke, "The management of respiratory motion in radiation oncology report of AAPM Task Group 76", Med. Phys. **33**, 3874–3900 (2006).

[52]J. H. Hubbell and S. M. Seltzer, *Tables of X-Ray Mass Attenuation Coefficients and Mass Energy-Absorption Coefficients from 1 keV to 20 MeV for Elements Z = 1 to 92 and 48 Additional Substances of Dosimetric Interest (Version 1.4)*, tech. rep. (National Institute of Standards and Technology, Gaithersburg, MD, 2004).

[53]M. Bazalova and E. Graves, "The importance of tissue segmentation for dose calculations for kilovoltage radiation therapy", Med. Phys. **38**, 3039–3049 (2011).

[54]D. W. O. Rogers, "Fifty years of monte carlo simulations for medical physics", Phys. Med. Biol. **51**, R287–R301 (2006).

[55]R. A. Rutherford, B. R. Pullan, and I. Isherwood, "Measurement of effective atomic number and electron density using an EMI scanner", Neuroradiology **11**, 15–21 (1976).

[56]B. J. Heismann, J. Leppert, and K. Stierstorfer, "Density and atomic number measurements with spectral x-ray attenuation method", J. Appl. Phys. **94**, 2073 (2003).

Chapter 2

Implementation and commissioning of an integrated micro-CT/RT system with computerized independent jaw collimation

This chapter is adapted from the research article "Implementation and commissioning of an integrated micro-CT/RT system with computerized independent jaw collimation". Reprinted with permission from M. D. Jensen, W. T. Hrinivich, J. A. Jung, D. W. Holdsworth, M. Drangova, J. Chen and E. Wong, Medical Physics **40**, 081706 (2013).

© 2013 American Association of Physicists in Medicine

doi:10.1118/1.4812422

2.1 Introduction

Technology development of preclinical irradiators has lagged compared to clinical systems in regards to providing conformal intensity-modulated therapy with onboard image guidance. The limitation to deliver sophisticated radiation treatments to small animals has hindered translating radiobiological studies to the clinic.[1] Several groups have worked to bring image-guided conformal radiation therapy technology to small animal laboratories. The first group of irradiators have been designed and constructed specifically for image guided small animal therapy. These systems include the SARRP from John Hopkins and Xstraal,[2,3] and the X-RAD 225Cx from Princess Margaret Hospital and Precision X-Ray.[4] Several other groups have purchased these

or other systems, and have published on their capabilities. The Maastricht group has developed a dose verification technique for the X-RAD 225Cx,[5] while the group at University of Texas Southwestern Medical Center has characterized an X-RAD 320.[6] Others have constructed radioisotope based systems, such as the Washington University group.[7,8] The last approach has been to modify a micro-CT scanner to enable irradiations, the primary example is the system at Stanford.[9–12]

The Stanford system is based on a previous generation micro-CT (GE eXplore RS120) with factory standard x-ray generator, using commercial imaging control software utilizing only the small focal spot.[12] A motorized variable-aperture collimator was added to define pseudocircular profiles of arbitrary width between 0.1 and 6.0 cm.[12] A two-dimensional translation stage was added to the couch to position the target at isocenter for irradiation, limiting the system to mouse radiotherapy.[9]

In this work, we report a different modification of micro-CT scanner for RT purposes. The three major enhancements are a computerized asymmetric jaw collimator, integrated therapy control software, and gated therapy. The computerized asymmetric jaw is the next level of sophistication in small animal collimation. Most systems, such as the SARRP and X-RAD 225Cx, still use manual static cone collimators. The Stanford collimator is the only other computerized collimator known to the authors. However, the Stanford collimator effectively emulates an extensive set of circular cones, and is unable to form asymmetric fields. Asymmetric jaws provide more flexibility, potentially allowing for more efficient treatment plans.

Software was acquired and developed to integrate the functionality of the CT scanner hardware and collimator hardware, allowing automated synchronized treatment plan delivery.

This modified scanner is the only dedicated small animal IGRT platform known to the authors that can perform gated radiation therapy.

Additional minor upgrades include upsizing to a larger x-ray generator and enhancements to the shielding and cooling. The existing imaging capabilities of the system were retained. In

this paper, we will focus on the design and evaluation of the custom-built motorized orthogonal jaws, and radiation therapy capabilities of the system, including gated delivery.

2.2 Materials and Methods

2.2.1 General design considerations

The desired end capabilities of the system are to irradiate small rodents, primarily mice and rats. Initially, we expect most studies to be improvements over previous non-image guided techniques which often have a larger irradiated volume. In place of irradiating half the animal, we plan to irradiate an entire organ, or a large fraction of the (tumour bearing) organ, utilizing image guidance to reduce margins and ensure target coverage. For example, instead of irradiating the entire rodent thorax, we would irradiate the lower right lung lobe localized by fluoroscopic image guidance. With this in mind, we have focused most of our characterizations on the field sizes ranging from 30 mm to 2 mm. Most systems move the target to isocenter and employed a collimator. However, the design of the micro-CT with a 10 cm diameter bore excludes translating the couch laterally to place the flank tumour on a rat at the isocenter. With this consideration, we designed and implemented a motorized jaw collimator to allow asymmetric beams. Additionally, orthogonal jaws are familiar to the radiation oncology community. With this design, we can utilize techniques such as dynamic wedge, or implement simple jaws only IMRT for small animals in the future.[13,14]

The jaw collimator is mounted on the bore, closer to the subject, as opposed to at the tube exit window. Several reasons lead us to this design decision. First, by being closer to the subject, we reduce geometric penumbra. Second, by reducing the magnification factor, small positioning errors in the jaws are not magnified to large errors. The reduction of magnification allows us to build larger components with more generous mechanical error tolerances, which reduces manufacturing and design time.

2.2.2 Hardware

2.2.2.1 Micro-CT/RT

The base hardware of the image guided small animal irradiator system is a GE eXplore CT 120 (GE Healthcare, Milwaukee WI USA). We have upgraded to a 50 kW x-ray generator (Indico 100, CPI Georgetown ON, Canada) that replaces the factory standard 32 kW generator and enables the x-ray tube to be operated at 140 kVp. We use the factory standard x-ray tube (PX1483, Dunlee, Aurora, IL, USA) with dual focal spot sizes of 0.3 mm and 1.0 mm. The beam is filtered by the equivalent of 4.5 mm of aluminum. A sagittal laser was added to the system to complement the factory standard axial and coronal lasers to allow for identification of the treatment isocenter. The imaging capabilities of this scanner model were reported by Bahri et al.[15] using the vmCT phantom.[16]

2.2.2.2 Collimator

A CAD rendering and photos of the collimator are given in figure 2.1. The collimator was designed to clamp onto the bore of the micro-CT. Supporting electronics and power supplies were mounted on a custom plate, designed to attach to the micro-CT gantry using pre-existing threaded holes.

The collimator consists of two jaw pairs. The x jaws move orthogonal to the CT axis of rotation, and are independently controlled. The y jaws are symmetric, and move parallel to the CT axis of rotation. The jaws are moved by three stepper motors (Wantai Motor Co. Ltd., Changzhou City, Jiangsu, China), two for the x jaws, and one for the y jaws. All jaw positions are monitored with capacitive encoders (CUI Inc., Tualatin OR, USA). A limit switch at the end of each jaw track is used to calibrate the jaw position at system startup. Motor control and encoder readout is provided by control boards with USB interfaces (Phidgets Inc., Calgary AB, Canada). A small single board computer running embedded Linux (Phidgets Inc.) is attached to the USB interface boards and provides overall control and communication for the collimator.

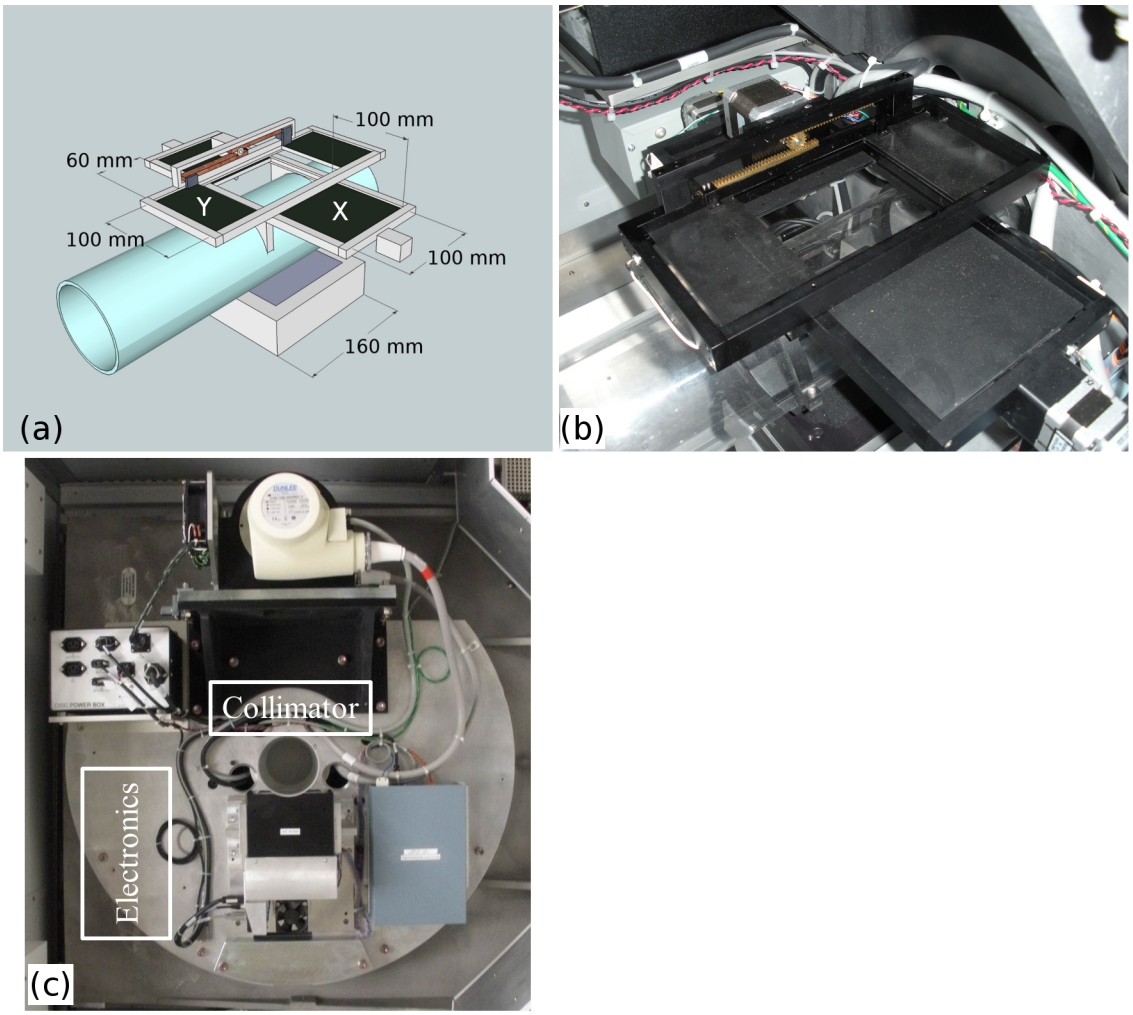

Figure 2.1: CAD rendering of the computer controlled collimator (a). Photo of the jaws mounted on the Micro-CT bore (b). X1 jaw motor and position encoder are visible in lower right of the figure. Y jaw rack and pinion motor drive is visible in upper right of the figure. Photo of micro-CT gantry before collimator installation (c). The collimator mounts onto the micro-CT bore, sitting above the detector assembly. The support electronics mount onto the gantry.

This single board computer is mounted on the gantry, and communicates to the console over Ethernet.

All jaws consist of a polyoxymethylene base laminated with 1 mm of lead. The x jaws translate by a lead screw mechanism. The y jaws are moved with a rack and pinion mechanism. The frame structure was fabricated in aluminum and assembled by the department machine shop.

2.2.3 Software

Collimator controller software was written in C, making use of the software libraries provided with the USB interface boards (Phidgets Inc.). Collimator console software was written in Java.

Third-party radiation therapy (RT) control software (Parallax Innovations, London ON, Canada) was used in place of the factory supplied micro-CT control software. The custom RT software controls all aspects of the system and allows defining treatment protocols and accessing modes of operation of the micro-CT hardware that were not available in the factory console software. For example, the RT software allows us to irradiate using the large focal spot at 140 kVp, as opposed to the factory software that restricts exposures to the small focal spot and 120 kVp. Additionally, an interface between the RT software and collimator software allows for automated delivery of conformal and simple step-and-shoot plans.

2.2.4 System calibration and performance characterization

We first verified the system's isocenter by placing a small ball bearing (BB) on the couch and images were acquired from multiple directions. The images of the BB were compared to the results of the CT image reconstruction calibration. The BB position was iteratively adjusted until the BB images agreed with the reconstruction parameters. The lasers were then adjusted such that they intersected at the corrected BB position.

2.2.4.1 Jaw position calibration and accuracy assessment

Each of the collimator jaws were stepped across the full beam width in increments of approximately 1 cm. Fluoroscopy images were acquired of the shadows cast by the jaws at each position. Line profiles were then taken perpendicular to the jaw edge in the fluoroscopy images, and the position of the half maximum intensity was determined. A jaw position lookup table was then compiled using the stepper motor counts and the half maximum intensity positions, and implemented in the software.

Three aspects of the jaw performance were accessed: jaw homing reproducibility, motor control accuracy, and mechanical play and backlash. Jaw homing occurs when the system starts up and moves the jaws to the end of the motion track and trips a mechanical switch to set the home or zero position. To access jaw homing reproducibility, the jaws were homed, subsequently moved to 2 cm from isocenter, and a fluoroscopy image was acquired. This was repeated at 5 gantry positions (0°, 45°, 90°, 180°, 270°) with a total repetition of 54 times, and the standard error of each jaw edge was computed.

For this work, motor control accuracy is defined as the ability of the control software and electronics to rotate the stepper motors the correct number of steps. To assess motor control accuracy, 60 random jaw configurations were selected such that no consecutive jaw configurations were the same (exclude all changes where there would be no jaw movements). The jaws were then moved to each of the random jaw positions and the encoder position was recorded. Recall that the encoders are used for independent verification of position, and are not used as feedback to the motor control.

Mechanical play and backlash is the error attributed to the play or slop in the gears and lead screws. Backlash is a consistent error that occurs when the system changes direction. Mechanical play and backlash in the x jaw mechanisms were accessed by stepping the jaws to three consecutive positions, and then reversing direction and stepping to the previous positions. For example, the x1 jaw was moved in the order from 30 mm to 20 mm, 10 mm, 20 mm, and back to 30 mm. The jaw edge position was determined using fluoroscopic imaging as described

above and repeated four times. Mechanical play and backlash in the y jaws were accessed with the same procedure.

We recognize the limitation of these tests in separating the three effects. However, each test gives a reasonable estimation of the desired effect while minimizing the influence of the other effects.

All jaw position and speed measurements were scaled to be at isocenter for reporting.

2.2.5 Dosimetry

2.2.5.1 Measurements

2.2.5.1.1 Exposure settings All measurements were completed at 140 kV, 50 mA and 25 ms pulse duration, with 220 ms between pulses using the large focal spot, unless otherwise stated.

2.2.5.1.2 Jaw Transmission The jaws were closed, and the transmission measured with the Farmer type ion chamber.

2.2.5.1.3 Output Beam output was measured using a 0.6 cm^3 Farmer chamber (type 30013, PTW, Freiburg Germany) inside a $70 \times 70 \times 20$ mm^3 solid water block. This chamber was cross compared to the local standards at beam energies ranging from 80 kV to 18 MV, and found to be in agreement. Symmetric square fields of 60×60, 50×50, 40×40 and 30×30 cm^2 were centered on the active volume of the ion chamber, and irradiated with 500 pulses.

2.2.5.1.4 Radiochromic film processing Radiochromic film (EBT2, Ashland Inc., Covington KY, USA) was digitized at 72 dpi using a transmission mode flatbed scanner (Expression 10000XL, Seiko Epson Corp., Suwa, Nagano, Japan). Film processing was based on work by Devic et al.[17,18] and McCaw et al.,[19] and is described in detail in appendix A. The film was calibrated for the range of 0 to 8 Gy by comparison with ion chamber measurements.

2.2.5.1.5 Absolute depth dose Absolute depth dose was measured using a cubic solid water and radiochromic film phantom with dimensions of $50 \times 50 \times 50$ mm^3. The films were scanned and converted to dose. Symmetric fields of sizes 40×40 and 20×20 mm^2 were examined with 24 films perpendicular to the beam axis, separated by 2 mm of solid water. Similarly, a 2×2 mm^2 field was characterized with 12 films placed every 4 mm at different depths.

2.2.5.1.6 Beam profiles (FWHM, symmetry, flatness, penumbra) Beam profiles of symmetric fields of sizes 60×60, 50×50, 40×40, 30×30, 20×20, 10×10, 5×5 and 2×2 mm^2 were also examined using EBT2 radiochromic film at isocentre, at a depth of 2 and 12 mm in a solid water phantom. Only the films at a depth of 12 mm are presented. The FWHM was calculated as the width of the beam at 50% the maximum intensity. Beam symmetry was quantified based on the left-side and right-side dose of the beam profile at 80% of the FWHM using

$$S = \max\left(100 \times \frac{D_{\text{left}} - D_{\text{right}}}{D_{\text{left}} + D_{\text{right}}}\right). \tag{2.1}$$

Flatness was computed by finding the maximum and minimum dose in the middle 80% extent of the beam profile and applying

$$F = 100 \times \frac{D_{\text{max}} - D_{\text{min}}}{D_{\text{max}} + D_{\text{min}}}. \tag{2.2}$$

Penumbra was calculated by computing the distance between the points of 20% and 80% maximum dose.

2.2.5.1.7 Beam profile with asymmetric field A 30×30 mm field, off-axis by 10 mm was delivered to a film at isocentre at a depth of 12 mm in solid water. Two 10×10 mm fields, off-axis by 15 and 25 mm were also delivered to film at isocentre.

2.2.5.2 Monte Carlo modeling

We used the Monte Carlo package EGSnrc.[20,21] A Monte Carlo beam model of the system was built in BEAMnrc,[22] with dose calculations performed in DOSXYZnrc.[23] We used the work by Bazalova et al.[11] to develop the model. The XTUBE component module was configured to the manufacturer's published specifications of the x-ray tube (anode angle, material composition, geometry). The electron source is modelled as a parallel circular beam of radius 0.5 mm for the large focal spot to approximate the effective spot size of 1 mm. The simulation output was calibrated against the ion chamber output measurements. The model was verified by comparing the beam profiles of the simulations to the film measurements for symmetric fields of sizes 60 $\times$ 60, 50 $\times$ 50, 40 $\times$ 40, 30 $\times$ 30, 20 $\times$ 20, 10 $\times$ 10, 5 $\times$ 5 and 2 $\times$ 2 mm^2 and asymmetric fields of sizes 10 $\times$ 10 mm^2 and 30 $\times$ 30 mm^2. Modeled absolute depth dose curves were compared to measured ones for the following field sizes: 40 $\times$ 40, 20 $\times$ 20, and 2 $\times$ 2 mm^2.

Monte Carlo simulations were run with sufficient histories such that in the high dose regions, the reported uncertainty was 3% or less.

2.2.5.3 Focal spot size

One difference between the Stanford system and this system is the use of the large focal spot. Two films were exposed with 2 $\times$ 2 mm^2 fields, the first using the small focal spot, and the second using the large focal spot. The two fields with different focal spot sizes were also modelled with Monte Carlo.

2.2.6 Elliptical target

Two simple 3D conformal plans to irradiate a 20 mm $\times$ 10 mm elliptical cylinder target were used to qualitatively access overall machine performance. One plan consisted of 9 beam directions, and the second 31 beam directions. Film was sandwiched vertically in a solid water

cube with side lengths of 50 mm. The films were examined for asymmetry that would indicate gantry sag, or collimator malfunctions.

2.2.7 Image guidance

A simple phantom was constructed with three non-metallic 2.3 mm BBs (CT-SPOT, Beekley Medical, Bristol, CT, USA) inside the interior of a cubic polystyrene phantom. The phantom could be split to insert a radiochromic film. One BB, not at isocenter, was localized by CT imaging. A plan to irradiate the BB was manually generated with four asymmetric beams of 5×5 mm^2 centered on the BB. The phantom was removed and replaced onto the couch and repositioned using fluoroscopy guidance. The phantom with film was then irradiated with the four beam plan. The targeting accuracy was verified by examination of the radiochromic film and comparing the centroid of the BB and the high dose region. This was repeated 6 times to access repositioning accuracy.

2.2.8 Respiratory gating

We have performed a number of pilot gated rat lung irradiations in collaboration with a MR imaging group (G. Santyr) at our institution. All procedures followed animal care protocols approved by the University of Western Ontario (ACVS) and were consistent with procedures used by the Canadian Council on Animal Care (CCAC).

From a cohort of 12 200–250 g Sprague-Dawley rats, we estimated the diaphragm motion to be approximately 5 mm at a breath rate of 50–60 breaths per minute free breathing under 1–2% isoflurane. One technique to compensate for motion is to gate the delivery. This system is capable of performing gated imaging with the addition of a small animal physiology monitoring system. We adapt the gated imaging scanner hardware for gated radiation therapy. While the diagnostic imaging x-ray system is disadvantageous for producing a high dose rate compared to therapy tubes, one advantage is the fine control over the x-ray exposure timing. Normally the system is operated with a 10% duty cycle to balance heat accumulation and continuous x-

ray pulsing. For a gated delivery, the x-ray exposure is triggered to occur during the breathing window with an extended duration to maintain a 10% duty cycle. The duration of the therapy exposure is adjusted to match the breathing rate of the animal and maintain close to a 10% duty cycle. Hence, we managed to deliver gated treatments in the same amount of time as normal un-gated treatments. A sample of the respiratory trace and gating window from the animal monitoring system is shown in figure 2.2. Also shown are the duration and timing of x-ray exposures for a non-gated and gated irradiation.

A prototype small animal respiratory motion phantom was constructed, with variable period control (figure 2.3). The phantom moves a platform in a sinusoidal motion with a frequency of 0.83 Hz (imitating an anesthetized rat breath rate of 50 breaths per minute), with a peak to peak amplitude of 5 mm. The phantom provides a gating signal by squeezing the same respiratory pillow used with small animals. The small animal monitoring system (SA Instruments, Inc. Stony Brook NY, USA) generated a gating window from the respiratory signal. The gating output of the small animal monitoring system was connected to the built-in gating hardware of the micro-CT scanner. With the custom RT software, the x-ray exposure is triggered at the start of the gating window for an irradiation type delivery. The pulse duration was changed from 25 ms to 125 ms to match the breath rate. A radiochromic film was placed on the motion platform and a dose of 2 Gy to a field size of 20×20 mm^2 was delivered with respiratory gating. A second film was exposed with no gating, and a third with no motion.

A rat's thorax was scanned using the micro-CT (70 kVp, 32 mA) first without gating, and then with respiratory gating. Since the same systems of microCT hardware and animal monitoring are used to gate the image acquisition and to gate therapy, the quality of the gated image is a surrogate to the quality of the gated delivery in an animal.

2.2.8.1 Example animal IGRT

A cohort of Sprague-Dawley rats were irradiated to 18 Gy in their right lung. Equally weighted parallel opposed oblique beams were employed to spare the left lung and heart. The fields were

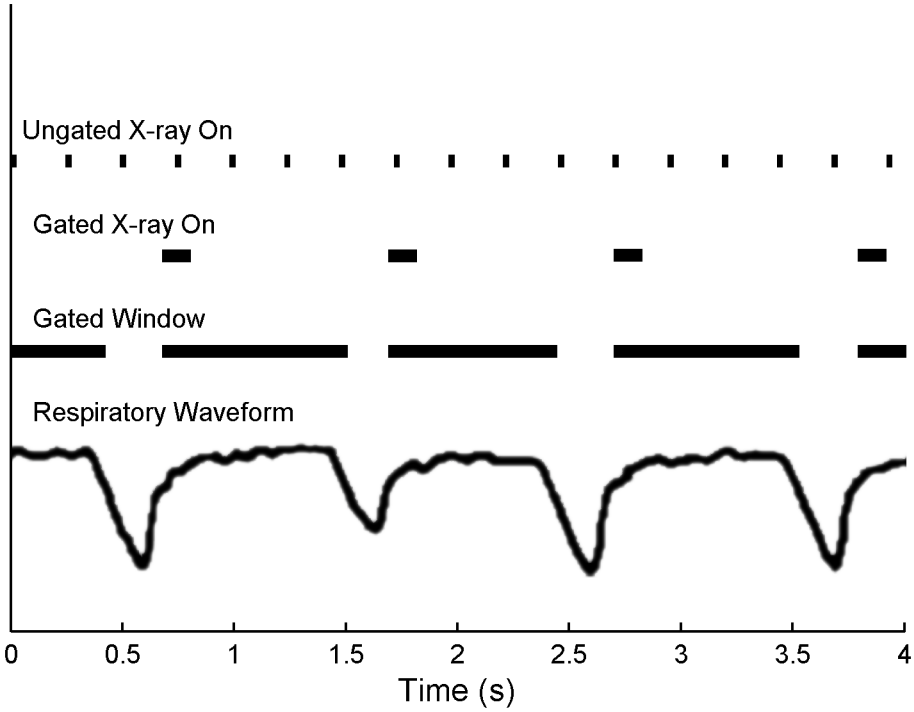

Figure 2.2: Sample of the respiratory waveform and gating window produced by the small animal monitoring system. Inspiration coincides with the valleys in the waveform. Shown at the top is the ungated x-ray exposure protocol of 25 ms pulses separated by 220 ms. For a gated delivery the exposure is triggered by the beginning of the gated window. The exposure duration is chosen to achieve close to a 10 percent duty cycle. For this figure, the respiration period is approximately 1080 ms, with an exposure duration of 125 ms.

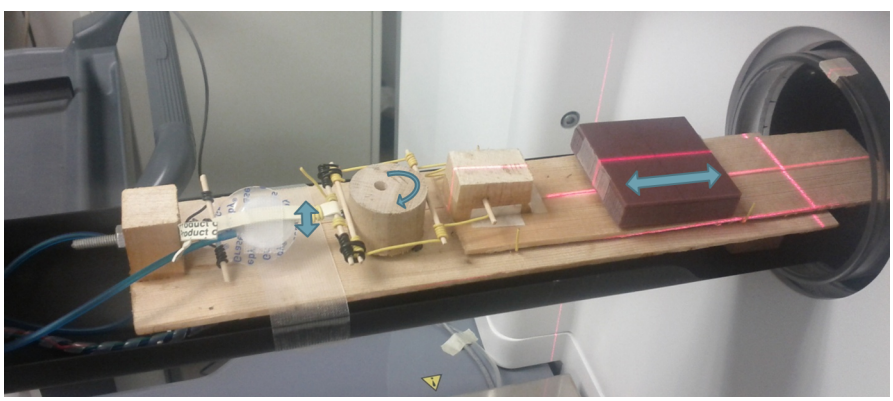

Figure 2.3: Motion phantom used to test respiratory gating functionality. A speed adjustable rotating cam causes a platform to move sinusoidally, with a solid water block and radiochromic film. Simultaneously, an elastic band is stretched, compressing the small animal respiratory pillow creating the gating signal for the micro-CT scanner.

placed using fluoroscopic guidance, ensuring the heart, spine and diaphragm were shielded. An optimal gantry angle is first chosen using fluoroscopic imaging to spare the heart and spine. The jaws are then positioned to shield the heart, spine and diaphragm. The gantry and jaw parameters and pre-treatment CT images from the treatment were used to perform a Monte Carlo dose verification calculation. The dose calculation was performed as described above, using the 8-tissue segmentation technique.[24]

2.3 Results

2.3.1 Collimator performance

Jaw measurements are reported at isocenter. The x jaws move with a speed of 7.7 mm/s, while the y jaws move with a speed of 10 mm/s. Jaw transmission was measured to be 1%. Jaw homing repeatability was quantified to have a standard deviation of 0.07 mm in the X jaws, and 0.3 mm in the Y jaws. Repeated random jaw movements showed the average absolute error between the desired jaw position and the encoder position was $(3.5 \pm 0.4)\times10^{-5}$ mm in the x jaws, and $(3.1 \pm 0.4)\times10^{-2}$ mm in the y jaws. A consistent backlash effect is dwarfed by the random error of the jaws. For the mechanical play x jaws test, the mean error was 0.0004 mm, with a standard deviation of 0.003 mm. The y jaws backlash mean error was 0.02 mm, with a standard deviation of 0.08 mm. One explanation is the vibrations of the collimator during operation results in the jaws coming to rest in a random position within the mechanical play envelope, and not consistently resting against the gear face transmitting the force.

The variability in homing the jaws at start-up is the largest source of error, being an order of magnitude larger than the error of the play in the mechanical linkages, and several orders larger than the error in the motor control.

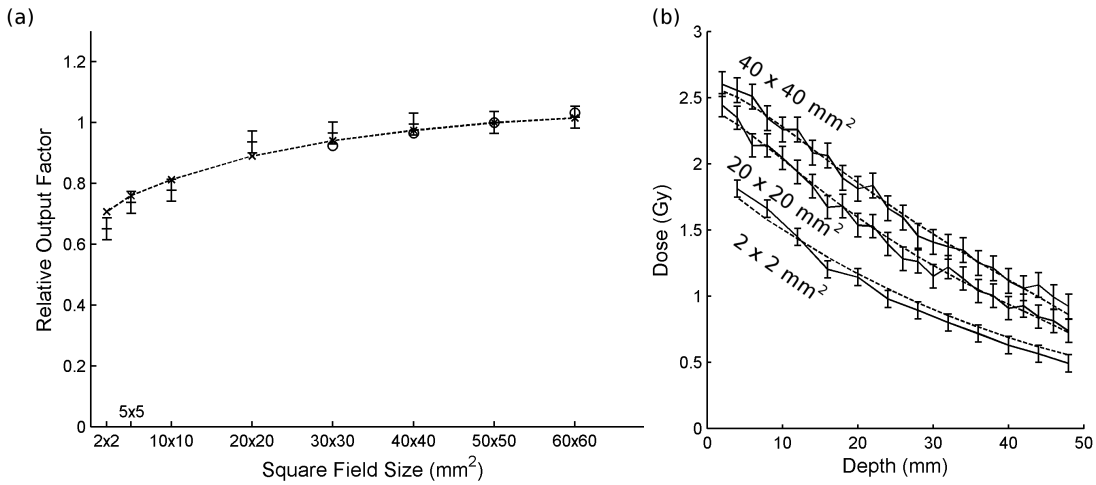

Figure 2.4: Relative output factors for field sizes ranging from 2 × 2 to 60 × 60 mm^2 as measured with EBT2 film (+) and ion chamber (o), and calculated by Monte Carlo (–×–) (a). All measurements were normalized to the 50 × 50 mm^2 field. Error bars for the film are shown. Absolute depth dose in solid water, EBT2 Film and Monte Carlo, for square fields of size 2, 20 and 40 mm^2 (b). Film dose is shown as solid lines with error bars; Monte Carlo dose is shown as dashed lines.

2.3.2 Dosimetry

2.3.2.1 Output

For the reference 50 × 50 mm^2 field, at isocenter and at a depth of 10 mm in solid water, the dose per current-time product (mAs) was measured to be (9.53 ± 0.02)×10^{-4} Gy/mAs. With the heating limitations of the system (10% duty cycle), this works out to an average dose rate of approximately 0.3 Gy/min.

A comparison of relative output factors from ion chamber measurements, film measurements and Monte Carlo simulations is shown in figure 2.4a. Ion chamber measurements and Monte Carlo differ by less than 2%. This very small discrepancy in ion chamber measurement with Monte Carlo could be explained by partial volume effects. All but two of the films agree within the film error of 3.6% with Monte Carlo. The larger discrepancies are the 2 × 2 and 20 × 20 mm^2 fields, with differences of 5.7% and 4.6%.

2.3.2.2 Absolute depth dose

Comparisons of radiochromic film measurements with the Monte Carlo simulations are shown in figure 2.4b. There is good agreement between film and simulation for the larger 40×40 and 20×20 mm^2 fields, with all points falling with the film uncertainty of 3.6% of the dose nearest the surface. The 2×2 mm^2 field shows a consistent 3% disagreement at depths below 24 mm. Nine of twelve film measurements include the Monte Carlo value within the uncertainty of 3.6%, with the largest difference at 5%.

Compared to the Stanford system with an approximate dose decrease of 10% for every 5 mm of depth,[12] this system has an approximate dose decrease of 7.5% with every 5 mm of depth. This result is concurrent with the higher beam energy, and increased beam filtration of 4.5 mmAl compared to 2.5 mmAl.[24,25]

2.3.2.3 Beam profiles

Sample of beam profiles at 12 mm depth are shown in figure 2.5, and the measured parameters, such as FWHM, are presented in table 2.1. The x-ray tube anode heel effect is evident in the superior-inferior beam profiles of the large fields (figure 2.5b). The heel affect is also measured by the deteriorating symmetry and flatness, and the widening penumbra, in the superior-inferior direction compared to the left-right direction in the large 40×40, 50×50 and 60×60 mm^2 fields as shown in table 2.1. There is no flattening filter in the beam, so this result was expected.

The simulations and film agree within the film uncertainty of 3.6% of the maximum dose. On the larger fields, there is some discrepancy in the dose of the tails (figures 2.5a and 2.5b), which is not present for the smaller fields (figures 2.5c and 2.5d). The film shows higher dose than the Monte Carlo simulations in these penumbra tails. One explanation is backscattered photons from the detector, as the detector is not modelled in the simulations.

To compare beam characteristics with the Stanford system, we examine the field sizes of 5×5, 10×10 and 20×20 mm^2 against the pseudo-circular beams of radius 5, 10 and 20 mm. The penumbra of approximately 0.5, 0.6 and 0.7 mm is not far off the values reported by

		Field Size (mm × mm)							
		2 × 2	5 × 5	10 × 10	20 × 20	30 × 30	40 × 40	50 × 50	60 × 60
FWHM	Left-right	2.05	4.98	10.39	20.31	29.81	40.27	49.77	59.54
(mm)	Sup-inf	1.96	5.02	10.00	19.87	29.26	39.56	49.46	59.38
Flatness	Left-right	13.82	4.14	2.44	4.22	4.15	5.30	4.03	5.94
(%)	Sup-inf	15.72	4.40	3.08	3.77	3.05	6.24	7.72	8.75
Symmetry	Left-right	5.22	1.35	0.42	1.20	1.49	2.32	0.67	1.61
(%)	Sup-inf	7.04	1.93	0.53	0.72	0.75	1.96	5.15	3.40
Penumbra	Left-right	0.39	0.54	0.61	0.69	0.75	0.97	0.94	1.30
(mm)	Sup-inf	0.46	0.48	0.57	0.73	0.78	0.97	1.31	2.37

Table 2.1: Beam profile characteristics from EBT2 film measurements at isocenter and 12 mm depth

Rodriguez et al.[12] of 0.45, 0.45 and 0.6 mm. The beam flatness is also similar, with values ranging from 2.4% to 4.4% for this system, compared to 3.4% to 3.7% for the Stanford system. Symmetry is slightly worse for this system, ranging from 0.42% to 1.93% compared to 0.1% to 1.0% for the Stanford system.

Comparison is not straight forward, as the square fields are larger in area than the corresponding pseudo-circular beams resulting in different photon scatter potential. As well, the measurements are taken at 10 mm versus 1 mm depth.

Another consideration is the appropriateness of these metrics for such small beams. For the 2×2 mm^2 field, the flatness metric is very high, 13% to 15%. At this size, the beam won't have a flat region and the flatness measurement is not informative. Similarly, the symmetry metric is also not useful for this small field. As the field gets smaller, the 80% of the maximum dose will fall on a steep gradient, and will cause the symmetry metric to be overly sensitive.

Overall, these results suggest this system has beam characteristics that are suitable for irradiating small animals, and are similar to the existing Stanford system in use.

2.3.2.4 Asymmetric field beam profile

Figures 2.5e and 2.5f show the 10×10 mm^2 field off-axis by 25 mm. The film and simulation agree within the film uncertainty of 3.6% of the maximum dose.

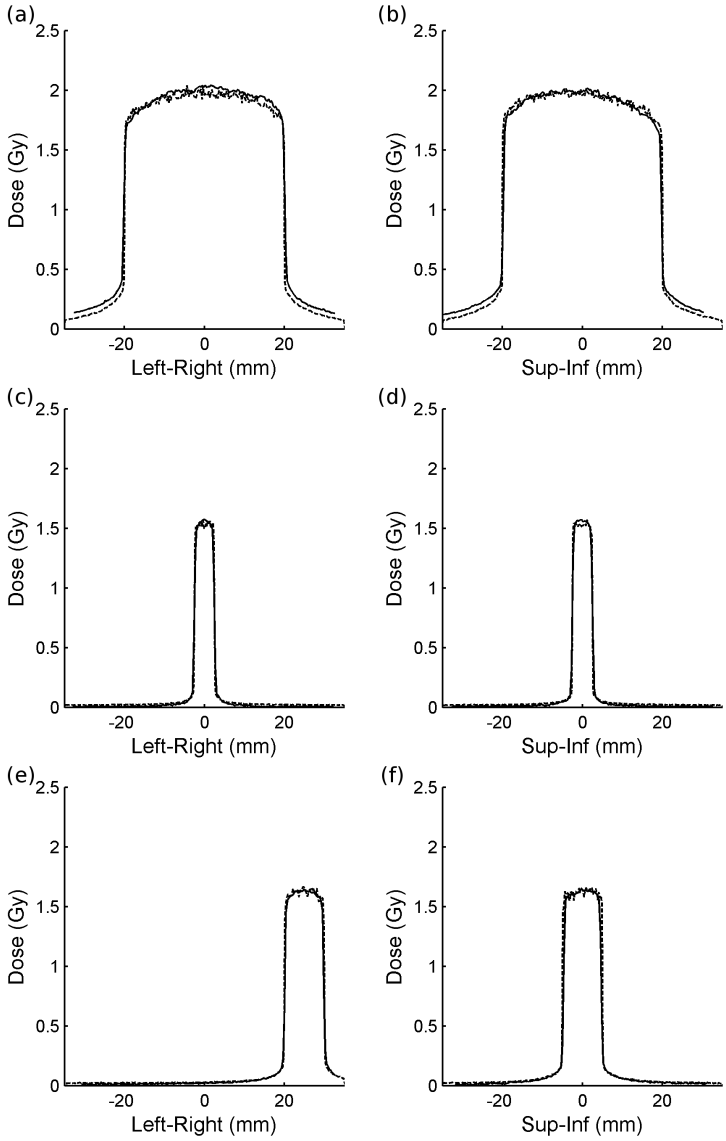

Figure 2.5: Beam profiles at 12 mm depth in a $70 \times 70 \times 22$ mm^3 solid water block. Film profiles have been normalized to ion chamber scaled Monte Carlo. Left-Right (a) and Superior-Inferior (b) profiles of a 40×40 mm^2 field. Left-Right (c) and Superior-Inferior (d) profiles of a 5×5 mm^2 field. Left-Right (e) and Superior-Inferior (f) profiles of a 10×10 mm^2 field, offset from the central axis by 25 mm. Solid lines are film measurements, dashed lines are Monte Carlo.

2.3.2.5 Focal spot size

Results from film measurements and simulations show the differences between the small and large focal spot are within error. Calculations of geometric penumbra for this system are 0.054 and 0.072 mm for x and y jaws for the small focal spot, and 0.18 and 0.24 mm for the large focal spot. These are smaller than the film sampling interval (0.35 mm) and simulation voxel size (0.25 mm). With the collimator mounted closer to the subject, geometric penumbra is minimized, reducing the effect of focal spot size. However, going to the large focal spot for the 2×2 mm^2 field allows for an increase in mA resulting in close to a doubling of the dose rate.

2.3.3 Elliptical target

Elliptical target films are presented in figure 2.6. Qualitatively, the dose distributions look symmetric, indicating good collimator and system performance. No gantry sagging or other overt errors are detected. The high dose region appears uniform. The jaws are able to successfully conform to an elliptical cylindrical target.

2.3.4 Image guidance

One film from the 6 image guidance targeting experiments is shown in figure 2.7. For the five remove-and-replace BB phantom trials, the mean displacement between the BB centroid and the high dose centroid is 0.6 mm, with a standard deviation of 0.1 mm. The maximum and minimum displacements were 0.7 and 0.4 mm.

2.3.5 Gating

The dose distribution to a moving film without gating has a penumbra of 3.9 mm in the motion direction. The gated film has a penumbra of 0.8 mm, and no motion film a penumbra of 0.5 mm. The gated and ungated films are shown in figure 2.8. The reduction of the penumbra in the direction of motion by approximately 80% is quite substantial. The phantom moves in a simple

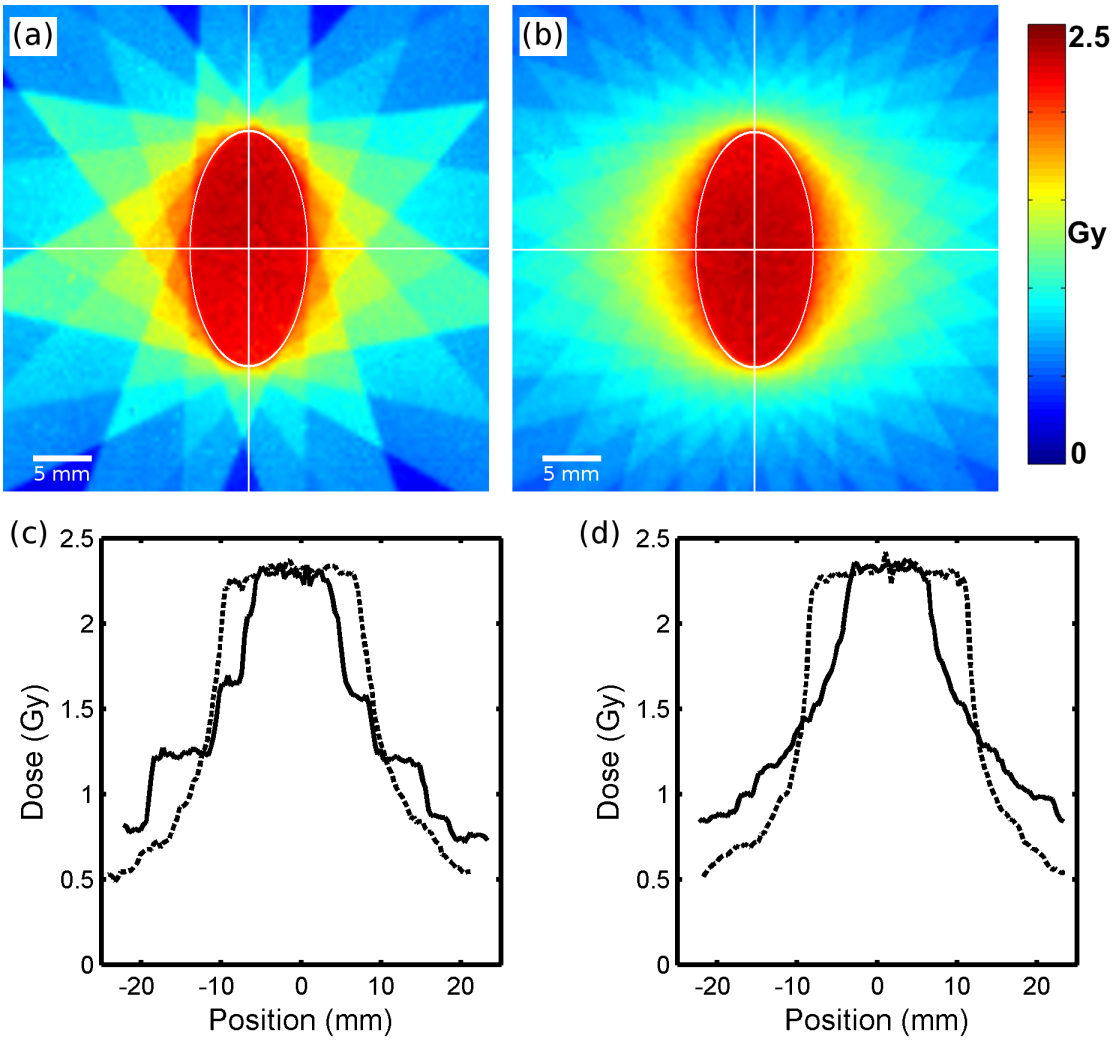

Figure 2.6: Irradiation of an elliptical target (major axis 20 mm, minor axis 10 mm.), measured on EBT2 film. Dose distribution of nine field plan (a) and thirty-one field plan (b). Scale bar is 5 mm. Perpendicular dose profiles through the center of the dose distribution for the nine field plan (c) and the thirty-one field plan (d). Solid lines are the horizontal profiles; dashed lines are the vertical profiles.

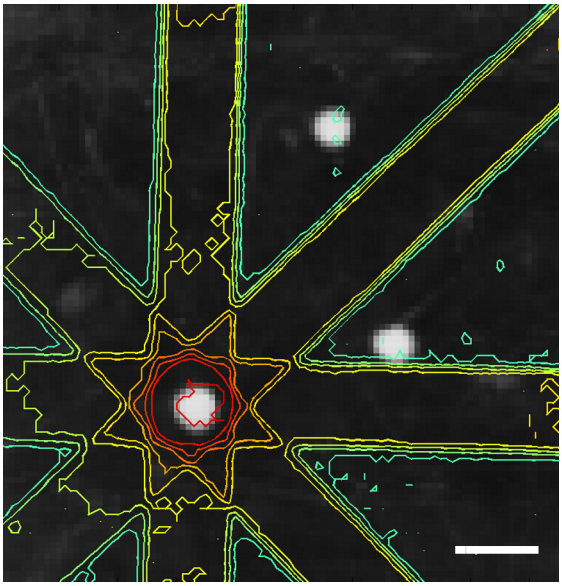

Figure 2.7: Image guided irradiation of off-axis BB with 5×5 mm^2 fields from four directions. Three 2.3 mm diameter BBs are visible. The bottom left BB was targeted for irradiation. Relative dose contours. Scale bar is 5 mm. The four beams with parameters are: (Gantry, X1 mm, X2 mm) (0°,−2.5,−7.5), (45°,−3.0,−8.0), (90°,−0.5,−5.5), (135°,4.0,−1.0).

1D sinusoidal motion, which is not a good representation of a small animal. Tissue deformation and the non-equal time spent in the inspiration and expiration phases are not modeled by the motion phantom. However, the phantom test successfully demonstrates the basic functionality of the gating systems.

Figure 2.9 compares an ungated and gated CT image acquisition on the same rat. Respiratory gating reduced the motion artifacts in the image. By the fact that both the imaging and therapy gating are performed by the same hardware, we argue the gated therapy will reduce the therapy beam blurring, as the gated imaging reduces the image blur. However, it's difficult to quantify the amount of the reduction in motion artifact in the dose deposited into lungs due to the deformation.

2.3.6 Example animal IGRT

Figures 2.10a and 2.10b show the fluoroscopy image guidance used to place the lung fields. An optimal gantry angle was chosen, as shown in figure 2.10a. The jaws are then set as shown

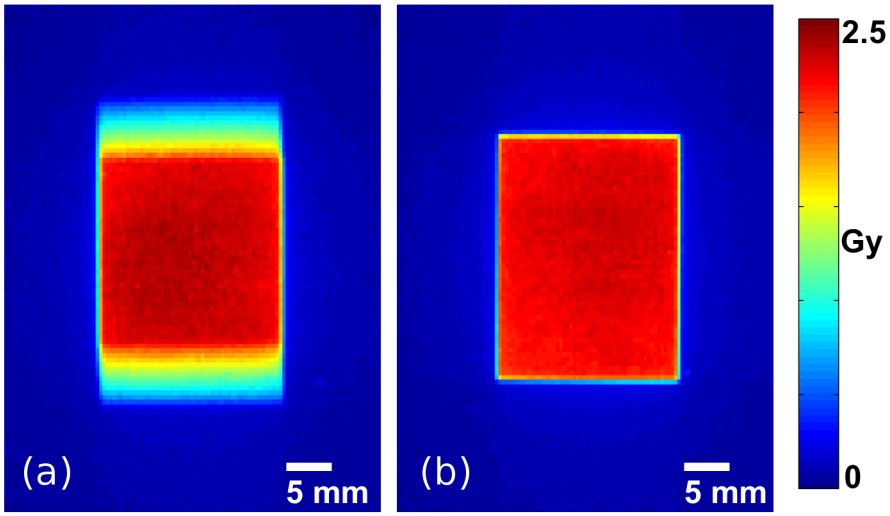

Figure 2.8: Ungated (a) and gated (b) irradiation of an EBT2 film on a motion platform. Peak to peak motion of 5 mm.

in figure 2.10b. The Monte Carlo dose verification is shown in figures 2.10c–2.10e. The bone dose is approximately double the prescribed lung dose, due to the photoelectric absorption of the bone at this low beam energy.

2.4 Discussion

Jaw homing variability is the primary source of jaw error, as it is an order of magnitude larger than the other sources of error. With respect to the ideal targeting accuracy of ±0.1 mm for mice, as proposed by Verhaegen et al.,[1] the performance of the x jaw with a standard deviation of 0.07 mm is comparable. The performance of the y jaw is disappointing, with a standard deviation of 0.3 mm, which exceeds this ideal accuracy. However, at the current level of sophistication in our lab, these error characteristics are acceptable, as we estimate errors in animal positioning and target identification to be on the order of 1–5 mm.

Future revisions of the collimator design would replace the rack and pinion y jaw mechanism with a lead screw. For the current rack and pinion design, some of the error can be detected as missed steps of the motor by the encoder. The software could be modified to use

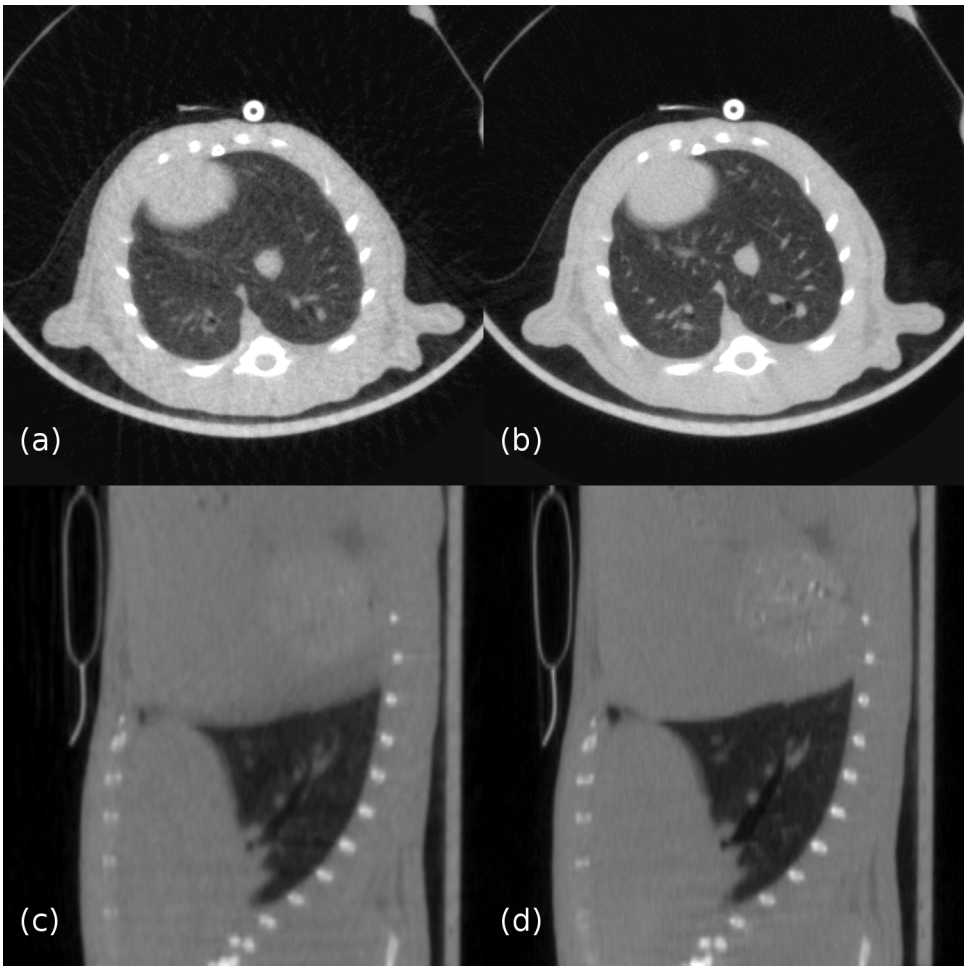

Figure 2.9: Micro-CT images of an anesthetized rat. Transverse ungated (a) and gated (b) slices showing the lungs and heart. Sagittal ungated (c) and gated (d) slices through the left lung. Note the motion blur artifacts on the diaphragm boundary and lung sub-structure are reduced by gated image acquisition. However, cardiac motion blur is still evident, as the acquisition was only respiratory gated. The same hardware systems and techniques used to perform the gated image acquisition are used to deliver a gated therapy.

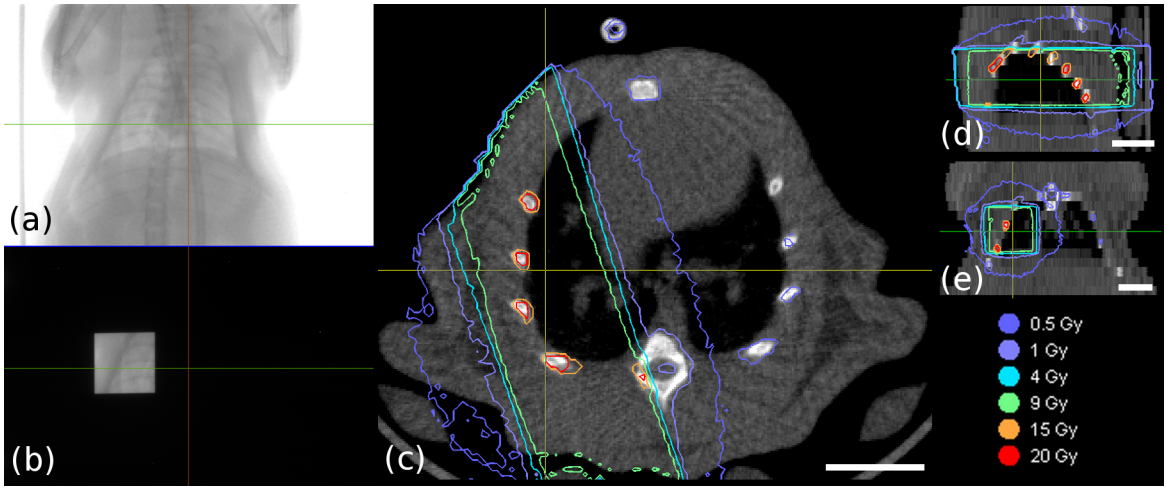

Figure 2.10: Image guidance of AP irradiation field. Fluoroscopy images without (a) and with (b) collimator in treatment position. Field was adjusted with image guidance to shield heart and diaphragm. Monte Carlo dose verification for AP-PA parallel opposed beam plan; transverse (c), sagittal (d) and coronal (e) slices shown. Scale bar is 10 mm.

encoder feedback to improve the y jaw position. Additionally, more reproducible homing detection methods, such as improved mechanical switches or optical detectors would reduce the jaw homing variability. Another approach to improve the jaw homing would be to image the jaw positions with fluoroscopy after start-up and calculate a homing correction to be used for that session. We have not currently implemented these features because the current error characteristics are sufficient for our partial organ irradiations in rats. As we start moving towards more precise irradiation experiments, we should be able to improve the system with software changes.

Generally, the Monte Carlo simulations agree with the film within the measurement uncertainty of 3.6%. The only consistent (3%) discrepancy is for the depth dose of the smallest field, 2×2 mm^2. We are unsure if this consistent discrepancy is a measurement error, or a modeling error, as the film dosimetry is very challenging for such a small field.

One limitation to the system is the dose rate. Nonetheless, the achieved dose rate of 0.3 Gy/min (10 mm depth, at isocenter, 140 kVp) is comparable, but slightly higher than the dose rate reported by the Stanford group of approximately 0.2 Gy/min (surface, at isocenter,

120 kVp).[12] In comparison, the SARRP dose rate is approximately 10 times higher for a similarly sized field.[2] On our system, a typical 10 Gy treatment requires about 60 minutes for treatment delivery, including cooling time for the x-ray tube. While not ideal for high throughput studies, this is tolerable by small animals under isoflurane.

Small fields are practically undesirable on this system, as the dose rate penalty further exacerbates the inherently low dose rate of the micro-CT. Geometric penumbra and focal spot size ultimately affect the smallest field size available. For this system, the collimator is placed far from the source, minimizing the penumbra. Even so, the geometric penumbra with the large focal spot is 0.25 mm in the superior-inferior direction, limiting the smallest field available. Going to the smaller focal spot reduces the geometric penumbra to 0.07 mm at the cost of a further reduction in dose rate. We are also unlikely to use a field this small for our initial experiments, as other sources of uncertainty would prevent the use of this field.

A lesion with diameter smaller than 5 mm would be very difficult to visualize with CT, and would require fusing the CT to another imaging modality, such as MR. This would require development of an immobilization device that would be CT, RT and MR compatible or a robust deformable registration algorithm validated in small animals.

The manual aspect of the vertical couch adjustment and the lack of lateral couch adjustment impede replicating animal setup. This was the major contributor of targeting error in the phantom tests, as we could identify a misalignment with the fluoroscopic imaging, but could not move the phantom precisely. To be able to confidently use the smaller beam sizes will require more development work on animal positioning.

Additionally, the constrained size of the imaging bore restricts activities for commissioning the system and placing animals for therapy with the associated supports for long anaesthetic times.

Given the low 140 kV beam energy, Monte Carlo simulations will be needed to calculate accurate dose, especially to bone, precluding the simple dose calculations.[24,26,27] Therefore, the

lack of flatness and symmetry in the beams is not a problem, as they can be accounted for properly by Monte Carlo simulations.

The low beam energy also presents a potential problem with enhanced bone dose due to the photoelectric effect. At this energy, bone within the field will receive approximately 50% more dose compared to a higher energy beam available on other systems. The effect on the hematopoietic system needs to be considered when planning therapy. If the volume of irradiated red marrow is small relative to total red marrow, the effect will likely be negligible. To quantify the volume of bone irradiated, we provided two examples in figure 2.11 of rat irradiations on our system where we generated and assessed the dose-volume histogram for the bone with a prescription dose of 20 Gy. In either case, we estimated from a micro-CT scan of the rat that less than 3% of total body bone volume was irradiated to 5 Gy. In addition, Lee et al. reported a threshold for leukocytopenia of approximately 27% of red marrow irradiated in a metastatic patient population on helical tomotherapy.[28] While clinically known thresholds are difficult to translate to animal studies, they provide a rough guideline. Since bone marrow toxicities are disease model and site specific, we recommend that treatment planning be done and bone dose-volume histograms be examined as in figure 2.11, in addition to other critical organs.

Simple multi-beam irradiations and image guidance tests qualitatively demonstrated overall performance of the system. Irradiating the elliptical target with a conformal plan is efficient with the system, as collimator size can change automatically as the gantry rotates to the next beam. Systems utilizing cones would require a cone change for each angle to achieve similar conformality, or a raster scanning of a small cone. Asymmetric fields are a strong benefit of this collimation system, enabling the irradiation of off-axis targets. The elliptical cylinder is ideally suited to this jaw configuration. Many complex targets could be decomposed into a series of elliptical cylinders, allowing this system to achieve conformal treatments for complex shapes. However, decomposing into more than a few cylinders could make the delivery time infeasible. Conformality comes at the expense of increased treatment time, like all the other

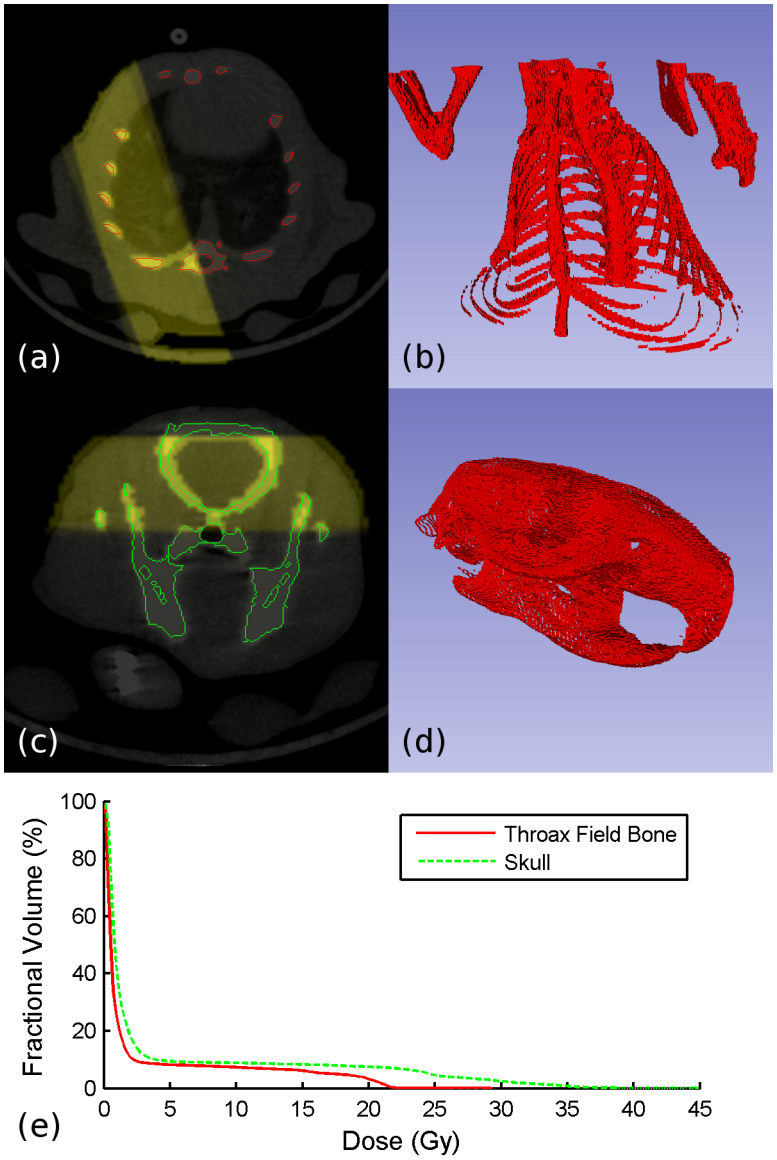

Figure 2.11: An axial slice (a) of a 14 × 14 mm^2 parallel opposed fields irradiating the right lung to a total dose of 20 Gy delivered in 2 fractions. The bones in the scan field of view (the thorax) were segmented (b). Approximately 10% of the bone is receiving a dose above 5 Gy as shown in the dose volume histogram (e). The bone V_{5Gy} is 0.25 cm^3, which is approximately 2% of the total body bone volume of 14 cm^3 including the tail, estimated from a total body micro-CT scan. An axial slice (c) of a 10 × 10 mm^2 lateral parallel opposed fields irradiating a brain tumour to a total dose of 20 Gy delivered in 2 fractions. The skull was segmented (d). Approximately 10% of the skull is receiving a dose above 5 Gy (e). The bone V_{5Gy} is 0.4 cm^3, which is approximately 3% of the total body bone volume.

existing systems. The development of a multi-leaf collimator for small animal IGRT could greatly improve the treatment efficiency of complex targets.

Gating functionality is unique to this system, and these results show promise. More work is required to further characterize the gating performance, specifically in animals. One approach would be to develop a more advanced respiratory phantom that could play back a recorded animal respiratory waveform. To test in animals directly, staining for DNA double-strand breaks immediately after irradiation (γ-H2AX) may be sensitive enough to detect the field edges of irradiation. Histology acquired at later time points, at inflammation or fibrotic stages may not be ideal, as the damaged region could spread beyond the irradiated volume.

Overall, none of the existing small animal IGRT platforms currently have the ideal mix of technology to replicate the sophistication of the clinic. The SARRP and XRAD-225Cx lack computerized collimators, limiting the efficiency of conformal treatment. Intensity modulated plans on these systems may require manual collimator changes during treatment and/or require raster scanning of small cones. However, these purpose built devices offer some advantages, including a high dose rate. The micro-CT based systems have more sophisticated collimators, but suffer from a lower dose rate. The Stanford system has a motorized stage for precise placement and is restricted to mice. The system described in this work employs the standard micro-CT couch with a computerized asymmetric collimation to allow rats as well as mice in a micro-CT geometry. In addition, gated radiation delivery is possible. These strengths fit the niche of the rat oriented imaging studies common at our institution.

2.5 Conclusion

A computerized jaw based collimator has been designed, built and installed in a micro-CT. A Monte Carlo dose package was configured to calculate the dose to small animals and validated against film measurements. Work is still needed to develop a planning system, as currently planning is done manually. The dose rate of the system is low compared to other irradiators,

but has the advantages of being able to perform gated delivery and asymmetric fields, suitable for both rats and mice. This system also offers the advantage that it is based on modifications to an existing commercial design for micro-CT, taking advantage of the gantry, tube, and control infrastructure that is already present, and retaining the existing capability for co-registered 3D micro-CT imaging. We have characterized and commissioned the micro-CT hardware, and the performance is satisfactory to perform the first cohort of image guided, conformal, small animal irradiations studies.

2.6 References

[1]F. Verhaegen, P. Granton, and E. Tryggestad, "Small animal radiotherapy research platforms", Phys. Med. Biol. **56**, R55–R83 (2011).

[2]J. Wong, E. Armour, P. Kazanzides, I. Iordachita, E. Tryggestad, H. Deng, M. Matinfar, C. Kennedy, Z. Liu, T. Chan, O. Gray, F. Verhaegen, T. McNutt, E. Ford, and T. DeWeese, "High-resolution, small animal radiation research platform with x-ray tomographic guidance capabilities", Int. J. Radiat. Oncol., Biol., Phys. **71**, 1591–1599 (2008).

[3]M. Matinfar, E. Ford, I. Iordachita, J. Wong, and P. Kazanzides, "Image-guided small animal radiation research platform: calibration of treatment beam alignment", Phys. Med. Biol. **54**, 891–905 (2009).

[4]R. Clarkson, P. Lindsay, S. Ansell, G. Wilson, S. Jelveh, R. Hill, and D. Jaffray, "Characterization of image quality and image-guidance performance of a preclinical microirradiator", Med. Phys. **38**, 845–856 (2011).

[5]P. V. Granton, M. Podesta, G. Landry, S. Nijsten, G. Bootsma, and F. Verhaegen, "A combined dose calculation and verification method for a small animal precision irradiator based on onboard imaging", Med. Phys. **39**, 4155–4166 (2012).

[6]R. Pidikiti, S. Stojadinovic, M. Speiser, K. Song, F. Hager, D. Saha, and T. Solberg, "Dosimetric characterization of an image-guided stereotactic small animal irradiator", Phys. Med. Biol. **56**, 2585–2599 (2011).

[7]S. Stojadinovic, D. Low, M. Vicic, S. Mutic, J. Deasy, A. Hope, P. Parikh, and P. Grigsby, "Progress toward a microradiation therapy small animal conformal irradiator", Med. Phys. **33**, 3834–3845 (2006).

[8]S. Stojadinovic, D. Low, A. Hope, M. Vicic, J. Deasy, J. Cui, D. Khullar, P. Parikh, K. Malinowski, E. Izaguirre, S. Mutic, and P. Grigsby, "MicroRT – small animal conformal irradiator", Med. Phys. **34**, 4706–4716 (2007).

[9]H. Zhou, M. Rodriguez, F. Van Den Haak, G. Nelson, R. Jogani, J. Xu, X. Zhu, Y. Xian, P. Tran, D. Felsher, P. Keall, and E. Graves, "Development of a micro-computed tomography-based image-guided conformal radiotherapy system for small animals", Int. J. Radiat. Oncol., Biol., Phys. **78**, 297–305 (2010).

[10]E. Graves, H. Zhou, R. Chatterjee, P. Keall, S. Gambhir, C. Contag, and A. Boyer, "Design and evaluation of a variable aperture collimator for conformal radiotherapy of small animals using a microCT scanner", Med. Phys. **34**, 4359–4367 (2007).

[11]M. Bazalova, H. Zhou, P. Keall, and E. Graves, "Kilovoltage beam Monte Carlo dose calculations in submillimeter voxels for small animal radiotherapy", Med. Phys. **36**, 4991–4999 (2009).

[12]M. Rodriguez, H. Zhou, P. Keall, and E. Graves, "Commissioning of a novel microCT/RT system for small animal conformal radiotherapy", Phys. Med. Biol. **54**, 3727–3740 (2009).

[13]J.-R. Dai and Y.-M. Hu, "Intensity-modulation radiotherapy using independent collimators: an algorithm study", Med. Phys. **26**, 2562–2570 (1999).

[14]J. Anderson, R. Symonds-Tayler, and S. Webb, "Investigating the fundamentals of IMRT decomposition using ten simple collimator models", Phys. Med. Biol. **51**, 2225–2236 (2006).

[15]M. Bahri, G. Warnock, A. Plenevaux, P. Choquet, A. Constantinesco, E. Salmon, A. Luxen, and A. Seret, "Performance evaluation of the General Electric eXplore CT 120 micro-CT using the vmCT phantom", Nucl. Instrum. Methods Phys. Res. A **648**, S181–S185 (2011).

[16]L. Du, J. Umoh, H. Nikolov, S. Pollmann, T.-Y. Lee, and D. Holdsworth, "A quality assurance phantom for the performance evaluation of volumetric micro-CT systems", Phys. Med. Biol. **52**, 7087–7108 (2007).

[17]S. Devic, J. Seuntjens, G. Hegyi, E. Podgorsak, C. Soares, A. Kirov, I. Ali, J. Williamson, and A. Elizondo, "Dosimetric properties of improved GafChromic films for seven different digitizers", Med. Phys. **31**, 2392–2401 (2004).

[18]S. Devic, J. Seuntjens, E. Sham, E. Podgorsak, C. Schmidtlein, A. Kirov, and C. Soares, "Precise radiochromic film dosimetry using a flat-bed document scanner", Med. Phys. **32**, 2245–2253 (2005).

[19]T. McCaw, J. Micka, and L. Dewerd, "Characterizing the marker-dye correction for Gafchromic EBT2 film: a comparison of three analysis methods", Med. Phys. **38**, 5771–5777 (2011).

[20]I. Kawrakow, E. Mainegra-Hing, D. Rogers, F. Tessier, and B. Walters, *The EGSnrc code system: Monte Carlo simulation of electron and photon transport*, tech. rep. No. PIRS-701 (National Research Council of Canada, Ottawa, 2011).

[21]I. Kawrakow, "Accurate condensed history monte carlo simulation of electron transport. I. EGSnrc, the new EGS4 version", Med. Phys. **27**, 485–498 (2000).

[22]D. Rogers, B. Faddegon, G. Ding, C.-M. Ma, J. We, and T. Mackie, "BEAM: a Monte Carlo code to simulate radiotherapy treatment units", Med. Phys. **22**, 503–524 (1995).

[23]B. Walters and D. Rogers, *DOSXYZnrc users manual*, tech. rep. No. PIRS-794 rev B (National Research Council of Canada, Ottawa, 2002).

[24]M. Bazalova and E. Graves, "The importance of tissue segmentation for dose calculations for kilovoltage radiation therapy", Med. Phys. **38**, 3039–3049 (2011).

[25]A. Motomura, M. Bazalova, H. Zhou, P. Keall, and E. Graves, "Investigation of the effects of treatment planning variables in small animal radiotherapy dose distributions", Med. Phys. **37**, 590–599 (2010).

[26]J. Chow, M. Leung, P. Lindsay, and D. Jaffray, "Dosimetric variation due to the photon beam energy in the small-animal irradiation: a Monte Carlo study", Med. Phys. **37**, 5322–5329 (2010).

[27]J. Chow, "Depth dose dependence of the mouse bone using kilovoltage photon beams: a Monte Carlo study for small-animal irradiation", Radiat. Phys. Chem. **79**, 567–574 (2010).

[28]I. Lee, J. Seong, C. Lee, Y. Kim, K. Keum, C. Suh, G. Kim, and J. Cho, "Early clinical experience and outcome of helical tomotherapy for multiple metastatic lesions", Int. J. Radiat. Oncol., Biol., Phys. **73**, 1517–1524 (2009).

Chapter 3

Determination of effective atomic numbers and electron densities with dual energy micro-CT measurements

This chapter was adapted from the research article "Determination of effective atomic numbers and electron densities with dual energy micro-CT measurements" by M. D. Jensen, J. Chen and E. Wong.

3.1 Introduction

Preclinical radiobiology studies are required to investigate novel radiation and combination therapies in animal models of cancer. To perform these experiments, a number of hardware platforms to perform image-guided conformal small animal irradiations have been built. These small animal image-guided radiation therapy (IGRT) systems bring the technical sophistication of accurate and precision irradiation from the clinical environment to the preclinical laboratory. However, preclinical radiobiology data collected from studies with large dosimetric uncertainties will be of limited value.

Most small animal IGRT systems operate at x-ray tube potentials at or below 225 kVp to produce a photon beam with dosimetric properties (depth dose, buildup, beam penumbra, etc.) that are appropriate for the size of experimental animals.[1] Supporting small animal treatment planning systems, often incorporating Monte Carlo dose engines, are available to further

advance the sophistication of radiotherapy in small animals.[2,3] However, accurate dose calculations in small animals remain a challenge.[2,4] With kilovoltage beams, small animal IGRT systems deposit energy through both photoelectric and Compton interactions. With clinical megavoltage beams, photoelectric interactions can generally be ignored. To accurately model photoelectric interactions, knowledge of both the tissue elemental composition and the tissue density is needed. The elemental tissue composition is often quantified by the effective atomic number (Z_{eff}) as defined by Johns and Cunningham.[5] Since human tissue compositions have been characterized,[6,7] but not for small animals, we have assumed small animal and human tissue compositions are equivalent in calculating small animal dose.[3,4,8]

Previously, Bazalova and Graves have shown that a larger set of tissues of varying elemental composition is needed for more accurate small animal dose calculation.[4] The most straightforward approach is to create finer density bins with corresponding tissue compositions. This works well for bone since bone density essentially increases with increasing amounts of bone apatite.[8] However, there are many soft tissues with similar density but different compositions. For example, the standard human tissue compositions[9] of Lymph, GI Tract, and Red Marrow have an identical density of 1.03 g/cm^3, but dissimilar elemental compositions as shown by their corresponding effective atomic numbers (Z_{eff}) of 7.6, 7.5, and 7.2. Such an unaccounted 5% difference in Z_{eff} results in a dose variation from 0.87 to 1.01 for the three tissues (lymph, GI tract and red marrow) relative to muscle for a 120 kVp therapy beam (mean energy at 55 keV).[4] This difference is greater than 10% and is unaccounted for when using a single energy CT scan for dose calculation with kV therapy beams.

Dual energy computed tomography (DECT) has the potential to overcome some of the limitations in small animal dose calculation by providing elemental composition information in addition to density. DECT has been proposed to estimate the elemental composition of tissue in the human/clinical setting[10,11] and improve kilovoltage dose calculation accuracy. Specifically, DECT has been studied for low energy brachytherapy[12] and ion therapy.[13]

Currently, little to no work has been published related to the use of dual energy micro-CT (DEmCT) to estimate the elemental composition of tissue to improve dose calculation for small animal radiotherapy studies. Micro-CT differs from clinical CT scanners in several ways. First, the kVp is lower and x-ray spectra softer for a micro-CT compared to a clinical CT, as the sizes of the scan subjects are different. The factory maximum kVp of a common micro-CT (the GE eXplore CT 120, GE Healthcare, Milwaukee, WI) is 110 kVp, with a beam filter of 4.5 mmAl. Clinical DECT scanners most often use 140 kVp as the high energy. One dual source dual energy CT scanner (Somatom Definition Flash, Siemens Healthcare, Forchheim, Germany) has a base filter composed of 3.0 mmAl and 0.9 mmTi applied to the low energy (e.g. 100 kVp) beam, with an additional 0.4 mmSn applied to the high energy (140 kVp) beam.[14,15] One study added 9 mmAl to the filter for the 100 kVp and 140 kVp beams to reduce beam hardening and improve Z_{eff} measurement accuracy.[10] A micro-CT cannot match the spectra of a clinical scanner. Therefore, different spectral pairs will need to be examined for DEmCT. Secondly, micro-CT based on a cone-beam geometry will generally have lower image quality compared to fan beam clinical CT.

This study experimentally investigates dual-energy micro-CT (DEmCT) to be applied to tissue classification for small animal kilovoltage Monte Carlo dose calculation. In this work, an adaptation of an image-space DECT algorithm[10,11] to a small animal cone-beam micro-CT (GE eXplore CT 120) is presented with a new DEmCT energy pair of 70 kVp (4.5 mmAl) and 120 kVp (4.5 mmAl + 1 mmCu). The impact of imaging reconstruction artefacts (systematic uncertainties) and imaging noise (random uncertainties) on the effective atomic number and relative electron density as determined by DEmCT is investigated. We designed phantoms specifically to evaluate the application of DEmCT for tissue classification. These phantoms covered an extensive range of materials, some with similar densities but different effective atomic numbers, and are sized to investigate beam hardening effects. Finally, a proof of concept scan of a mouse is performed and analyzed.

3.2 Methods

3.2.1 Micro-CT scanner and image acquisition

Images were acquired on a modified GE eXplore CT 120 (GE Healthcare, Milwaukee, WI). A computer controlled filter wheel was installed to allow the easy addition, and subsequent removal, of 1 mm of copper to the beam filtration. Two x-ray tube potentials were used, 70 and 120 kVp, with the 120 kVp beam hardened with the addition of 1 mm copper filtration to the base filter of 4.5 mm aluminum. The additional 1 mm of copper to the 120 kVp scan increased the separation between the two scan mean energies. The system modifications, such as the upgraded generator, were described previously.[16] The detector is composed of a CsI scintillator atop a fibre optic taper bonded to a CCD.

Acquisition settings for the scans were 900 projections, full gantry rotation, 16 ms exposure, with 4×4 detector pixel binning and gain and offset settings of 70 and 20, respectively. The 70 kVp scans were run at 32 mA, and the 120 kVp scans at 63 mA to compensate for the additional 1 mmCu filter. The x-ray tube current was chosen as the highest mA setting that would not saturate the detector during a bright field acquisition with no object in the scanner. The large focal spot (1 mm) was used for all scans. Scanning dose was measured with a 0.6 cm^3 Farmer chamber (type 30013, PTW, Freiburg, Germany) in a 2 cm diameter PMMA cylindrical phantom. The doses for the 70 kVp and 120 kVp scans were 8.2 cGy and 9.1 cGy, respectively. Approximately ten minutes of CT scanning time was required for a dual energy acquisition. Images were reconstructed at $0.2 \times 0.2 \times 0.5$ mm^3 using the manufacturer supplied cone-beam filtered back-projection (FDK) algorithm. A median filter (5×5) was applied to the CT axial image slices to obtain an average image noise of 15 and 12 HU for 70 and 120 kVp respectively. All scans included a syringe or vial of water as a reference. Each scan was calibrated individually by delineating air and water regions in the scan and applying an offset and scaling factor. The same scanning protocols were used for all objects. No adaptation of the mAs was made to account for the size of the scanned object.

3.2.2 Dual energy computed tomography algorithm

More detail on the dual energy algorithm is provided in appendix B. This work implements the DECT algorithm described by Bazalova et al.[10,11] with the addition of the modified formulation of the effective atomic number of water, Z_w, described by Landry et al.[12,17] The algorithm uses two CT images acquired at different x-ray tube potentials and models the x-ray spectrum and detector response to generate maps of the effective atomic number (Z_{eff}) and electron density relative to water ($\rho_e/\rho_{e,w}$). Details can be found in Bazalova et al.[11] and Landry et al.[12] To adapt the algorithm to the micro-CT from that of a clinical CT scanner, the micro-CT x-ray spectra and detector response are needed. The x-ray spectra were simulated using BEAMnrc,[18] a package of EGSnrc.[19,20] The Monte Carlo simulation parameters were described previously.[16] The detector response was modelled as a CsI scintillation crystal doped with Tl. Crystal response data from Mengesha et al.[21] was used to adjust the detector signal integration of the x-ray spectrum used by the algorithm. The thickness of the detector scintillator is unknown; a typical thickness of 0.15 mm was used. Theoretical values for effective atomic number ($Z_{eff,theory}$) were calculated using the empirical power law with an exponential power of 3.5.[5]

3.2.3 DECT scanning objects

3.2.3.1 CIRS and Gammex phantom inserts

Tissue-equivalent inserts, with an average diameter of 2.8 cm, from two CT electron density calibration phantoms, Gammex Model 467 (Gammex, Middleton, WI) and CIRS Model 062 (CIRS, Norfolk, VI), were scanned (table 3.1).

3.2.3.2 Micro-CT specific plastics and solution phantoms

We constructed four cylindrical (one 6.08 cm diameter and three 2.54 cm diameter) PMMA phantoms with ten different plastics inserts of varying elemental composition and density (table 3.2). Additionally, four phantoms consisted of vials of solutions with varying concentration

Phantom Insert	Density (g/cm^3)	$\rho_e/\rho_{e,w}$	$Z_{eff,theory}$
Gammex Inserts			
LN-300 Lung	0.300	0.290	7.65
LN-450 Lung	0.450	0.440	7.62
AP6 Adipose	0.940	0.930	6.40
BR-12 Breast	0.980	0.960	7.09
CT Solid Water	1.020	0.990	7.92
BRN-SR2 Brain	1.050	1.040	6.14
LV1 Liver	1.100	1.060	7.92
B200 Bone Mineral	1.150	1.100	10.70
SB3 Cortical Bone	1.820	1.690	13.88
CIRS Inserts			
Lung (Inhale)	0.195	0.190	6.97
Lung (Exhale)	0.495	0.489	7.68
Adipose	0.960	0.952	6.52
Breast (50% Gland, 50% Adipose)	0.991	0.976	7.01
Plastic Water	1.016	1.001	7.79
Muscle	1.062	1.043	7.79
Liver	1.071	1.052	7.78
Trabecular Bone (200 mg/cc HA)	1.161	1.117	10.60
Dense Bone (800 mg/cc HA)	1.609	1.512	13.10

Table 3.1: Clinical electron density phantom inserts. CT density phantom insert material values for physical density and relative electron density are from manufacturer data. Insert material effective atomic number was calculated using manufacturer elemental composition data.

Material	Molecular Formula	Density (g/cm^3)	$\rho_e/\rho_{e,w}$	$Z_{eff,theory}$
Plastics				
Polypropylene (PP)	$(C_3H_6)_n$	0.86	0.88	5.53
High-density polyethylene (HDPE)	$(C_2H_4)_n$	0.95	0.98	5.53
Acrylonitrile butadiene styrene (ABS)	$(C_{15}H_{17}N)_n$	1.00	0.97	5.81
Polystyrene (PS)	$(C_8H_8)_n$	1.05	1.02	5.74
Nylon 6/6	$(C_{12}H_{22}N_2O_2)_n$	1.16	1.13	6.21
Polycarbonate (PC)	$(C_{16}H_{14}O_3)_n$	1.21	1.15	6.33
Poly(ethylene terephtalate) glycol-modified (PETG)	$(C_{16}H_{18}O_4)_n$	1.27	1.22	6.41
Polyvinyl chloride (PVC)	$(C_2H_3Cl)_n$	1.30	1.20	14.26
Polyoxymethylene (POM, acetal, Delrin)	$(CH_2O)_n$	1.42	1.36	7.03
Polytetrafluoroethylene (PTFE, Teflon)	$(C_2F_4)_n$	2.20	1.90	8.48
Poly(methyl methacrylate) (PMMA, acrylic)	$(C_5H_8O_2)_n$	1.18	1.15	6.56
Solutions				
EtOH 100%	C_2H_6O	0.79	0.80	6.47
EtOH 90%	C_2H_6O	0.81	0.82	6.62
EtOH 75%	C_2H_6O	0.84	0.85	6.82
EtOH 50%	C_2H_6O	0.89	0.90	7.09
EtOH 25%	C_2H_6O	0.95	0.95	7.32
EtOH 10%	C_2H_6O	0.98	0.98	7.43
$CaCl_2$ 1 g/100 mL	$CaCl_2$	1.01	1.01	7.88
$CaCl_2$ 5 g/100 mL	$CaCl_2$	1.05	1.04	9.02
$CaCl_2$ 10 g/100 mL	$CaCl_2$	1.10	1.09	10.00
$CaCl_2$ 20 g/100 mL	$CaCl_2$	1.20	1.18	11.31
$CaCl_2$ 30 g/100 mL	$CaCl_2$	1.30	1.26	12.19
$CaCl_2$ 40 g/100 mL	$CaCl_2$	1.40	1.35	12.85
$CaCl_2$ 50 g/100 mL	$CaCl_2$	1.50	1.44	13.37
$CaCl_2$ 60 g/100 mL	$CaCl_2$	1.60	1.53	13.78

Table 3.2: Materials used in custom phantoms. Molecular formula corresponds to the primary component of the plastic. Additives, such as stabilizers or dyes were not considered in the calculation of the relative electron density or effective atomic number. Physical density values are from supplier data sheets, and verified by measurement. Ethanol and calcium chloride solutions were prepared with de-ionized water.

of ethanol or calcium chloride in water to test the accuracies of DECT. In particular, these phantoms were designed to allow us to investigate the impact of imaging artefacts (beam hardening and streaking) as well as imaging noise on the determination of Z_{eff} and $\rho_e/\rho_{e,w}$.

3.2.3.2.1 Plastics phantom design The two sizes of cylindrical phantoms, 2.54 cm (1″) and 6.08 cm (2″) in diameter, were designed to investigate the impact of beam-hardening artefacts on the measurement of Z_{eff} and $\rho_e/\rho_{e,w}$. Beam hardening results in a cupping effect where the HU in the centre of the phantom is depressed compared to the edges, and is more pronounced in larger phantoms. The two sizes of phantoms allows for the comparison of repeated insert materials within the larger phantom and the comparison of materials between the large and small phantoms. Eleven plastics (10 insert materials and PMMA for the phantom body) were used to construct the phantoms, and are listed in table 3.2. Most inserts were of a diameter of 3.175 mm (1/8″), except for POM with a diameter of 4.7625 mm (3/16″) and HDPE and polystyrene with a diameter of 6.35 mm (1/4″). Variations in insert diameter were a result of the supplier's carried inventory. The large diameter PMMA phantom was designed to have an outer ring of 12 inserts and an inner ring of 6 inserts (figures 3.1a, 3.1b). All ten insert plastic materials were inserted into the outer ring, leaving 2 inserts as air. Four materials (PTFE, nylon, polycarbonate and polyprolylene) were repeated in the inner ring with two left as air. Three small phantoms containing the ten unique plastic inserts were constructed (figures 3.1c–3.1h). Two small phantoms contained 4 materials and 2 air inserts and the remaining small phantom contained only two largest diameter inserts (polystyrene and HDPE).

3.2.3.2.2 Solution phantom design To fill in some of the gaps in materials with different compositions of Z_{eff} and $\rho_e/\rho_{e,w}$, we also prepared a total of four solution phantoms (figure 3.2). A Styrofoam vial holder with a capacity of 7 vials was manufactured. Two calcium chloride ($CaCl_2$) based phantoms (figure 3.2a) were prepared with 6 of 8 different concentrations of $CaCl_2$ solutions (table 3.2), plus one vial of water in each phantom. Four concentrations of $CaCl_2$ were repeated (60, 40, 10, and 5 g/100 mL) in these two phantoms. An ethanol (EtOH)

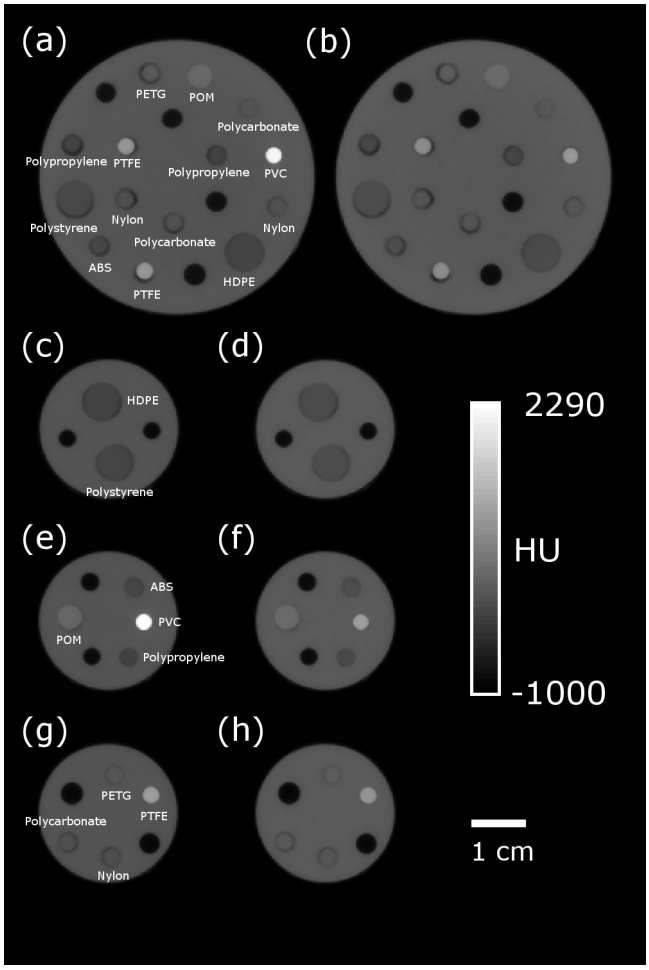

Figure 3.1: Images of the plastics phantoms, with the main body constructed of PMMA. Insert materials are labelled. Corresponding mid-phantom CT slices acquired at 70 kVp (a) and 120 kVp (b) displayed with the same window and level.

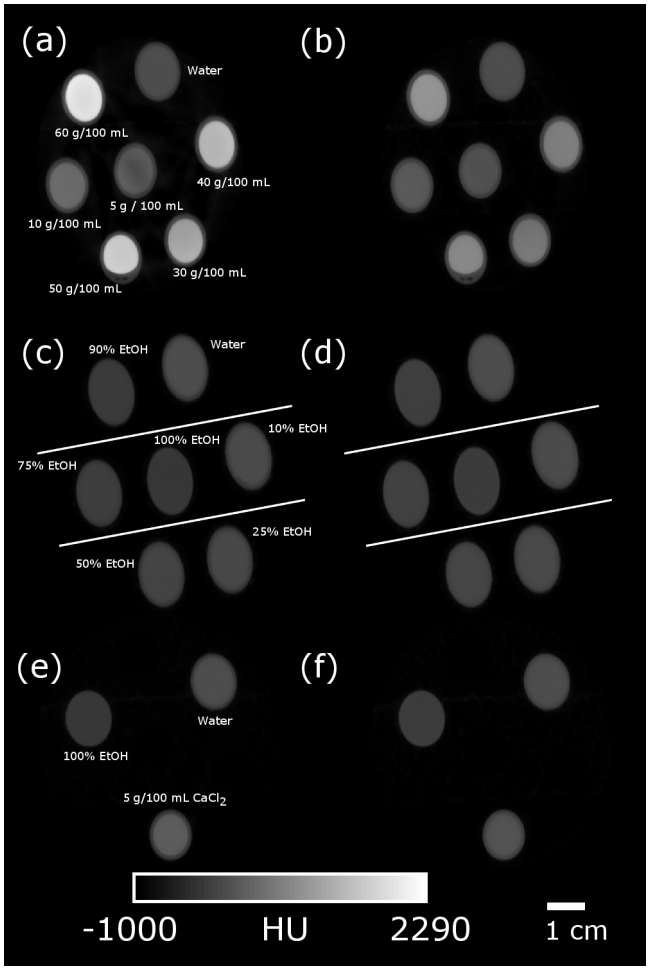

Figure 3.2: Images of the solutions phantoms with insert solutions labelled. For $CaCl_2$ solutions, the g/mL is labelled, and for alcohol (EtOH), the percentage EtOH by volume is labelled. Corresponding mid-phantom CT slices acquired at 70 kVp (a), (c), (e) and 120 kVp (b), (d), (f) are displayed with the same window and level.

based phantom, made of 6 vials of varying ethanol concentrations (table 3.2) plus one vial of distilled water, was prepared (figure 3.2c). Upon imaging the $CaCl_2$ solution phantom, the most concentrated $CaCl_2$ solutions (60 g/100 mL) generated a streaking artefact across the central vial of 5 g/100 mL of $CaCl_2$ (figure 3.2a). Therefore, a fourth solution phantom (figure 3.2e) was constructed composed of one vial of 5 g/100 mL of $CaCl_2$, one vial of water and one vial of 100% of EtOH. This fourth solution phantom was fabricated to eliminate the streaking artefact affecting the 5 g/100 mL $CaCl_2$ measurement, and to help quantify the systematic error from streaking artefacts in the determination of Z_{eff} and $\rho_e/\rho_{e,w}$ from the $CaCl_2$ solution phantoms.

3.2.4 Small animal

A mouse was anesthetized with isoflurane, and imaged at 70 kVp and 120 kVp using the same protocols for the phantoms as described previously. All procedures followed animal care protocols approved by the Animal Use Subcommittee of The University of Western Ontario and were consistent with the policies of the Canadian Council on Animal Care (CCAC). Images were acquired serially, with no adjustment of the subject between scans. To account for intra-scan motion, the 120 kVp image was registered to the 70 kVp image using the General Registration (BRAINS) module in 3D Slicer 4.2.2.[22]

3.2.5 Comparison with theoretical values

For each material in the phantoms, the theoretical Z_{eff} and $\rho_e/\rho_{e,w}$ were calculated and tabulated in tables 3.1 and 3.2. For the CIRS and Gammex inserts, an average HU value for each insert was calculated by taking a region of interest that covered the cross-section of each insert, excluding partial volume voxels at the periphery. The averaged HU pairs for each insert were used as input to the DECT algorithm to calculate a Z_{eff} and $\rho_e/\rho_{e,w}$ for each insert material. For the plastics and solutions phantoms, an image slice was processed with the DECT algorithm to produce Z_{eff} and $\rho_e/\rho_{e,w}$ images. The average values of the measured Z_{eff} and $\rho_e/\rho_{e,w}$ were obtained by placing regions of interest on the images. We grouped our analysis into imaging reconstruction artefacts (systematic uncertainties) and imaging noise (random uncertainties).

3.2.5.1 Impact of imaging artefacts (systematic uncertainties)

Beam-hardening effects were assessed in two ways: comparisons of materials within the large (6.08 cm diameter) phantom and comparisons of materials between the large and the small (2.54 cm diameter) phantoms. For the large phantom, the four inner inserts (PTFE, nylon, polycarbonate and polypropylene) and the phantom body (PMMA) were compared to their

counterparts in the outer ring. All ten insert materials and PMMA were compared between the large phantom (outer and inner rings) and the small phantoms.

3.2.5.2 Impact of imaging noise (random uncertainties)

We isolated variation due to imaging noise from systematic uncertainties due to streaking and beam hardening reconstruction artefacts by analyzing regions of interest in the small plastics phantoms and solution phantoms with concentrations of $CaCl_2$ less than 5 g/100 mL. Twenty-one regions of interests were employed for this investigation, with 11 in the plastics group, and 10 in the solutions group. Imaging noise is characterized by the standard deviation of the HU in the regions of interest. The 70 kVp and 120 kVp images were analyzed before and after a 5×5 median filter was applied to the axial slices of the CT. The Z_{eff} and $\rho_e/\rho_{e,w}$ images are calculated from both the filtered and unfiltered CT HU images. The median, minimum and maximum standard deviations for the CT HU (70 and 120 kVp), Z_{eff} and $\rho_e/\rho_{e,w}$ are reported separately for the plastics group and the solutions group. This will allow us to evaluate the impact of HU random uncertainties from imaging noise on the uncertainties in Z_{eff} and $\rho_e/\rho_{e,w}$.

3.2.6 DECT for small animal

The dual energy algorithm was applied to generate Z_{eff} and $\rho_e/\rho_{e,w}$ images for the mouse. These images were qualitatively examined to provide a first look at limitations and benefits of the dual energy algorithm that cannot easily be demonstrated in phantoms.

3.3 Results

3.3.1 Phantom scans

Dual energy CT images of the large and small plastics phantoms and representative solution phantoms are shown in figures 3.1 and 3.2 respectively. Corresponding Z_{eff} and $\rho_e/\rho_{e,w}$ images

are shown in figures 3.3 and 3.4. Measured Z_{eff} and $\rho_e/\rho_{e,w}$ against their corresponding theoretical values are shown in figure 3.5 for all phantom materials, including CIRS, Gammex, plastics and solutions. For materials above $Z_{eff,theory}$ of 8, there is a trend for the measurement to underestimate the Z_{eff}. Specific data on each group of phantoms are plotted for plastics phantoms (figure 3.6), calcium chloride (figure 3.7) as well as ethanol solutions and the clinical electron density inserts (figure 3.8). In general, the small plastics phantoms agreed better with theoretical values compared to the large phantom. The ethanol solutions agreed better than the calcium chloride solutions because of their effective atomic numbers. Detailed quantification is presented below.

The small plastics phantoms (figure 3.6) generally showed good agreement with theoretical calculations, with 8 of 11 Z_{eff} percent differences less than 3.5%, and a median percent difference of 1.65%. For the large plastics phantom (figure 3.6), the results are generally worse compared to the small phantoms, with a median Z_{eff} percent difference of 5.3% and 6.0% for the inner and outer rings. For the outer ring, 5 of 11 materials have a Z_{eff} percent difference of greater than 10%. The small and large plastics phantoms are made of identical materials. Some outliers, such as PVC and PTFE are common to both phantom sizes and the difference is related to the material (figure 3.6e). Of note, HDPE, PS and ABS have Z_{eff} percent differences of 1.3, 0.7 and 1.2% in the small phantoms, but 10.3, 11.9 and 11.6% in the large phantoms respectively (figure 3.6e). This systematic error in the large phantom is attributed to beam hardening due to difference in phantom size. Relative electron density measurements in the plastics phantoms have median percentage differences of 4.6, 3.6 and 3.0% for the small, large outer and large inner plastics.

The calcium chloride solutions were consistently underestimated in Z_{eff} by the measurement algorithm (figure 3.7e). The largest mean relative electron density percent difference was 3.5% (figure 3.7f). The ethanol solutions show good agreement with theoretical calculations, with all Z_{eff} measurements with a percent error less than 3.5%, and median of 1.9%

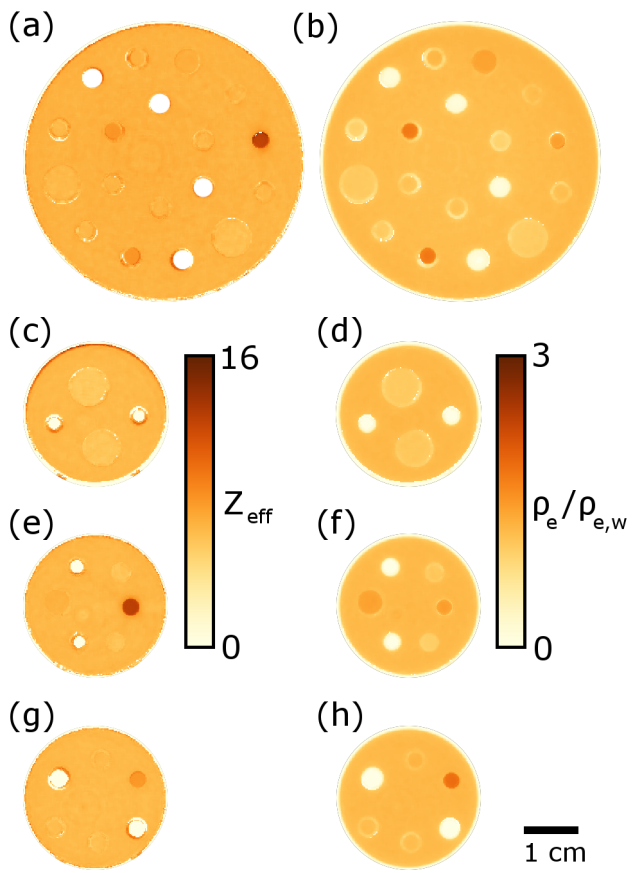

Figure 3.3: Effective atomic number (a), (c), (e), (g) and relative electron density (b), (d), (f), (h) are shown for the same slice of the large and small plastics phantoms. Material labels are shown in figure 3.1.

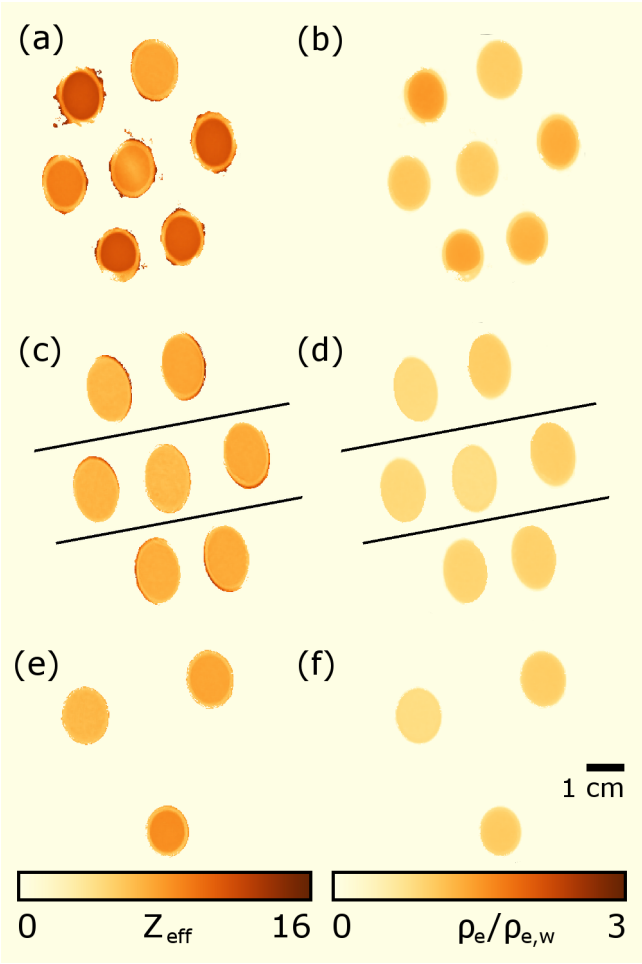

Figure 3.4: Effective atomic number are shown in (a), (c), (e) and relative electron density (b), (d), (f) for the solution phantoms. Insert materials are vials of solutions labelled in figure 3.2.

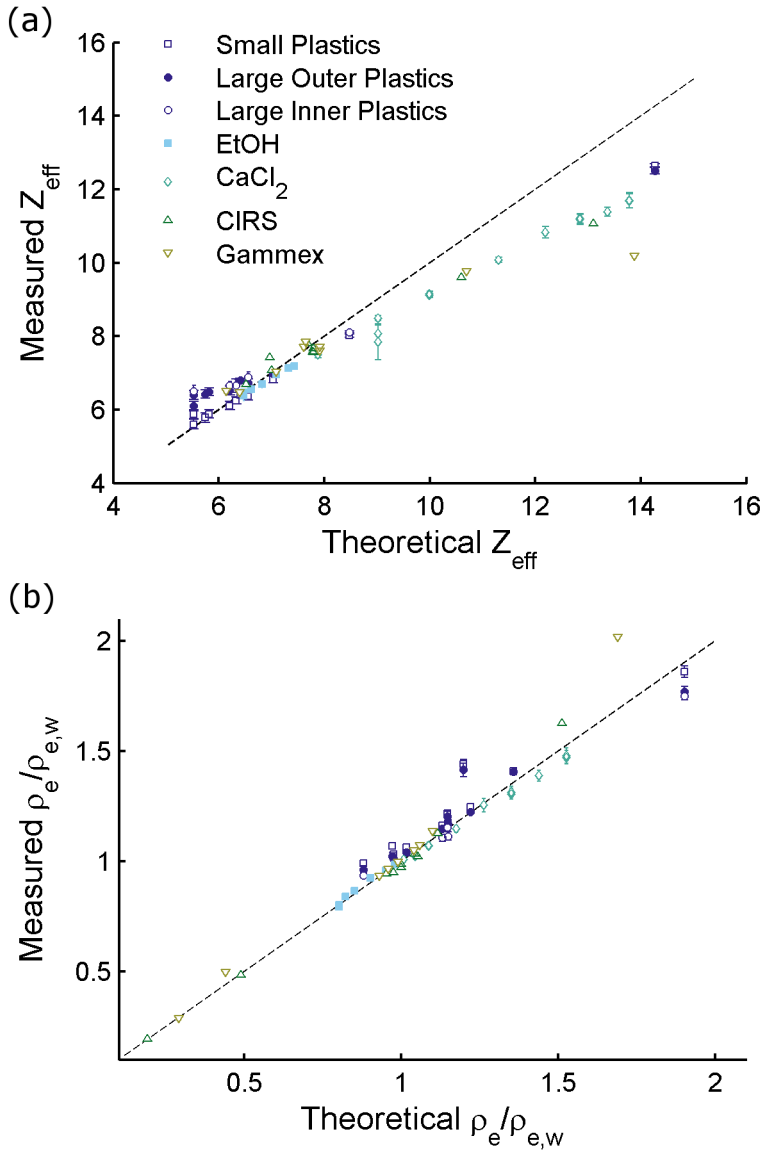

Figure 3.5: Combined phantom results are shown for small and large plastic phantoms, ethanol and calcium chloride solutions, CIRS and Gammex inserts. Error bars are the standard deviation of the voxel values in the ROI. Theoretical versus measurement values of effective atomic number (a) and relative electron density (b) are plotted with a dashed unity line. Note a linear correction is applied to the CCD detector data in chapter 4 that was not applied here.

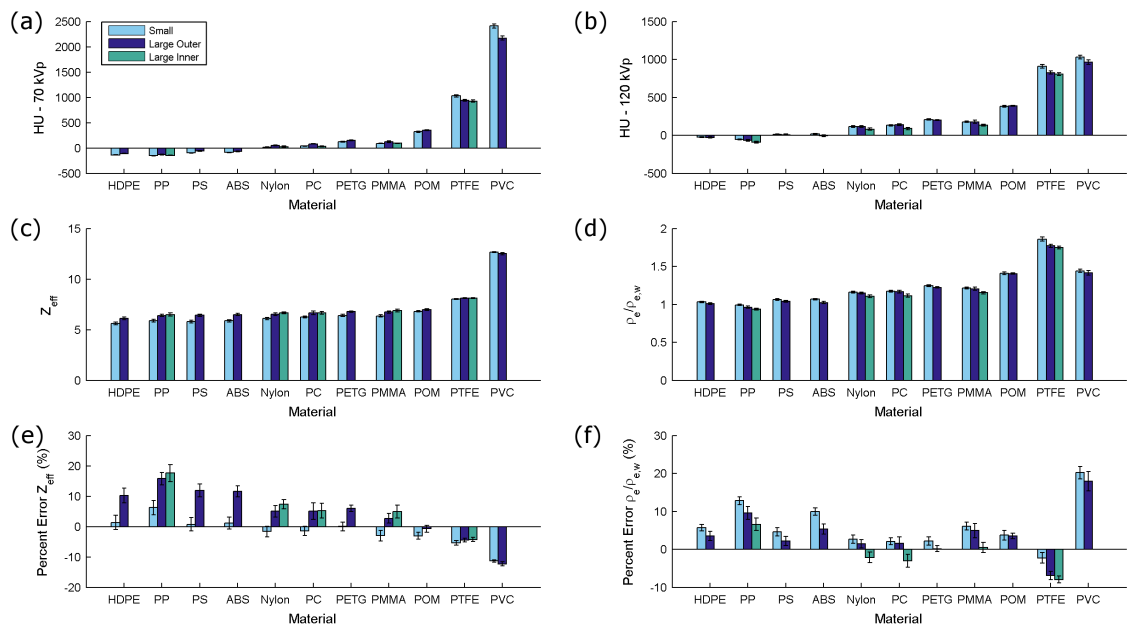

Figure 3.6: Comparison of Hounsfield units scanned at 70 kVp (a) and 120 kVp (b), effective atomic numbers (Z_{eff}) (c), relative electron density ($\rho_e/\rho_{e,w}$) (d), relative errors of Z_{eff} (e) and $\rho_e/\rho_{e,w}$ (f), of material inserts inside the plastic phantoms. Materials are labelled according to names defined in table 3.2. The materials in the larger phantom are labelled to indicate whether the materials are in the outer ("Large Outer") or inner ("Large Inner") rings. They are compared to those inside the smaller phantoms. Error bars indicate the standard deviation of the pixels within the regions of interest.

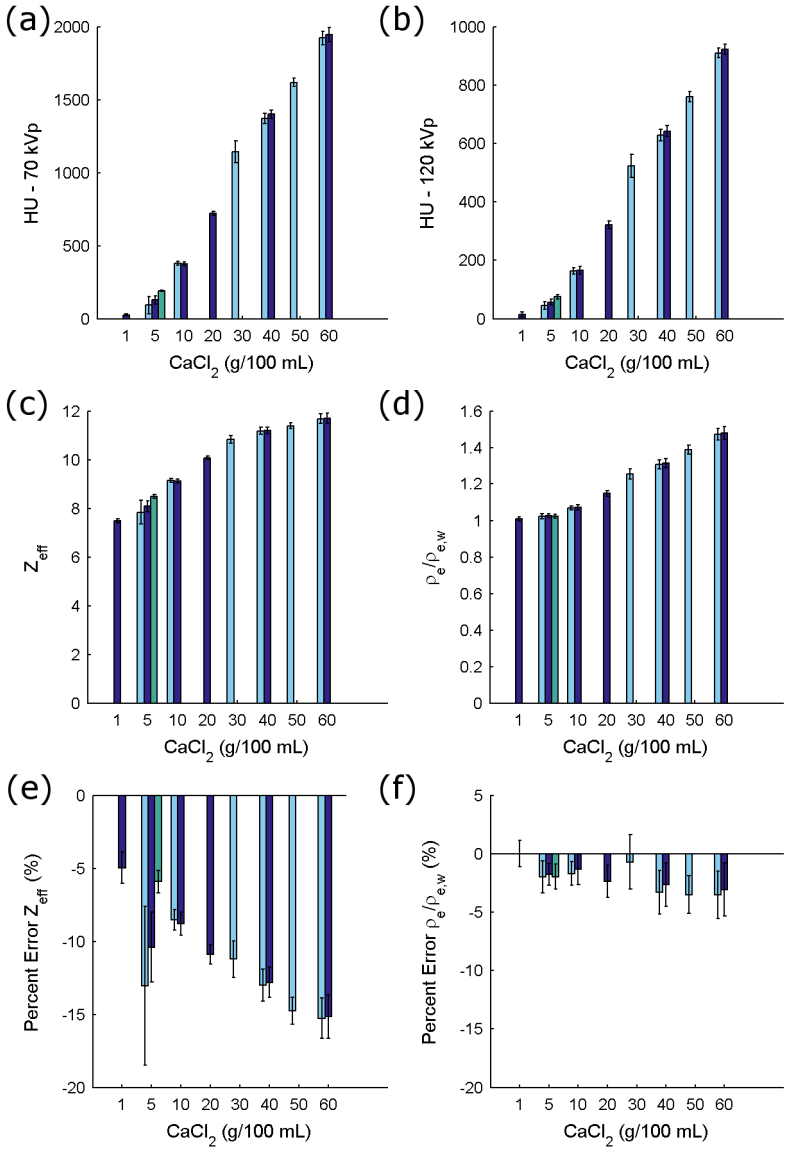

Figure 3.7: Comparison of Hounsfield units scanned at 70 kVp (a) and 120 kVp (b), effective atomic numbers (Z_{eff}) (c), relative electron density ($\rho_e/\rho_{e,w}$) (d), relative errors of Z_{eff} (e) and relative errors of relative electron density $\rho_e/\rho_{e,w}$ (f), of $CaCl_2$ solutions. Indicated in the plots are the amounts of $CaCl_2$ in g/100 mL in the solutions. Multiple bars per concentration indicate a repeated measurement. Error bars indicate the standard deviation of the pixels within the regions of interest.

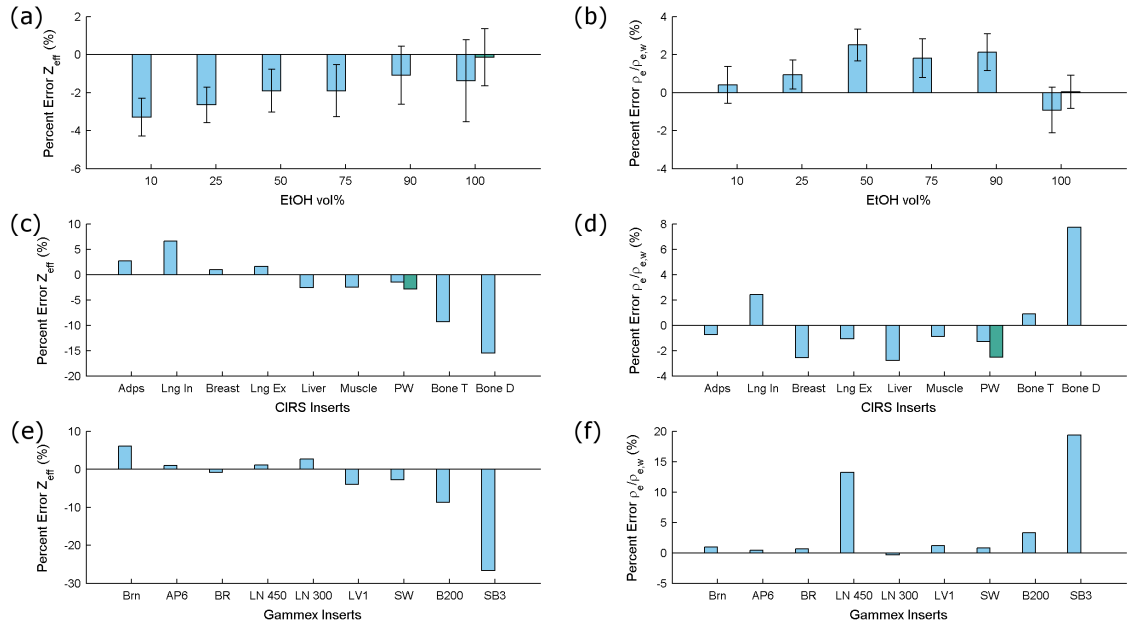

Figure 3.8: Relative differences in effective atomic numbers (Z_{eff}) and relative electron density ($\rho_e/\rho_{e,w}$) for ethanol solutions (a,b), CIRS inserts (c,d) and Gammex inserts (e,f). Multiple bars per material indicate a repeated measurement. Error bars indicate the standard deviation of the pixels within the regions of interest.

(figure 3.8a). Relative electron density was good as well, with all measurements within 2.5% (figure 3.8b).

The clinical electron density inserts (figures 3.8c–3.8f), 13 of the 19 scanned inserts had a percent difference in Z_{eff} less than 5%, with a median of 2.7%. For relative electron density, 16 of the 19 had a percent difference less than 5%, with a median of 1.21%. Bone inserts accounted for 4 of 6 inserts with Z_{eff} differences greater than 5% with the most significant deviation (SB3) discussed below.

3.3.1.1 Imaging arefacts

Two of the largest errors can be attributed to streaking artefacts affecting the 5 g/mL $CaCl_2$ solution when it was placed at the center of the phantom (figure 3.2a). The streaking artefact caused a depression in the estimation of the Z_{eff}, as shown in figure 3.7e. In figure 3.5a, we see that the Gammex SB3 insert did not fall on the same linear trend as the other materials above

		Small Plastics Phantoms	EtOH Phantoms
70 kV HU std dev	CT HU Unfiltered	14.2 (11.7–40.8)	10.8 (9.7–14.3)
	CT HU Median Filtered	6.1 (5.0–39.7)	3.6 (3.2–5.4)
120 kV HU std dev	CT HU Unfiltered	25.7 (21.6–31.1)	17.7 (17.11–22.9)
	CT HU Median Filtered	8.3 (5.8–24.4)	5.8 (4.9–8.4)
Z_{eff} std dev	CT HU Unfiltered	0.365 (0.122–0.430)	0.280 (0.182–0.472)
	CT HU Median Filtered	0.110 (0.049–0.129)	0.078 (0.062–0.140)
$\rho_e/\rho_{e,w}$ std dev	CT HU Unfiltered	0.0348 (0.0308–0.0401)	0.0258 (0.0249–0.0329)
	CT HU Median Filtered	0.0119 (0.0084–0.0260)	0.0082 (0.0070–0.0111)

Table 3.3: Comparisons of uncertainties in effective atomic number (Z_{eff}) and relative electron density ($\rho_e/\rho_{e,w}$) in conjunction with imaging noise (in HU) with and without median noise filtering in the HU images. Reported values are the median (minimum–maximum) standard deviations (std dev) of the respective quantity of interest within regions of interests in the small plastic phantoms and the EtOH solution phantoms.

a Z_{eff} of 8, which we attributed to the phantom size and relatively high attenuating materials, increasing beam-hardening effects.

3.3.1.2 Imaging noise

Table 3.3 summarizes the change in the noise of Z_{eff} and $\rho_e/\rho_{e,w}$ before and after the application of a 5×5 median filter on the CT HU data. Reduction of the CT HU noise leads to a similar reduction of noise in Z_{eff} and $\rho_e/\rho_{e,w}$. Examination of the mean Z_{eff} and $\rho_e/\rho_{e,w}$ before and after the application the median filter yielded a mean absolute difference of 0.2% for both parameters.

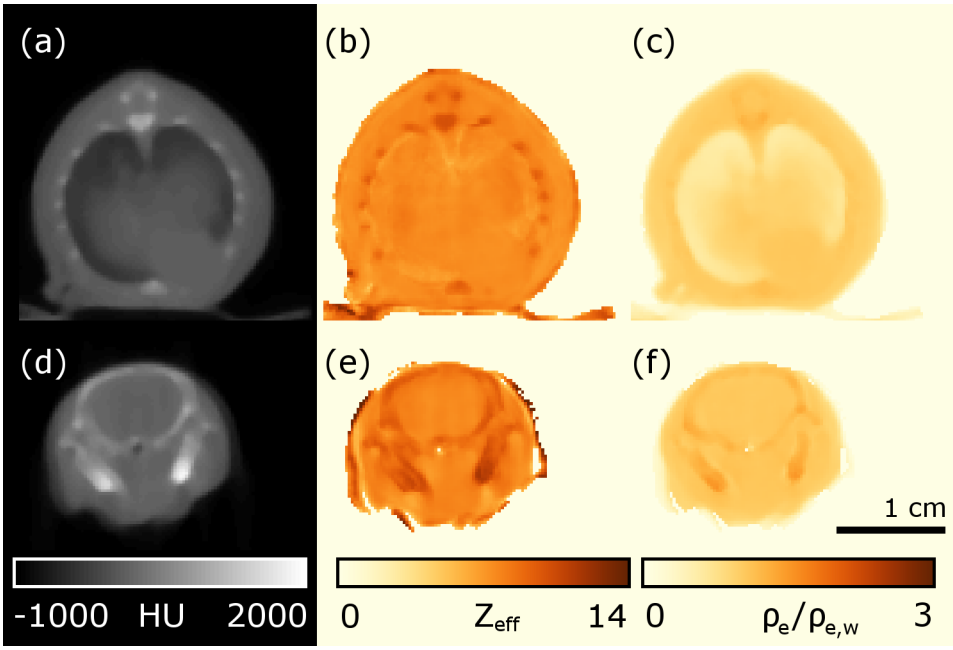

Figure 3.9: Axial CT images acquired at 70 kVp of a mouse at the diaphragm (a) and head (d). Corresponding Z_{eff} (b,e) and relative electron density (c,f) images are also shown.

3.3.2 Small animal scan

The results of the mouse scan are presented in figure 3.9. Looking at the diaphragm axial slice, the breathing motion artefact is apparent in the CT image (figure 3.9a) that causes a gradient in the lung boundary. This artefact is apparent in the relative electron density image (figure 3.9c). However, the Z_{eff} image (figure 3.9b) shows a nearly uniform effective atomic number across the diaphragm interface in contrast to the CT and relative electron density. For the skull images, artefacts from residual motion and beam hardening are apparent, especially in the Z_{eff} image (figures 3.9d–3.9f).

3.4 Discussion

Beam-hardening effects are apparent from the results of the large and small plastics phantoms (figure 3.6). The small plastics phantoms scan results agree better with theoretical values compared to the same materials scanned in the larger plastics phantoms. The spectrum of

this micro-CT is sufficiently soft that additional beam hardening corrections are needed to improve the accuracy when scanning larger specimens. Additional physical filters to harden the x-ray beam would also improve systematic errors due to the x-ray spectrum. Streaking artefacts from high Z_{eff} materials are problematic, as best illustrated by the streak crossing the 5 g $CaCl_2$/100 mL vial in figure 3.2a. The artefact leads to an artefact in the Z_{eff} image (figure 3.4a) and subsequently large error shown in figure 3.7e. For this particular micro-CT scanner, the 1 mm of copper was the most attenuating filter we can employ without substantially increasing beam-on time while keeping reasonable imaging noise.

A median filter was employed to reduce imaging noise to a desirable level while maintaining a scanning protocol with reasonable spatial resolution, imaging radiation dose and scan time. As shown in table 3.3, reducing the noise in the CT images proportionally reduced the noise in Z_{eff} and $\rho_e/\rho_{e,w}$ by roughly the same amount. The application of the median filter did not change the mean value of Z_{eff} and $\rho_e/\rho_{e,w}$ for each material scanned and suggests imaging noise does not strongly affect the accuracy of the values of effective atomic number and relative electron density. However, image noise post-processing is not equivalent to changes in image noise resulting from increased or decreased radiation dose used to acquire the image. To answer the question of how imaging noise (dose) affects DEmCT accuracy for determining Z_{eff} and $\rho_e/\rho_{e,w}$ will require a dedicated study to acquire additional data.

While much work has been done on DECT on clinical scanners, little has been published on dual energy scans in micro-CT. The relative electron density measured in this study by micro-CT has an accuracy slightly worse compared to previous work on clinical scanners.[23] The measured relative electron density of 85% of the materials we scanned agreed within 5% of their theoretical values. The results of Z_{eff} of this study are comparable to previous work on clinical scanners[10,11,17,24–26] if we restrict the comparison to materials with a Z_{eff} less than 8, and exclude measurements suffering from beam hardening effects.

Based on figure 3.5a, it's clearly apparent a calibration correction should be applied for materials with a Z_{eff} larger than 8. However, materials suitable for calibrating are not evident.

The clinical electron density inserts provide a good range of tissue like materials with known composition, but they are too large for a micro-CT. Only a few inserts can be scanned at a time in a time inefficient process. More importantly, the size of the inserts causes systematic beam hardening effects, especially for high Z materials. Figures 3.5a and 3.8e show the SB3 insert does not follow the same trend as the $CaCl_2$ solutions. A calibration based solely on the clinical inserts would not be desirable, for either the traditional single energy CT to density method, or for a correction/verification of a dual-energy CT method. The solutions provided a good range of Z_{eff} values and we can be confident in their composition. However, they are not practical as they need to be reconstituted for each scan as their stability over time is limited by evaporation. The plastics have good stability and are easily assembled into differently sized phantoms to investigate beam hardening. However the range of Z_{eff} is limited in the plastics, with most falling in the low Z_{eff} adipose range and few in the water and bone ranges. Additionally, the composition of the plastics is not well known, relying on manufacturer's specifications. A micro-CT phantom composed of a wide range of well known, stable, tissue mimicking materials, potentially in a few sizes, should be built. A scaled down CIRS Model 062 or Gammex Model 467 would be ideal.

The mouse scan demonstrated several effects that are not seen in a stationary phantom scan. Motion artefacts between the high energy and low energy scans cause artefacts, especially at air-tissue interfaces. Immobilization and registration should be considered to improve DECT performance on animals without fast kV switching or dual source scanners. One benefit is that the DECT algorithm can better classify the tissue Z_{eff} in a region of respiratory motion. A motion induced density gradient in the lung image would often lead to lung and other soft tissues erroneously being assigned to adipose tissues. In our pilot scan, the diaphragm region was uniformly shown with a Z_{eff} in the range of lung/muscle/liver as opposed to adipose, had a density to Z_{eff} method been used. However, the electron density image shows a respiratory motion artefact. We hypothesize that while the apparent density in the diaphragm region is reduced in both low and high energy scans from DECT, the ratio between the two energy scans

remains similar. This preserves the Z_{eff} information. Given the electron density images are sensitive to motion, gated acquisition or reconstruction should be considered for thoracic and abdominal studies.

3.5 Conclusion

We have adapted, implemented and evaluated a dual energy image-space algorithm developed for clinical CT for measuring effective atomic number and electron density in micro-CT. We found the measured and theoretical $\rho_e/\rho_{e,w}$ values agreed with median percent difference less than 2.5%. The measured and theoretical Z_{eff} values agreed with median percent difference less than 3.0% for Z_{eff} less than 8, while measurement systematically underestimated theoretical values for Z_{eff} greater than 8 which can be corrected by a calibration. The small phantoms had better agreement than the large phantom with 8 of 11 versus 2 of 16 material measurements having Z_{eff} percent differences less than 3.5%. Overall, the effective atomic number and relative electron density determinations made with micro-CT are comparable in accuracy to previous DECT work with clinical CT if one restricts the comparison to the small phantoms and materials with Z_{eff} less than 8. None of the phantoms presented in this study were ideal, but together covered a large range of requirements. Ideally, scaled down versions of the clinical electron density phantoms should be constructed that would address multiple calibration phantom requirements in a single phantom. To our knowledge, this is the first application of a dual-energy algorithm in the literature to measure the effective atomic number and relative electron density on a micro-CT scanner. Our study showed beam hardening, imaging noise, and motion artefacts that are more prevalent in micro-CT than clinical CT to be the major challenges of DEmCT. Future investigations into reducing imaging noise, beam hardening and motion artefacts in small animal imaging will enable DECT to be readily applicable with confidence.

3.6 References

[1]F. Verhaegen, P. Granton, and E. Tryggestad, "Small animal radiotherapy research platforms", Phys. Med. Biol. **56**, R55–R83 (2011).

[2]S. J. van Hoof, P. V. Granton, and F. Verhaegen, "Development and validation of a treatment planning system for small animal radiotherapy: SmART-Plan", Radiother. Oncol. **109**, 361–366 (2013).

[3]F. Verhaegen, S. van Hoof, P. V. Granton, and D. Trani, "A review of treatment planning for precision image-guided photon beam pre-clinical animal radiation studies", Z. Med. Phys. **24**, 323–334 (2014).

[4]M. Bazalova and E. Graves, "The importance of tissue segmentation for dose calculations for kilovoltage radiation therapy", Med. Phys. **38**, 3039–3049 (2011).

[5]H. E. Johns and J. R. Cunningham, *The physics of radiology*, 4th ed. (Charles C Thomas, Springfield, IL, 1983), pp. 241–243.

[6]H. Q. Woodard and D. R. White, "Bone models for use in radiotherapy dosimetry", Brit. J. Radiol. **55**, 277–782 (1982).

[7]H. Q. Woodard and D. R. White, "The composition of body tissues", Brit. J. Radiol. **59**, 1209–1219 (1986).

[8]H. Zhou, P. J. Keall, and E. E. Graves, "A bone composition model for Monte Carlo x-ray transport simulations", Med. Phys. **36**, 1008–1018 (2009).

[9]ICRU, *Photon, electron, proton and neutron interaction data for body tissues*, tech. rep. (International Commission on Radiation Units & Measurements, Bethesda, MD, 1992).

[10]M. Bazalova, J.-F. Carrier, L. Beaulieu, and F. Verhaegen, "Tissue segmentation in Monte Carlo treatment planning: a simulation study using dual-energy CT images", Radiother. Oncol. **86**, 93–98 (2008).

[11]M. Bazalova, J.-F. Carrier, L. Beaulieu, and F. Verhaegen, "Dual-energy CT-based material extraction for tissue segmentation in Monte Carlo dose calculations", Phys. Med. Biol. **53**, 2439–2456 (2008).

[12]G. Landry, P. V. Granton, B. Reniers, M. C. Ollers, L. Beaulieu, J. E. Wildberger, and F. Verhaegen, "Simulation study on potential accuracy gains from dual energy CT tissue segmentation for low-energy brachytherapy Monte Carlo dose calculations", Phys. Med. Biol. **56**, 6257–6278 (2011).

[13]G. Landry, K. Parodi, J. E. Wildberger, and F. Verhaegen, "Deriving concentrations of oxygen and carbon in human tissues using single- and dual-energy CT for ion therapy applications", Phys. Med. Biol. **58**, 5029–48 (2013).

[14]A. N. Primak, J. C. Ramirez Giraldo, X. Liu, L. Yu, and C. H. McCollough, "Improved dual-energy material discrimination for dual-source CT by means of additional spectral filtration", Med. Phys. **36**, 1359–1369 (2009).

[15]M. Saito, "Optimized low-kv spectrum of dual-energy ct equipped with high-kv tin filtration for electron density measurements", Med. Phys. **38**, 2850–2858 (2011).

[16]M. D. Jensen, W. T. Hrinivich, J. A. Jung, D. W. Holdsworth, M. Drangova, J. Chen, and E. Wong, "Implementation and commissioning of an integrated micro-CT/RT system with computerized independent jaw collimation", Med. Phys. **40**, 081706 (2013).

[17]G. Landry, B. Reniers, P. V. Granton, B. van Rooijen, L. Beaulieu, J. E. Wildberger, and F. Verhaegen, "Extracting atomic numbers and electron densities from a dual source dual energy CT scanner: experiments and a simulation model", Radiother. Oncol. **100**, 375–379 (2011).

[18]D. Rogers, B. Faddegon, G. Ding, C.-M. Ma, J. We, and T. Mackie, "BEAM: a Monte Carlo code to simulate radiotherapy treatment units", Med. Phys. **22**, 503–524 (1995).

[19]I. Kawrakow, "Accurate condensed history monte carlo simulation of electron transport. I. EGSnrc, the new EGS4 version", Med. Phys. **27**, 485–498 (2000).

[20]I. Kawrakow, E. Mainegra-Hing, D. Rogers, F. Tessier, and B. Walters, *The EGSnrc code system: Monte Carlo simulation of electron and photon transport*, tech. rep. No. PIRS-701 (National Research Council of Canada, Ottawa, 2011).

[21]W. Mengesha, T. D. Taulbee, B. Rooney, and J. D. Valentine, "Light yield nonproportionality of CsI(Tl), CsI(Na), and YAP", IEEE T. Nucl. Sci. **45**, 456–461 (1998).

[22]A. Fedorov, R. Beichel, J. Kalpathy-Cramer, J. Finet, J.-C. Fillion-Robin, S. Pujol, C. Bauer, D. Jennings, F. Fennessy, M. Sonka, J. Buatti, S. Aylward, J. V. Miller, S. Pieper, and R. Kikinis, "3D Slicer as an image computing platform for the Quantitative Imaging Network", Magn. Reson. Imaging **30**, 1323–1341 (2012).

[23]M. Saito, "Potential of dual-energy subtraction for converting CT numbers to electron density based on a single linear relationship", Med. Phys. **39**, 2021–2030 (2012).

[24]M. M. Goodsitt, E. G. Christodoulou, and S. C. Larson, "Accuracies of the synthesized monochromatic CT numbers and effective atomic numbers obtained with a rapid kVp switching dual energy CT scanner", Med. Phys. **38**, 2222–2232 (2011).

[25]J. K. Van Abbema, A. Van der Schaaf, W. Kristanto, J. M. Groen, and M. J. W. Greuter, "Feasibility and accuracy of tissue characterization with dual source computed tomography", Phys. Medica **28**, 25–32 (2012).

[26]N. Hünemohr, B. Krauss, C. Tremmel, B. Ackermann, O. Jäkel, and S. Greilich, "Experimental verification of ion stopping power prediction from dual energy CT data in tissue surrogates", Phys. Med. Biol. **59**, 83–96 (2014).

Chapter 4

Improved determination of effective atomic numbers and electron densities using dual energy micro-CT with optimized spectra and CMOS panel detector

This chapter was adapted from the research article "Improved determination of effective atomic numbers and electron densities using dual energy micro-CT with optimized spectra and CMOS panel detector by M. D. Jensen, S. Dawson, J. Chen and E. Wong.

4.1 Introduction

Small animal radiation therapy is a growing field which investigates cancer in a preclinical setting with sophisticated techniques such as image guidance, intensity modulation, and treatment planning that are available in the clinic.[1,2] Accurate radiation dosimetry is necessary in preclinical small animal radiotherapy studies. Small animal radiation dosimetry is challenged by kilovoltage x-ray therapy beams and micro-CT imaging limitations.

Kilovoltage x-rays (< 225 kVp) are generally used for small animal radiotherapy, in contrast to the megavoltage beams used for human external beam therapy. Kilovoltage x-rays deposit dose through photoelectric and Compton interactions requiring knowledge of both ele-

mental composition and electron density to accurately compute the dose.[3] Dual energy CT can provide elemental composition information that is needed to model photoelectric interactions accurately in small animals. So far, limited work has been done on dual energy micro-CT for dose computation.

In general, micro-CT scanners have a lower maximum x-ray accelerating potential than clinical scanners. Micro-CT often has softer spectra, as they are not as strongly filtered. For example, the GE eXplore CT 120 (GE Healthcare, Milwaukee, WI) has a maximum kVp of 110 kV and 4.5 mmAl filter, while most clinical scanners are capable of 140 kVp and have stronger base filters (3.0 mmAl + 0.9 mmTi).[4,5] Furthermore, investigations at improving clinical DECT have increased the beam filtering, further separating the x-ray spectra from that used in micro-CT.[4–8] Therefore beam hardening related cupping and streaking artefacts are often present in micro-CT images and it becomes a challenge to implement DECT methods that have been demonstrated with clinical CT scanners with better image quality.

The majority of DECT methods were developed and evaluated on clinical CT scanners, and can be classified into projection-space or image-space approaches. In this paper, we investigate DECT approaches for measuring electron density and elemental composition in small animals using a micro-CT scanner equipped with a factory-installed CCD and a newer CMOS x-ray detector.

To reduce beam hardening artefacts, projection-space DECT methods have been used to decompose the projection measured attenuation into thicknesses of two basis materials. Alvarez and Macovski first showed decomposition into theoretically pure photoelectric and Compton materials,[9] while Lehmann et al. showed any two materials could be used as a basis.[10] Virtual monoenergetic images created from the basis material images can be used to improve contrast for diagnostic tasks.[11,12] Taschereau et al. implemented a projection space DECT algorithm on a micro-CT using x-ray spectral information and a Newton-Raphson solver.[13]

Alternatively, image-space DECT methods can be used where the projections from the two energies are first reconstructed separately into two image volumes. The resultant image

volumes are then processed with a dual energy algorithm. Image-space DECT can be easier to implement, especially if there is no access to the projection data. One spectral method solves for the effective atomic number (EAN) and relative electron density (RED) by using x-ray spectra information and the pair of CT image values.[6,7,14–16] Torikoshi et al. published this method using synchrotron monoenergetic CT images.[14] Subsequently, Bazalova et al. extended the algorithm to clinical CT scanner acquired polyenergetic CT images and the algorithm was further improved by Landry et al.[6,7,15,16] Other methods have been published by Heismann et al., Goodsitt et al., Van Abbema et al., Landry et al., Hünemohr et al., and Bourque et al.[17–23] Generally, they determine a number of model parameters from a calibration exercise, with some having a theoretically based model, such as the Rutherford parameterization,[24] and others with empirical models. Tremblay et al. compared projection based sinogram methods with the image space method by Bourque et al. with virtual mono-energetic images.[25] This paper compares two image-space methods, the spectral method by Bazalova et al. and the the empirical method outlined by Bourque et al., which respectively will be referred to as the spectral DECT method and the polynomial fit DECT method.

In this study, we investigated micro-DECT by changing from a CCD x-ray detector to a more sensitive CMOS panel detector and optimized the x-ray beam quality to reduce beam hardening related artefacts. The more sensitive CMOS allowed heavy filtration of the beam with sufficient signal for an image. First we optimized the x-ray beam parameters and filtration to create a pair of narrow x-ray spectra with maximal separation for DECT acquisition. We then compared the performance of the CMOS detector with improved x-ray beam quality to the performance of the previous CCD detector and x-ray beam quality for effective atomic number and relative electron density measurements. Both the spectral and the polynomial fit DECT methods are applied to the CCD and CMOS detector data. Secondly, we investigated using virtual monoenergetic images with the spectral and polynomial fit DECT methods to further reduce beam-hardening effects and quantitatively assess the improvement of effective atomic number and relative electron density measurements. The CMOS detector data were processed

to create virtual monoenergetic images and polyenergetic images for DECT calculation using both the spectral and polynomial fit DECT methods.

4.2 Methods

4.2.1 Micro-CT Hardware

Our lab has previously published on a GE eXplore CT 120 (GE Healthcare, Milwaukee, WI) micro-CT that has been modified for small animal image guided radiation therapy.[26] The factory standard detector is a CCD bonded to fibre optic taper with a CsI scintillator. A new CMOS flat panel detector (Xineos 1313, TeledyneDALSA, Waterloo, Canada) was installed, replacing the CCD detector and allowing us to compare scans from the two detectors. This flat panel detector has a pixel pitch of 100 microns, is more sensitive (including a thicker CsI scintillator) and has a faster readout: up to 45 fps with a CameraLink Interface. The scanner with the new flat panel has an effective resolution at isocentre of 68 microns, reduced when compared to the CCD detector with 30 microns at isocentre. The CMOS detector has a larger axial field of view as the panel active area is square (131 mm $\times$ 131 mm), compared the CCD that had an aspect ratio of approximately 23:35.

4.2.2 Spectrum Optimization (kVp, mAs and filter choice)

Materials that are widely available were considered for filters, and the possible x-ray tube potentials were capped at 100 kVp as recommended by the CMOS manufacturer. The spectra were initially simulated with Spektr[27] for optimizing the choice of filter material and thickness. Many simulations of spectra with various kVp, filter materials and thicknesses were considered to minimize the overlap of two imaging spectra. Refinement of the optimization was performed on the micro-CT by testing the leading candidate materials. Once the filters and corresponding thicknesses had been chosen, the final spectra used for DECT processing were calculated with

	kVp	Beam Filter	Mean Energy (keV)	mAs, focal spot	Rotation mode	Views × frame avg	Scan time (min)	Dose (rel. to 70 kVp)
CCD Low Energy	70	4.5 mmAl	42.2	32 mA 16 ms Large	Continuous	900 × 1	5	1
CCD High Energy	120	4.5 mmAl + 1.0 mmCu	75.8	63 mA 16 ms Large	Continuous	900 × 1	5	1.2
CMOS Low Energy	60	4.5 mmAl + 0.4 mmCu	45.8	63 mA 16 ms Large	Step and Shoot	450 × 18	30	1.4
CMOS High Energy	100	4.5 mmAl + 0.8 mmSn	77.4	50 mA 20 ms Large	Step and Shoot	450 × 18	30	1.1

Table 4.1: Scanning protocol characteristics.

BEAMnrc.[28] The final filters chosen for both the low and high-energy beams are listed in table 4.1.

4.2.3 Scanning protocols

The scanning protocols are summarized in table 4.1. For both detectors, the mAs was chosen to maximize the detector signal intensity without saturation on a bright-field image with no scanned object. Where possible, mA was increased first to maintain a short exposure time. The mAs was kept constant for all scans of the same protocol and not varied to compensate for scan object size. For the new CMOS detector, a step and shoot acquisition protocol with frame averaging was chosen as the high sensitivity causes the detector to saturate at much lower doses compared to the CCD. By taking multiple images at each projection angle and averaging, we can better match the noise characteristics of the scanning protocols of the CCD detector acquisition. The step and shoot acquisition also provides more consistent co-registration between the low and high energy projections than the continuous rotation acquisition used with the CCD detector.

4.2.4 Image reconstruction and preprocessing

All volumes acquired with the CMOS detector were reconstructed using the FDK cone-beam filtered back-projection implementation in RTK[29] with default parameters at a resolution of $136.8 \times 136.8 \times 342.1$ μm^3. The volumes acquired with the CCD detector were reconstructed with the manufacturer supplied FDK engine with a resolution of $198.7 \times 198.7 \times 496.8$ μm^3. Each volume was individually calibrated in HU by segmenting reference water and air regions and applying appropriate scaling and shift factors. All images were filtered with a median filter (5×5) in the axial plane before subsequent DECT processing. After median filtering the images had an average image noise of 13, 17, 12 and 13 HU for the 60, 100, 70 and 120 kVp protocols, respectively.

4.2.4.1 Virtual monoenergetic image reconstruction

The projection class of dual energy methods can create effective/virtual monoenergetic images.[9,10] Instead of using the spectrum and a non-linear solver to decompose the projections into equivalent thicknesses of two basis materials as previously demonstrated for micro-CT,[13] we used a calibration based method. We implemented a fast isotransmission lines and table lookup method with the reduced calibration measurement method.[30,31] Calibration was performed with aluminum and solid water as the two basis materials. Twenty steps of aluminum of 1 mm thickness and 25 steps of solid water of 2 mm thickness were scanned. Polyenergetic projections were first processed and decomposed into aluminum and solid water thickness projections. RTK's FDK implementation was then used to reconstruct aluminum and solid water density volumes at the same resolution as the polyenergetic images. Effective virtual monoenergetic images were then created at the mean energies of the polyenergetic spectra: 46 keV and 77 keV. These virtual monoenergetic images are then treated the same as the polyenergetic images with individual HU calibration and median filtering as described previously.

	Density (g/cm^3)	$\rho_e/\rho_{e,w}$	$Z_{med} \pm \Delta Z_{med}$
Plastics			
Polypropylene (PP)	0.86	0.88	5.43 ± 0.04
High-density polyethylene (HDPE)	0.95	0.98	5.43 ± 0.04
Acrylonitrile butadiene styrene (ABS)	1.00	0.97	5.76 ± 0.02
Polystyrene (PS)	1.05	1.02	5.69 ± 0.02
Nylon 6/6	1.16	1.13	6.14 ± 0.03
Poly(methyl methacrylate) (PMMA, acrylic)	1.18	1.15	6.50 ± 0.02
Polycarbonate (PC)	1.21	1.15	6.29 ± 0.02
Poly(ethylene terephtalate) glycol-modified (PETG)	1.27	1.22	6.36 ± 0.02
Polyvinyl chloride (PVC)	1.30	1.2	14.064 ± 0.001
Polyoxymethylene (POM, acetal, Delrin)	1.42	1.36	6.99 ± 0.02
Polytetrafluoroethylene (PTFE, Teflon)	2.20	1.9	8.467 ± 0.001
Gammex			
LN-300 Lung	0.310	0.298	7.50 ± 0.03
LN-450 Lung	0.480	0.468	7.50 ± 0.03
AP6 Adipose	0.948	0.931	6.17 ± 0.03
BR-12 Breast	0.979	0.956	6.88 ± 0.03
CT Solid Water	1.016	0.987	7.66 ± 0.02
BRN-SR2 Brain	1.051	1.047	6.05 ± 0.03
LV1 Liver	1.09	1.059	7.66 ± 0.02
Inner Bone*	1.136	1.089	10.28 ± 0.02
B200 Bone Mineral	1.149	1.101	10.29 ± 0.02
CB2-30*	1.334	1.279	10.75 ± 0.01
CB2-50*	1.561	1.471	12.39 ± 0.01
SB3 Cortical Bone	1.823	1.695	13.50 ± 0.02

Table 4.2: Material Properties. Gammex inserts marked with * were not scanned with the CCD version of the micro-CT.

4.2.5 Test materials

Two sets of materials were used to evaluate the DECT performance. The first set consisted of the material inserts from the Gammex Model 467 (Gammex, Middleton, WI) electron density phantom. Twelve material inserts were scanned with the CMOS panel, and 9 of the 12 were previously scanned with the CCD. The second material set was four custom plastics phantoms: 3 small phantoms with a diameter of 2.54 cm (1″) and one large phantom with a diameter of 6.08 cm (2″). The plastics phantoms consisted of a body of PMMA with 10 other plastic inserts. The two sizes of phantoms allow for comparisons to investigate the effects of beam hardening. All four plastics phantoms were scanned previously on the micro-CT with the CCD detector and then rescanned with the CMOS panel. All the test materials are listed in table 4.2.

4.2.6 Algorithms

More details on the dual energy algorithms are provided in appendix B.

4.2.6.1 Definition of effective atomic number

The gold standard effective atomic number used in this work is Z_{med} described by Bourque et al.[22] This method defines a lookup curve relating the electron cross-section to the atomic number based on the X-COM database.[32] The electron cross-section of a mixed material is computed and the Z_{med} of the material is found using the lookup curve. The effective atomic number Z_{med} was computed using the four x-ray spectra used for imaging (table 4.1) and the therapy spectrum (140 kVp). The consensus Z_{med} value was computed by averaging the largest and smallest value and the non-statistical variation (ΔZ_{med}) was computed as half the difference between the largest and smallest value. $Z_{med} \pm \Delta Z_{med}$ of our test materials are listed in table 4.2.

4.2.6.2 Spectral based DECT method

The image space spectrum method was implemented.[6,7,14–16] A linear correction was applied to the spectral method to reduce the error between measured EAN and theoretical Z_{med} values. This linear correction was not applied in chapter 3. For the virtual monoenergetic images, the same spectrum image space method is used, except with a single energy input for the spectrum. Using virtual monoenergetic images emulates the original implementation of Torikoshi et al. with a synchrotron-based scanner.[14]

4.2.6.3 Empirical polynomial fit DECT method

We implemented the method published by Bourque et al.[22] Briefly, the dual energy ratio (DER: ratio of the attenuation coefficients for the high energy to low energy scans) is computed for each voxel of the image pair and regions of interest are applied to generate a mean DER for each calibration material. A polynomial is fit to relate the theoretical effective atomic number Z_{med} to the DER for all materials. Then another two polynomials, one for each energy scan,

are fit to relate the theoretical relative electron density to the HU and Z_{med}. Both the high and low energy scans are used to compute two relative electron density maps which are equally weighted to create a final relative electron density map. This method can be optimized by choosing the order of the polynomial. The order of the polynomial was chosen by trying orders of 2, 4 and 6. Higher orders were rejected if they caused strong inflection points in the range of the data or if the root mean squared error of the fit did not change markedly from the lower order polynomial fit.

4.2.7 Analysis

For all volumetric scans, representative slices were selected from the volumes and regions of interest were drawn on the various materials in the scan. The regions of interest were applied as masks to the input CT images and the generated EAN and RED images to compute a mean and standard deviation of each parameter for each material in each location.

4.2.7.1 Comparison of CMOS panel detector and optimized spectra with CCD detector

To compare the imaging performance between the CCD and CMOS detectors, polyenergetic images from both detectors were compared with both the spectral DECT method and the polynomial fit method. We specifically examined the plastics that were scanned in three positions: large phantom inner ring, large phantom outer ring, and small phantom to compare and evaluate beam-hardening effects. To evaluate how well the measurements agreed with the theoretical Z_{med} values, the root mean squared error and the absolute mean and maximum residuals of the linear correction of the spectral DECT method and the polynomial fit DECT method were examined. Residuals from the polynomial fit or spectral DECT correction are an indication of the inconsistencies introduced by beam hardening artefacts.

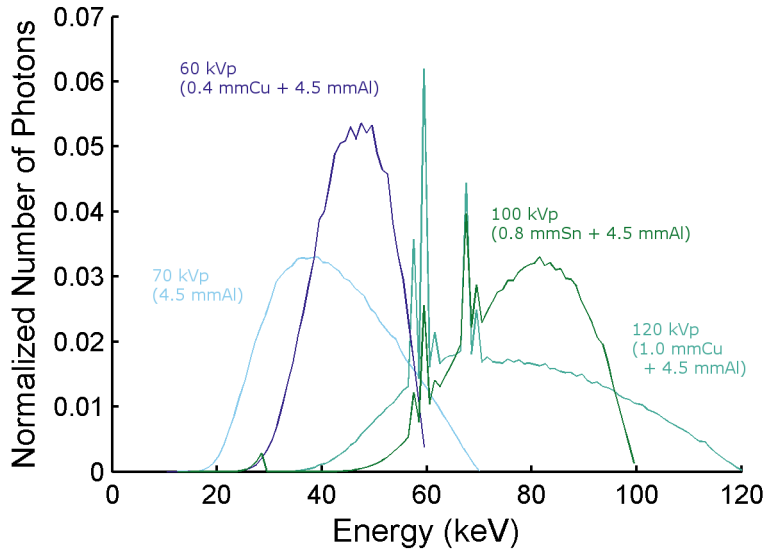

Figure 4.1: Plot of filtered spectrum used with the CCD detector and the CMOS detector. CCD 70 kVp (4.5 mmAl) and 120 kVp (1.0 mmCu + 4.5 mmAl). CMOS detector 60 kVp (0.4 mmCu + 4.5 mmAl) and 100 kVp (0.8 mmSn + 4.5 mmAl). All spectra normalized to the unit area under the curve.

4.2.7.2 Comparison of polyenergetic images with virtual monoenergetic images

The same dual energy projection pairs acquired with the new CMOS detector were processed into polyenergetic images and virtual monoenergetic images. Both sets of images were then fed into the spectral DECT and polynomial fit DECT methods to generate four sets of EAN and RED image volumes. The material regions of interest were used to generate a mean and standard deviation of the EAN and RED for each material insert. The imaging noise and difference between the measured and theoretical EAN and RED are investigated.

4.3 Results

4.3.1 Spectral Optimization

Figure 4.1 shows the simulated micro-CT spectrum for both the CCD and CMOS detectors. Specifications of all the scanner protocols are presented in table 4.1. A copper filter of 0.4 mm

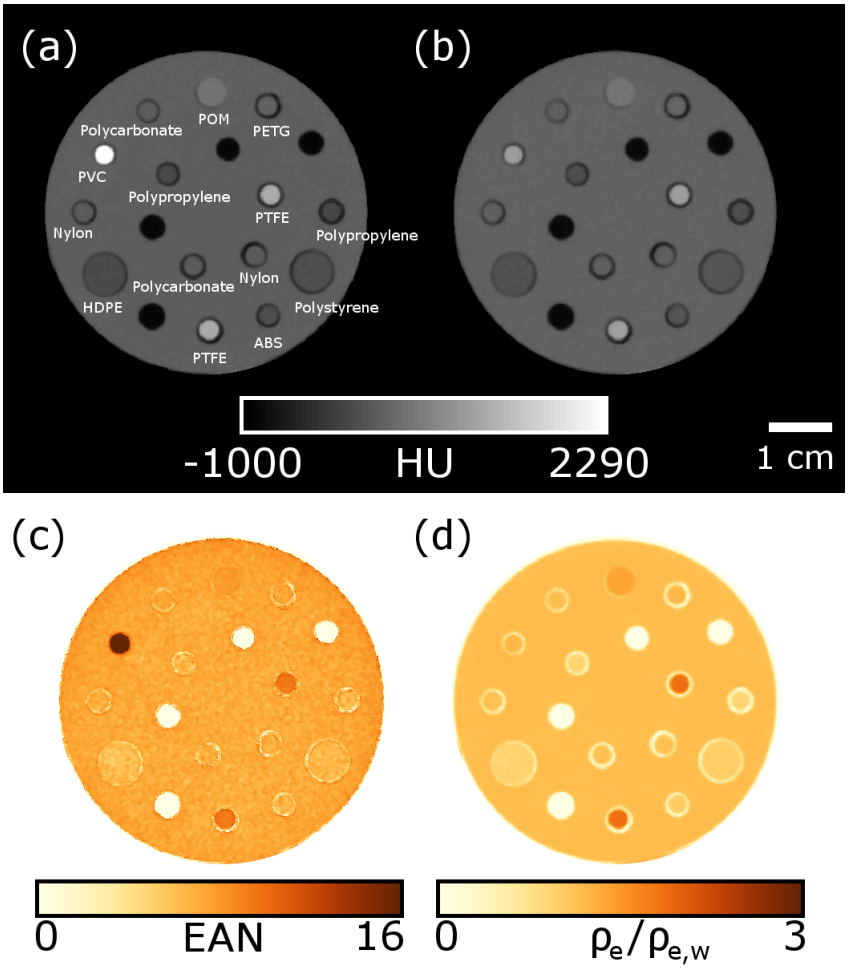

Figure 4.2: Polyenergetic CT images of the large plastics phantom at 60 kVp (a) and 100 kVp (b). The plastic inserts are labelled in (a). The CT images were processed with the polynomial fit DECT method to produce the effective atomic number image (c) and relative electron density image (d).

was chosen for the low energy 60 kVp scan, and a tin filter of 0.8 mm was chosen for the high energy 100 kVp scan. The filter materials of copper and tin were chosen because they are widely available and we were able to achieve reduction of overlap between the low-energy and high-energy spectra.

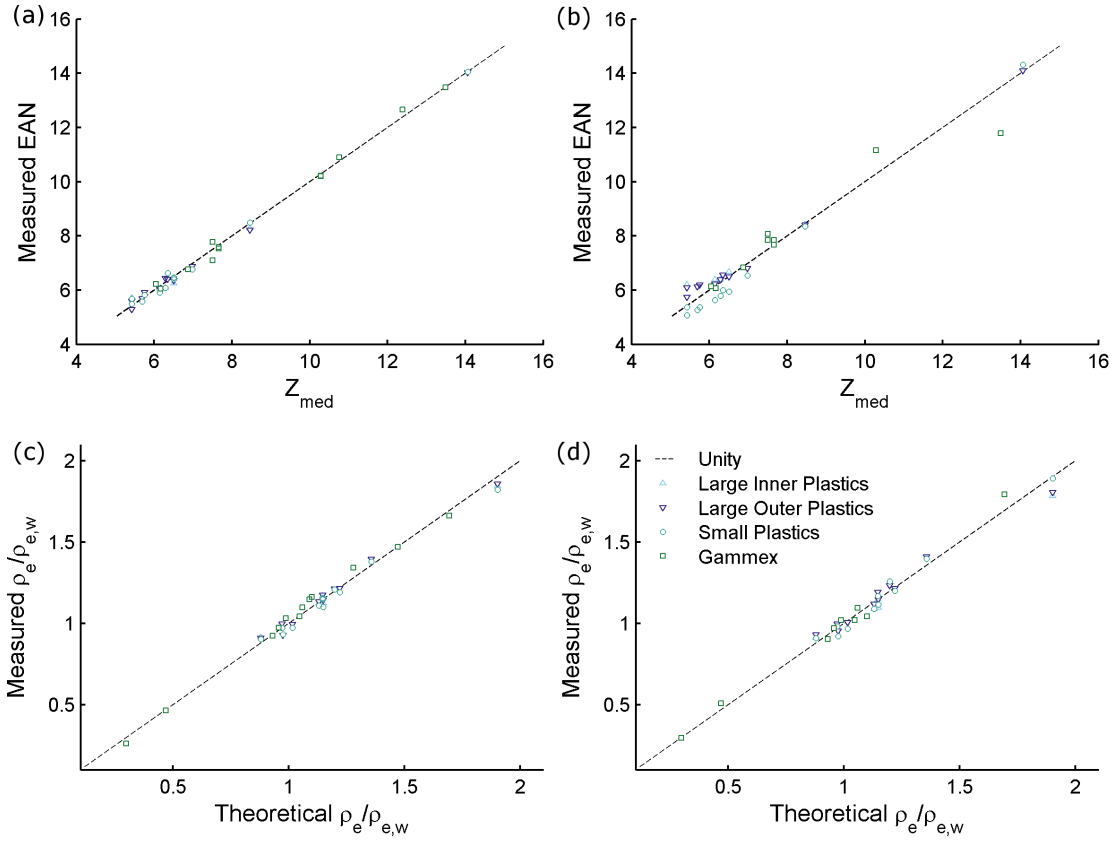

Figure 4.3: Polynomial fit calculated effective atomic number (a,b) and relative electron density (c,d) plotted against their theoretical values for the CMOS detector (a,c) and CCD detector (b,d). Note a linear correction was applied to the CCD detector data (b,d) that was not applied to the same data in chapter 3.

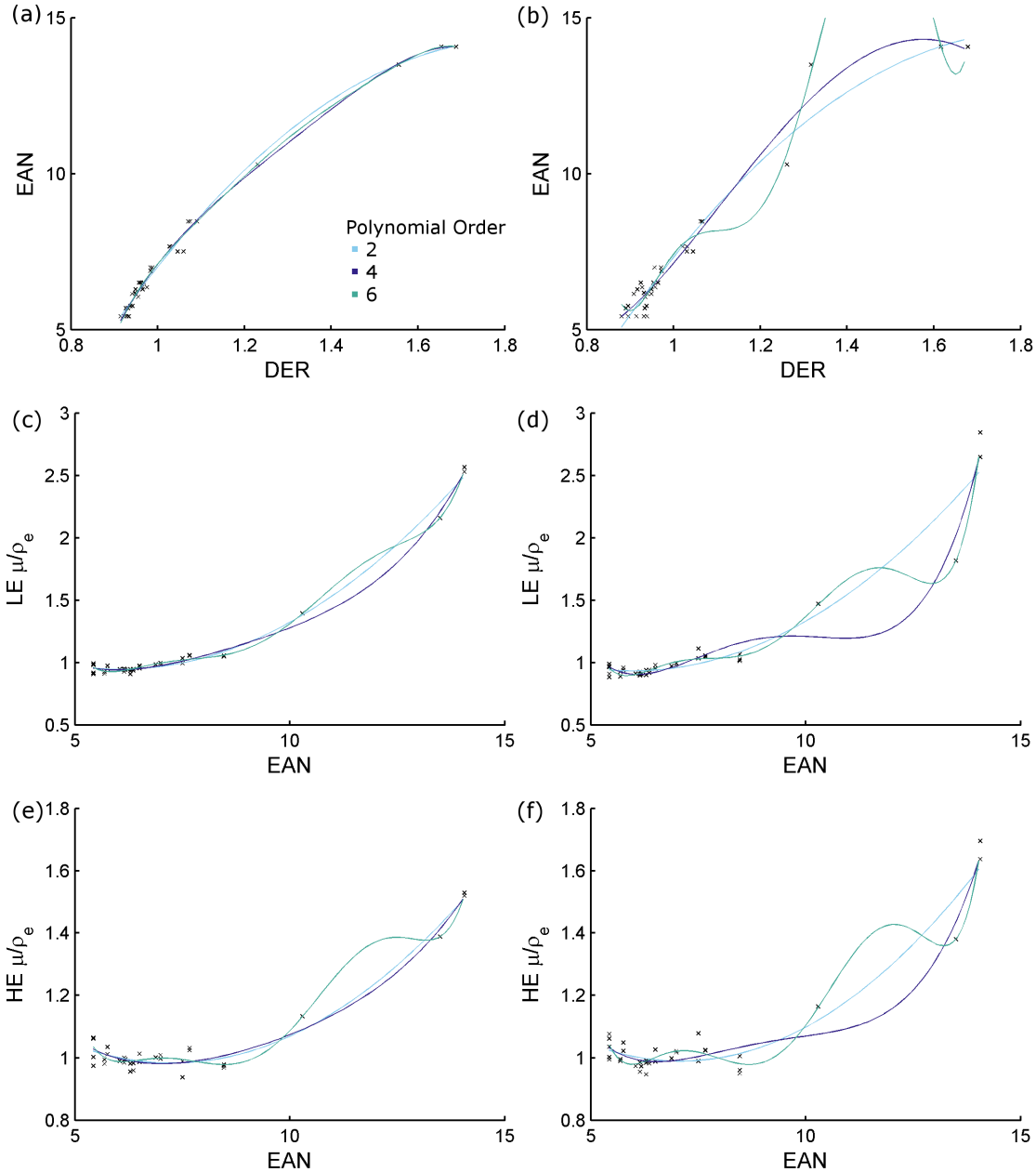

Figure 4.4: Plots of the polynomial fits of the orders (2,4,6) for the CMOS and CCD detector acquired data. Effective atomic number (EAN) is plotted against dual energy ratio (DER) of attenuation coefficients for CMOS (a) and CCD (b). Low energy (LE) RED polynomial for CMOS (c) and CCD (d) are plotted against EAN. High energy (HE) RED polynomial for CMOS (e) and CCD (f) are plotted against EAN.

4.3.2 CMOS versus CCD with polyenergetic images and polynomial fit DECT method

Figure 4.2 displays a representative set of input polyenergetic images and the polynomial fit output from the CMOS detector. Specifically, figure 4.2 presents a slice of the large plastics phantom with polyenergetic 60 kVp and 100 kVp images and corresponding EAN and RED images. To summarize the results for all phantom scans, figure 4.3 plots measured EAN and RED against theoretical values for the CMOS and CCD polyenergetic image data processed with the polynomial fit DECT method. Looking at the effective atomic number plots (figures 4.3a, 4.3b), we can see the high-Z Gammex inserts deviate from the unity line for the CCD data, but not for the CMOS data. Additionally, at the low Z, the CMOS data points are closer to the unity line than the CCD data. Polynomial fits of the EAN as a function of DER are shown in figure 4.4 for the CMOS and CCD acquired data. For the CMOS detector, the EAN and RED polynomials of order 4 were chosen to be employed. A higher order polynomial (6) for the CMOS detector data did not improve the fit noticeably. For the CCD detector, best fits for the EAN and RED polynomials were of order 2. Polynomial orders larger than 2 for the CCD detector introduced over-fitting behaviour to accommodate outliers (figures 4.4b, 4.4d, 4.4f). Artefacts in the source images resulted in many deviations from a monotonic curve.

4.3.3 Polynomial versus spectral fit DECT methods

Table 4.3 lists the root mean squared errors, mean absolute residuals, and maximum absolute residuals of the polynomial fit DECT and spectral DECT methods for the CMOS and CCD detectors. The CCD detector has larger root mean squared errors and residuals compared to the CMOS detector for both polynomial fit or spectral DECT methods. The polynomial fit DECT and spectral DECT methods provide similar output when applied to the same input polyenergetic CT images from the CMOS detector. In contrast, the polynomial fit DECT method provides better output than the spectral method for the CCD detector.

		Polynomial fit			Spectral		
		CCD	CMOS		CCD	CMOS	
		Poly E	Poly E	V Mono E	Poly E	Poly E	V Mono E
EAN	RMSE	0.41	0.18	0.18	0.55	0.19	0.18
	Mean Abs Residual	0.30	0.14	0.14	0.39	0.16	0.14
	Max Abs Residual	1.3	0.52	0.53	2.10	0.48	0.39
RED	RMSE Residual	0.062	0.033	0.033	0.115	0.050	0.054
	Mean Abs Residual	0.042	0.025	0.025	0.084	0.036	0.038
	Max Abs Residual	0.259	0.077	0.077	0.322	0.119	0.126

Table 4.3: Root mean square error (RMSE) and residuals of EAN and RED from the polynomial fit DECT method and spectral DECT method.

4.3.4 CMOS monoenergetic versus polyenergetic; spectral versus polynomial fit DECT method

Table 4.4 presents the noise in the input polyenergetic and monoenergetic images and the output EAN and RED images for the CMOS data processed with both the spectral and polynomial fit methods. There are minimal difference in the noise between the input virtual monoenergetic images and the input polyenergetic CMOS acquired images. As well, the output images have similar noise levels irrespective of the input data (virtual monoenergetic or polyenergetic) or processing method (polynomial or spectral). Table 4.5 presents the accuracy of the four combinations of virtual monoenergetic and polyenergetic input images processed with the spectral or polynomial fit DECT methods applied to the CMOS image data. Overall, there is little difference between the accuracy of the four combinations.

	Input CT (HU) mean (max)				EAN mean (max)				RED mean (max)			
	Poly E		V Mono E		Spectral		Polynomial fit		Spectral		Polynomial fit	
	60 kVp	100 kVp	46 keV	77 keV	Poly E	V Mono E	Poly E	V Mono E	Poly E	V Mono E	Poly E	V Mono E
Plastics	13 (25)	17 (28)	13 (26)	18 (28)	0.32 (0.52)	0.33 (0.53)	0.30 (0.56)	0.32 (0.57)	0.025 (0.038)	0.024 (0.036)	0.017 (0.035)	0.019 (0.040)
Gammex	36 (105)	28 (99)	37 (105)	28 (99)	0.60 (2.88)	0.60 (2.89)	0.60 (2.89)	0.61 (2.91)	0.042 (0.116)	0.041 (0.116)	0.043 (0.127)	0.043 (0.127)

Table 4.4: Root mean square error (RMSE) and residuals of EAN and RED from the polynomial fit DECT method and spectral DECT method.

			Precent difference from theory mean (max)	
			Spectral	Polynomial fit
EAN	Plastics	Polyenergetic	2.2 (7.1)	2.2 (5.5)
		Virtual Monoenergetic	2.0 (7.3)	2.5 (5.8)
	Gammex	Polyenergetic	1.7 (4.4)	1.9 (5.3)
		Virtual Monoenergetic	1.5 (4.8)	2.5 (5.1)
RED	Plastics	Polyenergetic	2.8 (8.3)	2.2 (4.9)
		Virtual Monoenergetic	3.0 (10.3)	2.4 (6.6)
	Gammex	Polyenergetic	4.8 (30.9)	3.5 (12.6)
		Virtual Monoenergetic	4.8 (28.4)	3.9 (12.8)

Table 4.5: Summary of percent difference between theory and measurement of EAN and RED for material sets (Plastics and Gammex), input images sets (polyenergetic and virtual monoenergetic) and DECT algorithms (Spectral and Polynomial fit) for the CMOS detector.

4.3.5 Beam hardening

Most of the difference between the CMOS and CCD data is related to beam hardening. Improvements in beam hardening artefacts are demonstrated in two ways. A reduction in the cupping artefact is illustrated in figure 4.5 by plotting a line profile through images of the large plastics phantom acquired with the CCD and CMOS detectors. Figure 4.6 shows the variation in the CT HU values for 5 plastics that are scanned in 3 different locations. The variation between the mean HU values for the three locations generally is larger for the CCD detector (70 kVp and 120 kVp) compared to the CMOS detector (60 kVp and 100 kVp). This trend is strongest for PTFE. Overall, the combination of the new CMOS detector and filtered x-ray beams have reduced beam hardening related artefacts in the polyenergetic CT images.

4.4 Discussion

The addition of beam filters of 0.4 mm copper for 60 kVp and 0.8 mm tin for 100 kVp have narrowed and separated the spectra. Tin is used in some clinical CT scanners to filter the high energy scan.[4,5] Work by Saito has shown that high Z (57–83) metals can achieve optimal spectra separation for DECT.[8] Saito recommended tungsten for the low energy filter when

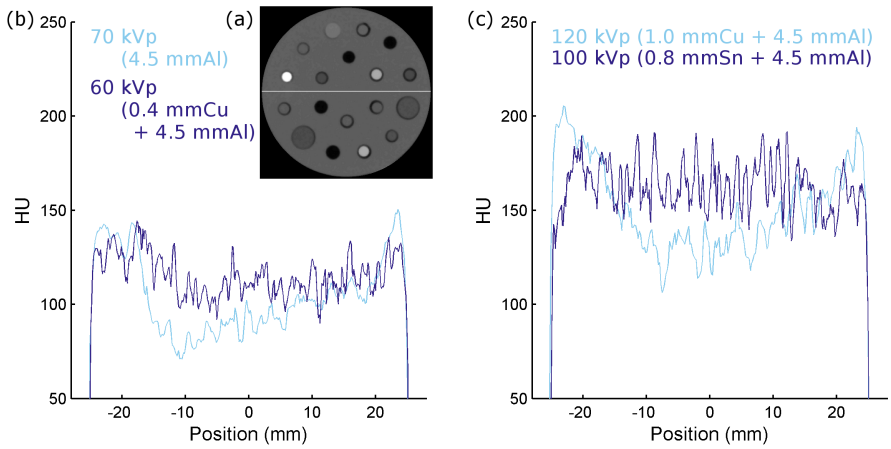

Figure 4.5: An illustration of the reduction of the cupping artefacts in the large plastics phantom. Axial CT slice of the phantom showing the position of the line profile (a). Line profiles of the low energy CT image volumes with spectra of 70 kVp and 60 kVp (b). Line profiles of the high energy CT image volumes with spectra of 120 kVp and 100 kVp (c).

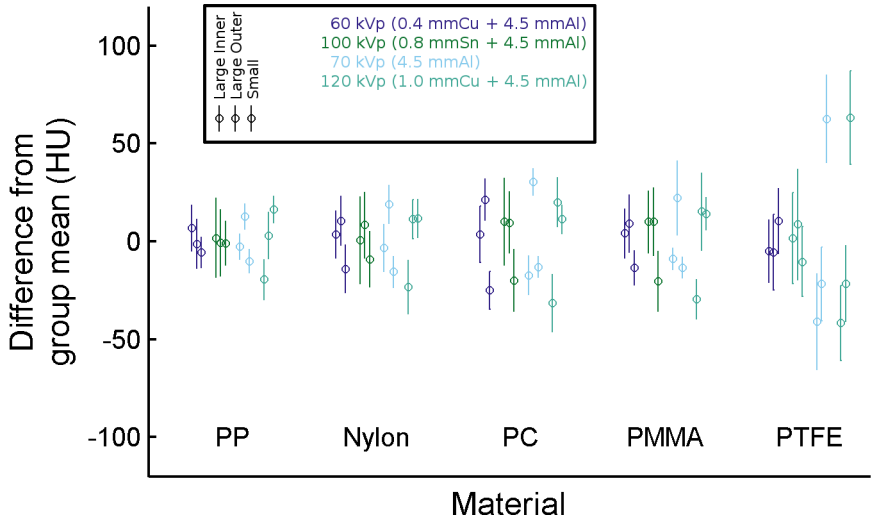

Figure 4.6: Comparison of the difference in HU mean values for each location to the mean of the group for 5 plastic materials. The plastics phantoms were scanned with the new CMOS detector (60 and 100 kVp) and the old CCD detector (70 and 120 kVp). Error bars represent the standard deviation inside the region of interest in HU. Insert locations are plotted in order, left to right: large phantom inner ring, large phantom outer ring and small phantoms. Scanning x-ray spectra are color coded.

paired with a high energy tin filter in clinical dual energy scanners.[5] However, the tube loading requirements with current x-ray hardware and the cost of some K-edge filter metals prevent the implementation. The characteristics of the micro-CT geometry with the more sensitive CMOS detector and small objects allowed us to achieve nearly detector saturating photon flux with the combination of a low 60 kVp setting and a 0.4 mm copper filter, negating the need for a higher kVp with a K-edge tungsten filter.

We have shown a reduction in beam hardening artefacts by using narrower x-ray spectra, made possible by a sensitive CMOS flat panel detector. This improvement comes at the price of increased scanning time to achieve similar quantum noise and a reduced maximum resolution (68 vs. 28 microns). However, the 28 micron CCD scan protocol was restricted to ex-vivo specimens due to the lethal x-ray dose. The maximum resolution for living specimens was approximately 50 microns. As the smallest practical irradiation field is 5 mm $\times$ 5 mm, 68 μm resolution is acceptable to locate a 5 mm diameter tumour. For dose calculation, feature details may be sacrificed for low noise and quantitative accuracy. We have made this trade-off to improve the accuracy of EAN and RED images. The addition of stronger image smoothing filters could further reduce the scanning time. Further investigations are needed into how input image noise affects the output values of EAN and RED, including if differences in the noise level between the low or high energy scans are important. Projection images acquired with the CCD required a correction for a honeycomb pattern and spatial distortions introduced by the fibre optic taper. The CMOS flat panel does not require a distortion correction. Previously with the CCD detector, setup with fluoroscopy was hindered by the obscuring honeycomb pattern and distortions in the images as real-time correction is not computationally feasible. By changing to the CMOS flat panel, the quality of the fluoroscopy images used for animal setup has been improved.

The values of Z_{med} were calculated based on the x-ray spectra of the CT, and could vary between micro-CT and clinical CT. However, the values of Z_{med} computed for the Gammex Model 467 inserts using the micro-CT spectra agreed well with values corresponding to a

clinical CT scanner spectra published by Bourque et al.[22] Eleven of the thirteen insert materials differed by less than their corresponding ΔZ_{med} (theoretically defined variation in EAN). The two remaining materials of LN-300 and SB-3 Cortical Bone differed from the values published by Bourque et al. by 0.047 and 0.013 respectively.

The Gammex inserts are a feasible set for calibration with the narrower x-ray spectra. The EAN measurements of the large bone inserts now agree with the theoretical Z_{med} (figure 4.3a) as beam hardening artefacts have been sufficiently supressed. However the lung inserts suffer from partial volume effects because the air pockets are visible at the micro-CT scanning resolution. Lung mimicking tissue inserts with smaller air pockets would be better for micro-CT.

In this work, virtual monoenergetic images generated from the CMOS acquired data provided no further improvement for EAN and RED measurement (table 4.5). The x-ray beam spectra used with the CMOS detector are relatively hard and the decomposition algorithm is simple. The generation of virtual monoenergetic images would likely have been beneficial for the CCD system setup with softer spectra. Post-processing can be used to suppress beam hardening effects instead of DECT methods, but were not examined in the present study. Decomposing the projections into materials with a larger separation in Z (solid water and iodine, instead of solid water and aluminum) may improve the robustness of the material decomposition.[33] Solid water (plastic) and aluminum were chosen for practical reasons and was the approach used in prior studies.[30,31] The spectral DECT and polynomial fit DECT have similar accuracy. Since polynomial fit DECT is easier to calibrate, requires no information on the spectra and detector response and is computationally simpler, it is the method recommended by our study.

4.5 Conclusion

We have shown that beam hardening artefacts in a micro-CR/RT system were reduced with a new CMOS detector and additional beam filters compared with the factory-installed CCD

detector. With the polynomial fit DECT method, changing from the CCD to the CMOS detector reduced the root mean square error (RMSE) from 0.41 to 0.18 for the effective atomic number, and from 0.06 to 0.03 for the relative electron density. The image-space polynomial fit and spectra DECT algorithms showed similar accuracy when applied to the same input CMOS data, with RMSE of 0.18 versus 0.19 for effective atomic number and 0.03 versus 0.05 for relative electron density. In contrast, the polynomial fit method outperformed the spectral DECT method for the CCD data with RMSE of 0.41 versus 0.55 for effective atomic number and 0.06 versus 0.12 for relative electron density. Polyenergetic and virtual monoenergetic images were processed with two different algorithms to compute effective atomic number and relative electron density, and no differences in accuracy were found among the four possible combinations of algorithms and images from the CMOS detector. With the CMOS detector, we were able to determine effective atomic number with mean error less than 3% and relative electron density with mean error less than 5%. Therefore we recommend the use of polyenergetic images acquired by the CMOS detector and the polynomial fit algorithm for DECT using micro-CT/RT system, as it is computationally simpler and faster than the spectral method. We have shown that the determination of effective atomic numbers and electron densities with micro-CT can be improved using a CMOS detector and optimized spectra compared to the factory-installed CCD.

4.6 References

[1]F. Verhaegen, P. Granton, and E. Tryggestad, "Small animal radiotherapy research platforms", Phys. Med. Biol. **56**, R55–R83 (2011).

[2]F. Verhaegen, S. van Hoof, P. V. Granton, and D. Trani, "A review of treatment planning for precision image-guided photon beam pre-clinical animal radiation studies", Z. Med. Phys. **24**, 323–334 (2014).

[3]M. Bazalova and E. Graves, "The importance of tissue segmentation for dose calculations for kilovoltage radiation therapy", Med. Phys. **38**, 3039–3049 (2011).

[4]A. N. Primak, J. C. Ramirez Giraldo, X. Liu, L. Yu, and C. H. McCollough, "Improved dual-energy material discrimination for dual-source CT by means of additional spectral filtration", Med. Phys. **36**, 1359–1369 (2009).

[5]M. Saito, "Optimized low-kv spectrum of dual-energy ct equipped with high-kv tin filtration for electron density measurements", Med. Phys. **38**, 2850–2858 (2011).

[6]M. Bazalova, J.-F. Carrier, L. Beaulieu, and F. Verhaegen, "Tissue segmentation in Monte Carlo treatment planning: a simulation study using dual-energy CT images", Radiother. Oncol. **86**, 93–98 (2008).

[7]M. Bazalova, J.-F. Carrier, L. Beaulieu, and F. Verhaegen, "Dual-energy CT-based material extraction for tissue segmentation in Monte Carlo dose calculations", Phys. Med. Biol. **53**, 2439–2456 (2008).

[8]M. Saito, "Spectral optimization for measuring electron density by the dual-energy computed tomography coupled with balanced filter method", Med. Phys. **36**, 3631–42 (2009).

[9]R. E. Alvarez and A. Macovski, "Energy-selective reconstructions in X-ray computerised tomography", Phys. Med. Biol. **21**, 733–744 (1976).

[10]L. A. Lehmann, R. E. Alvarez, and A. Macovski, "Generalized image combinations in dual KVP digital radiography", Med. Phys. **8**, 659–667 (1981).

[11]L. Yu, S. Leng, and C. H. McCollough, "Dual-Energy CT-based monochromatic imaging", Am. J. Roentgenol. **199**, S9–S15 (2012).

[12]D. Marin, D. T. Boll, A. Mileto, and R. Nelson, "State of the art: dual-energy CT of the abdomen", Radiology **271**, 327–342 (2014).

[13]R. Taschereau, R. W. Silverman, and A. F. Chatziioannou, "Dual-energy attenuation coefficient decomposition with differential filtration and application to a microCT scanner", Phys. Med. Biol. **55**, 1141–55 (2010).

[14]M. Torikoshi, T. Tsunoo, M. Sasaki, M. Endo, Y. Noda, Y. Ohno, T. Kohno, K. Hyodo, K. Uesugi, and N. Yagi, "Electron density measurement with dual-energy x-ray CT using synchrotron radiation", Phys. Med. Biol. **48**, 673–85 (2003).

[15]G. Landry, B. Reniers, P. V. Granton, B. van Rooijen, L. Beaulieu, J. E. Wildberger, and F. Verhaegen, "Extracting atomic numbers and electron densities from a dual source dual energy CT scanner: experiments and a simulation model", Radiother. Oncol. **100**, 375–379 (2011).

[16]G. Landry, P. V. Granton, B. Reniers, M. C. Ollers, L. Beaulieu, J. E. Wildberger, and F. Verhaegen, "Simulation study on potential accuracy gains from dual energy CT tissue segmentation for low-energy brachytherapy Monte Carlo dose calculations", Phys. Med. Biol. **56**, 6257–6278 (2011).

[17]B. J. Heismann, J. Leppert, and K. Stierstorfer, "Density and atomic number measurements with spectral x-ray attenuation method", J. Appl. Phys. **94**, 2073 (2003).

[18]M. M. Goodsitt, E. G. Christodoulou, and S. C. Larson, "Accuracies of the synthesized monochromatic CT numbers and effective atomic numbers obtained with a rapid kVp switching dual energy CT scanner", Med. Phys. **38**, 2222–2232 (2011).

[19]J. K. Van Abbema, A. Van der Schaaf, W. Kristanto, J. M. Groen, and M. J. W. Greuter, "Feasibility and accuracy of tissue characterization with dual source computed tomography", Phys. Medica **28**, 25–32 (2012).

[20]G. Landry, J. Seco, M. Gaudreault, and F. Verhaegen, "Deriving effective atomic numbers from DECT based on a parameterization of the ratio of high and low linear attenuation coefficients", Phys. Med. Biol. **58**, 6851–66 (2013).

[21]N. Hünemohr, B. Krauss, C. Tremmel, B. Ackermann, O. Jäkel, and S. Greilich, "Experimental verification of ion stopping power prediction from dual energy CT data in tissue surrogates", Phys. Med. Biol. **59**, 83–96 (2014).

[22]A. E. Bourque, J.-F. Carrier, and H. Bouchard, "A stoichiometric calibration method for dual energy computed tomography", Phys. Med. Biol. **59**, 2059–88 (2014).

[23]J. K. van Abbema, M.-J. van Goethem, M. J. W. Greuter, A. van der Schaaf, S. Brandenburg, and E. R. van der Graaf, "Relative electron density determination using a physics based parameterization of photon interactions in medical DECT", Phys. Med. Biol. **60**, 3825 (2015).

[24]R. A. Rutherford, B. R. Pullan, and I. Isherwood, "Measurement of effective atomic number and electron density using an EMI scanner", Neuroradiology **11**, 15–21 (1976).

[25]J.-É. Tremblay, S. Bedwani, and H. Bouchard, "A theoretical comparison of tissue parameter extraction methods for dual energy computed tomography", Med. Phys. **41**, 081905 (2014).

[26]M. D. Jensen, W. T. Hrinivich, J. A. Jung, D. W. Holdsworth, M. Drangova, J. Chen, and E. Wong, "Implementation and commissioning of an integrated micro-CT/RT system with computerized independent jaw collimation", Med. Phys. **40**, 081706 (2013).

[27]J. H. Siewerdsen, A. M. Waese, D. J. Moseley, S. Richard, and D. A. Jaffray, "Spektr: a computational tool for x-ray spectral analysis and imaging system optimization", Med. Phys. **31**, 3057 (2004).

[28]D. Rogers, B. Faddegon, G. Ding, C.-M. Ma, J. We, and T. Mackie, "BEAM: a Monte Carlo code to simulate radiotherapy treatment units", Med. Phys. **22**, 503–524 (1995).

[29]S. Rit, M. Vila Oliva, S. Brousmiche, R. Labarbe, D. Sarrut, and G. C. Sharp, "The Reconstruction Toolkit (RTK), an open-source cone-beam CT reconstruction toolkit based on the Insight Toolkit (ITK)", J. Phys.: Conf. Ser **489**, 012079 (2014).

[30]K.-S. Chuang and H. K. Huang, "A fast dual-energy computational method using isotransmission lines and table lookup", Med. Phys. **14**, 186 (1987).

[31]C. K. Wong and H. K. Huang, "Calibration procedure in dual-energy scanning using the basis function technique", Med. Phys. **10**, 628 (1983).

[32]M. J. Berger, J. H. Hubbell, S. M. Seltzer, J. Chang, J. S. Coursey, R. Sukumar, D. S. Zucker, and K. Olsen, *XCOM: Photon Cross Section Database (Version 1.5)*, tech. rep. (National Institute of Standards and Technology, Gaithersburg, MD, 2010).

[33]F. Kelcz, P. M. Joseph, and S. K. Hilal, "Noise considerations in dual energy CT scanning", Med. Phys. **6**, 418–425 (1979).

Chapter 5

Conclusion and Future Work

5.1 Overview and Summary

Radiation therapy has advanced over the past few decades through major technological developments.[1–6] The multi-leaf collimation technologies of Intensity Modulated Radiation Therapy (IMRT) and the addition of on-board CT detectors for Image-Guided Radiation Therapy (IGRT) have enabled the delivery of more localized radiation to complex geometric targets with greater accuracy and precision.[1,2,5,7–9] The next challenge will be to define the targets using biological information using functional and molecular medical imaging.[10,11] Preclinical studies are an important aspect to the advancement of radiation oncology as the field moves towards more biologically-based targeting and response monitoring.[6] Preclinical studies are also necessary to investigate the combination of new targeted drugs with targeted radiation therapy.[12] Therefore, the development of preclinical image-guided conformal irradiators and techniques for small animal research are a critical component of enabling basic science studies that will test and form the hypotheses for clinical trials. While the clinical technology has advanced, preclinical technology development has not kept pace. Many radiobiology studies have been performed using wide-field irradiations of the whole or large fraction of the animal body.[13–16] Such irradiations do not mimic the conformal and image-guided treatments available for human-scale radiotherapy. As outlined by Verhaegen et al., a number of preclinical image-guided systems have therefore been developed to address the gap between clinical and

preclinical irradiation technology.[13] Even with these new platforms, a number of limitations were identified at the outset of this thesis. These include the maximum animal size amenable to treatment in a micro-CT based system, production of asymmetric off-axis fields, complex computerized collimation, respiratory beam gating, and dual-energy CT for use in Monte Carlo calculation of dose distributions at kilovoltage energies. This thesis has addressed these issues.

In chapter 2, we presented the design, construction and commissioning of a set of computer-controlled motorized jaws for a micro-CT/RT system in order to perform conformal image-guided small animal radiotherapy. A system of custom-built motorized orthogonal jaws was designed and evaluated, which allows the delivery of off-axis rectangular fields and enables rat irradiation. Mechanical performance of the jaws was characterized using radiochromic film and portal imaging. Square beam profiles ranging from 2×2 to 60×60 mm^2 were measured using EBT2 film in the center of a $70 \times 70 \times 22$ mm^3 solid water block. Similarly, absolute depth dose was measured in a solid water and EBT2 film stack $50 \times 50 \times 50$ mm^3. A calibrated Farmer ion chamber was used to measure the dose output of three field sizes: 50×50, 40×40, and 30×30 mm^2. Elliptical cylinder target plans were delivered to films to assess overall system performance. Respiratory-gated treatment was implemented on the system and initially verified using a phantom subjected to simple sinusoidal motion. A Monte Carlo beam model of the irradiator was created using BEAMnrc[17] for comparison with the measurements and manual dose planning. A sample image-guided partial lung irradiation in a rat was demonstrated. The averaged random error of positioning each jaw was less than 0.1 mm. Relative dose output factors measured with the ion chamber agreed with Monte Carlo simulations within 2%. Beam profiles and absolute depth dose curves measured from the films agreed with simulations within measurement uncertainty. Respiratory-gated treatments applied to a phantom moving with a peak-to-peak amplitude of 5 mm showed reduced beam penumbra (80%–20%) from 3.9 to 0.8 mm. Overall, a set of computer-controlled motorized jaws for a micro-CT/RT system were constructed with position reliably better than 0.1 mm. The hardware

system was thereby characterized for image-guided conformal radiotherapy for small animals adding the capability of respiratory-gated delivery.

In chapter 3, Dual-Energy CT (DECT) was developed for micro-CT in order to obtain tissue electron density and effective atomic number data for improving dose computations at kilovoltage energy. The experimental investigations identified some challenges unique to dual-energy micro-CT (DEmCT). Images were acquired sequentially at 70 kVp (4.5 mmAl) and 120 kVp (4.5 mmAl + 1 mmCu). Four plastics phantoms (1 large, 3 small, 11 materials) and two solution sets of $CaCl_2$ and EtOH were designed for DEmCT. Additionally, 18 electron density inserts and a mouse were scanned. Using a published clinical DECT algorithm, we found the measured and theoretical relative electron density values agreed with a median percent difference less than 2.5%. The measured and theoretical effective atomic number values agreed with a median percent difference less than 3.0% for effective atomic numbers less than 8, while measurement systematically underestimated theoretical values for effective atomic numbers greater than 8 which could be corrected by a calibration. The small phantoms had better agreement than the large phantom with 8 of 11 versus 2 of 16 material measurements having effective atomic number percent differences less than 3.5%; beam hardening was found to be the major contributing factor to this discrepancy. Effective atomic number and relative electron density maps were demonstrated in the mouse, despite motion and beam-hardening artefacts. Overall, when beam-hardening and motion artefacts were minimized, the accuracies approached that of modern clinical CT scanners.

In chapter 4, we quantified the improvements in dual energy micro-CT performance using a complementary metal oxide semiconductor (CMOS) x-ray detector panel in place of a charge coupled device (CCD) detector. Four custom micro-CT phantoms with plastic inserts and commercial inserts with known material composition as used for clinical CT electron density calibration were employed in this study. Dual energy image data of phantoms were first acquired on a micro-CT with a factory-installed CCD detector using a pair of previously optimized energy spectra. A CMOS panel detector was then installed and commissioned on

the micro-CT/RT. Beam filters were then chosen and implemented by optimizing two x-ray spectra for dual energy scans with the CMOS detector. Two published clinical dual energy CT (DECT) image-space algorithms were implemented to determine effective atomic number and relative electron density: an explicit spectra-based method and an empirical polynomial fit method. Data obtained from the two detectors were processed with both DECT algorithms and the effective atomic number and relative electron density of the various material inserts were compared. We further tested the utility of virtual monoenergetic images in conjunction with both DECT algorithms for the CMOS acquired data. The CMOS detector demonstrated better accuracy and precision than the CCD detector with the polynomial fit DECT method, reducing root mean square error (RMSE) from 0.41 to 0.18 for the effective atomic number, and from 0.06 to 0.03 for the relative electron density. The image-space polynomial fit and spectra DECT algorithms showed similar accuracy when applied to the same input CMOS data, with RMSE of 0.18 vs. 0.19 for effective atomic number and 0.03 vs. 0.05 for relative electron density. In contrast, the polynomial fit outperformed the spectral DECT algorithm for the CCD data with RMSE of 0.41 vs. 0.55 for effective atomic number and 0.06 vs. 0.12 for relative electron density. Virtual monoenergetic images used as input provided no improvement compared to polyenergetic image input with CMOS acquired images. Using the CMOS detector and any method proposed in this work, we were able to determine the effective atomic number with mean error less than 3% and relative electron density with mean error less than 5%. We demonstrated that the CMOS detector outperformed the CCD detector for the determination of effective atomic numbers and relative electron densities. The higher efficiency of the CMOS detector allowed us to increase the beam filtration and harden the x-ray spectra more than we could with the CCD. The combination of using polyenergetic images, CMOS detector, and the empirical polynomial fit DECT image-space algorithm provided the best accuracy as well as computational simplicity for the measurement of effective atomic number and relative electron density.

5.2 Summary of conclusions

In summary, we have created a small animal image-guided conformal radiotherapy platform built upon a commercial micro-CT scanner gantry. This was achieved by 1) designing, building and commissioning a set of computer controlled asymmetric jaw collimators and 2) designing and building a computer controlled beam filter wheel and replacement of the imaging detector. A Monte Carlo dosimetry code was commissioned for dose calculations for this micro-radiotherapy system. Finally, dual energy micro-CT was investigated for measuring the effective atomic number and relative electron density of materials to improve dose computation accuracy. Beam hardening effects that limited the accuracy of dual energy micro-CT were overcome by optimization of the dual energy spectra. Table 5.1 updates table 1.1 to include the system developed in this thesis.

5.3 Limitations

One limitation of the system is the low dose rate of approximately 0.3 Gy/min. As the radiotherapy platform developed in this thesis is based on a micro-CT, the diagnostic x-ray tube and generator are not designed for therapeutic radiation dose rates. The low dose rate has both practical and possible biological consequences. First, the low dose rate limits the number of animals that can be treated in a day, making studies with many animals less appealing with this system. Secondly, the low dose rate leads to long treatment times, during which cell repair mechanisms can become active and counteract the biological radiation damage.[18–21] These limitations are not insurmountable, as the biological repair during long treatment times can be counteracted with an increased dose prescription. When comparing studies conducted on this system to that of other investigators, the dose rate effects will need to be considered. As for the throughput of the system, many of the studies performed with the system have used few animals as they undergo extensive time-consuming imaging. Respiratory-gated therapy does not introduce an additional time penalty. As the duty cycle is approximately 10%, there is

	SARRP (Johns Hopkins)	X-Rad 225Cx (Toronto and Masstricht)	Stanford University	Western University London, ON
Maximum accelerating potential (kVp)	225	225	120	140
Interchangeable beam filters	Yes	Yes	No	Yes
Dose rate (Gy/min)	4	4	2	0.3
Collimation	Fixed cones (Jaw option recently available)	Fixed cones	Computerized variable aperature	Computerized jaws
Field sizes	Circular and Square 0.5 mm ⊘ – 10 mm × 10 mm	Circular and Square 1.0 mm ⊘ – 10 mm × 10 mm	Pseudo-circular 0.1 – 6 cm ⊘	Rectangular 2 mm × 2 mm – 60 mm × 60 mm
Beam direction	non-coplanar	coplanar	coplanar	coplanar
Asymmetric/ off-axis fields	No	No	No	Yes
Stage translation	3D + rotation	3D	3D (contrained by CT bore)	SI computerized AP manual
Respiratory Gating	No (Gated shutter option recently) available)	No	No	Yes (+ Cardiac)
Image resolution (μm)	130	200	49	68
Targeting accurracy (μm)	200	200	100	200–300
Dose calculation and planning system	Muriplan (Commericial)	SmART-Plan (Maastro Clinic, Commercial)	RT_Image BEAMnrc (Stanford, in-house)	BEAMnrc Dose calc. only

Table 5.1: Comparison of select image-guided small animal irradiation systems with the system developed in this thesis.

no need to reduce the duty cycle further for respiratory-gated therapy. The x-ray "on" time is redistributed to occur within the gated window corresponding to end exhalation.

A second limitation is the treatment beam energy. At 140 kVp, the system is close to the lower limit of preclinical systems, as most are operating at 225 kVp. The lower treatment kVp means that photoelectric effects are more prominent and must be accounted for in the computation of the dose distribution in the mouse. Bone dose enhancement must be considered. The lower energy also has implications for physical dosimetry. Many dosimeters can have energy dependent response at energies below 100 keV, including ion chambers and film. The dose measurements used in this thesis were cross-calibrated against the LRCP local standard ion chamber using calibration factors at 80 and 100 kVp. A second comparison with another traceable standard would give increased confidence in the commissioning.

Soft tissue contrast is lacking in CT and the identification of an orthotopic legion by CT alone will be difficult. To overcome this limitation in target identification using this system, other imaging modalities, such as MRI, nuclear medicine, ultrasound or optical imaging will be required.[22,23]

The Monte Carlo dose calculations shown in the thesis have been performed with single energy CT information and simplified tissue segmentation. As discussed later, the change to DECT based tissue segmentation for Monte Carlo dosimetry will improve the accuracy and confidence in the dose calculations.

The phantom materials used in chapters 3 and 4 were not ideal. The composition of the plastics are not well known and only approximate tissue atomic composition. The clinical electron density inserts have known composition and reflect tissues, but are not sized appropriately for a small animal system.

Finally, in chapter 4 the comparison of the CCD and CMOS detector may be biased, as the CCD acquisition was not optimized to the same extent of the CMOS detector. The CCD failed before we could perform such optimization, and was indeed the reason for acquiring the

CMOS detector. The deficiencies in the accuracy of the results from the CCD detector cannot be completely attributed to inherent limitations of the detector.

5.4 Future Work

A number of extensions of the thesis work are possible, with several described in this section.

5.4.1 CMOS detector

First, the installation of the CMOS flat panel detector has effectively created a new higher performance micro-CT system. The imaging performance of this system has not been fully characterized in terms of image quality. The previous configuration was characterized with the vmCT phantom.[24,25] A similar evaluation should be completed to determine parameters such as the modulation transfer function (MTF) for this new scanner configuration. Additionally, the set of imaging protocols needs to be updated and optimized for the new CMOS detector configuration. The work of chapter 4 only examined optimizing scans for dual energy material classification. Imaging protocols need to be developed and optimized for other simpler imaging tasks with due consideration for animal dose reduction. Digital subtraction angiography (DSA) has been successfully demonstrated in small animals, but has not been widely adopted.[26] DSA has been used to examine the tumour blood supply in small animals.[27]The framerate of the previous CCD was too slow for dynamic studies and discouraged investigation of DSA with this system. The 45 fps framerate of the CMOS flat panel provides a new opportunity to implement DSA or tomographic DSA in small animals.

5.4.2 Small animal tissue characterization

As mentioned in the limitations above, the set of materials used for testing dual energy scanning in chapters 3 and 4 were not ideal as tissue substitutes. A new set of phantoms should be constructed from well-characterized materials with small dimensions appropriate for the micro-

CT. The self-evident approach would be to scale down a clinical electron density phantom composed of tissue mimicking plastics to the size of a rat and mouse. Following dual energy calibration and verification on the appropriate phantom, a series of animal tissues should be scanned to determine if human tissue composition estimates are appropriate for small animal tissues. Ideally, independent measures of small animal tissue composition should be made to corroborate radiological measures. Once small animal tissue compositions are analysed, they can be implemented in the Monte Carlo dose calculation codes to improve dose calculation accuracy. Furthermore, a dosimetry error budget needs to be investigated to determine the level of accurracy required from the dose calculation. Then it will be possible to clearly define the accuracy needed in the DEmCT measurements of effective atomic number and relative electron density. For context, an error of 0.5 in effective atomic number leads to a local relative dose difference of approximately 8% in dense bone, and 14% in soft tissues for the 140 kVp therapy beam.

5.4.3 Inverse planning

The overall objective of this thesis was to develop preclinical radiation therapy to better match clinical practice. One area that was not addressed in this thesis is inverse treatment planning. A core part of IMRT is the ability of the planning system to determine the beam intensity profiles based upon a number of clinical objectives. To date, treatment planning on dedicated preclinical radiation therapy platforms is restricted to forward planning. In forward planning, the planner chooses the beam shapes and weights. The jaws system developed in this thesis may be more amenable to implementing inverse planning, as the jaws mirror the clinical machine, and algorithms for jaw sequencing may be implemented.[28,29]

5.4.4 Gated radiotherapy

One benefit of the diagnostic x-ray generator and tube is the temporal control of the radiation exposures. This allows gating of the delivery of radiation based on respiratory, or potentially

cardiac, waveforms. Chapter 2 only demonstrated proof-of-concept for respiratory gating using sinusoidal breathing patterns. Further investigations are possible to quantify how the system performs with different respiratory waveforms. Cardiac motion may be more of a concern for small animals comparted to humans due to the relatively larger size of the heart compared to the lungs. The impact of cardiac motion on small animal thoracic tumours can uniquely be investigated with cardiac gating available on this system. Moving beyond film, the motion blur of the dose deposited could be measured biologically by mapping γ-H2AX staining in animals irradiated with and without gating .

5.4.5 Potential preclinical studies

With the availability of the new micro-CT/RT radiotherapy system, a large variety of preclinical irradiation studies are now possible. A few potential extensions to collaborative studies that have used the system are discussed.

In collaboration with K. Thind et al., it was shown the number of macrophages are increased in the lung following conformal irradiation with the micro-CT/RT.[30] Lactate to pyruvate levels in irradiated lung were found to be elevated as measured by C-13 MRI. Work to examine these biological markers, and eventually determine mechanisms for the increase in macrophage numbers and source of the elevated lactate to pyruvate levels is an area of potential interest. Work into immunohistochemical staining of the macrophages to identify their activation state is a possible companion avenue of exploration.

Studies of primary brain tumour or brain metastasis models have been performed using this system. A pilot study with M. Cooper, S. Schmid and M. Hebb (unpublished) examined combining radiotherapy with electric field therapy for glioma. The system developed in this thesis allows for the imaging and targeting of the implanted electrode and surrounding tumour.

5.5 Impact and Significance

A small animal conformal image-guided radiation therapy system has been built that addresses some of the previous limitations of other similar systems available at the start of this thesis. A computer controlled, asymmetric jaw collimator was designed, built and commissioned that offers a major advancement over the manual collimators of other systems. Computerized collimation is a key component towards bringing Intensity Modulated Radiation Therapy (IMRT) to the preclinical setting. Respiratory gating is another clinically available feature now made possible in a preclinical radiotherapy systems. This thesis documents one of the first implementations of computerized asymmetric jaw collimation and respiratory gating on a dedicated preclinical system. Finally, measuring effective atomic number and relative electron density are crucial to accurate dose calculations with the kilovoltage energies used in small animal radiotherapy. One of the first applications of dual energy CT techniques for measuring effective atomic number and relative electron density to micro-CT is presented in this thesis. A preclinical system that allows controlled studies of radiobiological response to radiation in vivo using irradiation techniques similar to those achievable clinically will become a useful tool to optimize biologically-driven treatment planning for future cancer patients.

5.6 References

[1] A. Ahnesjö, B. Hårdemark, U. Isacsson, and A. Montelius, "The IMRT information process–mastering the degrees of freedom in external beam therapy", Phys. Med. Biol. **51**, R381–R402 (2006).

[2] L. A. Dawson and M. B. Sharpe, "Image-guided radiotherapy: rationale, benefits, and limitations", Lancet Oncol. **7**, 848–858 (2006).

[3] D. I. Thwaites and J. B. Tuohy, "Back to the future: the history and development of the clinical linear accelerator", Phys. Med. Biol. **51**, R343–R362 (2006).

[4] D. Verellen, M. D. Ridder, and G. Storme, "A (short) history of image-guided radiotherapy", Radiother. Oncol. **86**, 4–13 (2008).

[5] J.-Y. Jin, N. Wen, L. Ren, C. Glide-Hurst, and I. J. Chetty, "Advances in treatment techniques", Cancer J. **17**, 166–176 (2011).

[6]K. T. Butterworth, K. M. Prise, and F. Verhaegen, "Small animal image-guided radiotherapy: status, considerations and potential for translational impact", Brit. J. Radiol. **88**, 20140634 (2015).

[7]T. R. Mackie, J. Kapatoes, K. Ruchala, W. Lu, C. Wu, G. Olivera, L. Forrest, W. Tome, J. Welsh, R. Jeraj, P. Harari, P. Reckwerdt, B. Paliwal, M. Ritter, H. Keller, J. Fowler, and M. Mehta, "Image guidance for precise conformal radiotherapy", Int. J. Radiat. Oncol., Biol., Phys. **56**, 89–105 (2003).

[8]T. Bortfeld, "IMRT: a review and preview", Phys. Med. Biol. **51**, R363–79 (2006).

[9]W. Schlegel, "If you can't see it, you can miss it: the role of biomedical imaging in radiation oncology", Radiat. Prot. Dosim. **139**, 321–326 (2010).

[10]C. C. Ling, J. Humm, S. Larson, H. Amols, Z. Fuks, S. Leibel, and J. A. Koutcher, "Towards multidimensional radiotherapy (MD-CRT): biological imaging and biological conformality", Int. J. Radiat. Oncol., Biol., Phys. **47**, 551–560 (2000).

[11]S. M. Bentzen and V. Gregoire, "Molecular imaging-based dose painting: a novel paradigm for radiation therapy prescription", Semin. Radiat. Oncol. **21**, 101–110 (2011).

[12]T. Z. Vern and W. Small, Jr., "Targeted therapies: definitions, limitations, and future directions", in *Combining targeted biological agents with radiotherapy: current status and future directions*, edited by W. Small, Jr. (Demos Medical Publishing, New York, NY, 2008) Chap. 1, pp. 1–15.

[13]F. Verhaegen, P. Granton, and E. Tryggestad, "Small animal radiotherapy research platforms", Phys. Med. Biol. **56**, R55–R83 (2011).

[14]N. S. Bese, C. Umay, S. Serdengecti, N. Kepil, N. Sut, T. Altug, and A. Ober, "The impact of trastuzumab on radiation-induced pulmonary fibrosis: results of an experimental study", Med. Oncol. **27**, 1415–9 (2010).

[15]Z. N. Rabbani, J. Mi, Y. Zhang, M. Delong, I. L. Jackson, K. Fleckenstein, F. K. Salahuddin, X. Zhang, B. Clary, M. S. Anscher, and Z. Vujaskovic, "Hypoxia inducible factor 1α signaling in fractionated radiation-induced lung injury: role of oxidative stress and tissue hypoxia", Radiat. Res. **173**, 165–74 (2010).

[16]T. Eldh, F. Heinzelmann, a. Velalakan, W. Budach, C. Belka, and V. Jendrossek, "Radiation-induced changes in breathing frequency and lung histology of C57BL/6J mice are time- and dose-dependent", Strahlenther. Onkol. **188**, 274–81 (2012).

[17]D. Rogers, B. Faddegon, G. Ding, C.-M. Ma, J. We, and T. Mackie, "BEAM: a Monte Carlo code to simulate radiotherapy treatment units", Med. Phys. **22**, 503–524 (1995).

[18]J. Z. Wang, X. Li, W. D. D'Souza, and R. D. Stewart, "Impact of prolonged fraction delivery times on tumor control: a note of caution for intensity-modulated radiation therapy (IMRT)", Int. J. Radiat. Oncol., Biol., Phys. **57**, 543–552 (2003).

[19]X. Mu, P.-O. Löfroth, M. Karlsson, and B. Zackrisson, "The effect of fraction time in intensity modulated radiotherapy: theoretical and experimental evaluation of an optimisation problem", Radiother. Oncol. **68**, 181–187 (2003).

[20]V. Moiseenko, C. Duzenli, and R. E. Durand, "In vitro study of cell survival following dynamic MLC intensity-modulated radiation therapy dose delivery", Med. Phys. **34**, 1514 (2007).

[21]J. M. Bewes, N. Suchowerska, M. Jackson, M. Zhang, and D. R. McKenzie, "The radiobiological effect of intra-fraction dose-rate modulation in intensity modulated radiation therapy (IMRT)", Phys. Med. Biol. **53**, 3567–78 (2008).

[22]J. S. Lewis, S. Achilefu, J. Garbow, R. Laforest, and M. Welch, "Small animal imaging", Eur. J. Cancer **38**, 2173–2188 (2002).

[23]W. Koba, K. Kim, M. L. Lipton, L. Jelicks, B. Das, L. Herbst, and E. Fine, "Imaging devices for use in small animals", Semin. Nucl. Med. **41**, 151–165 (2011).

[24]M. Bahri, G. Warnock, A. Plenevaux, P. Choquet, A. Constantinesco, E. Salmon, A. Luxen, and A. Seret, "Performance evaluation of the General Electric eXplore CT 120 micro-CT using the vmCT phantom", Nucl. Instrum. Methods Phys. Res. A **648**, S181–S185 (2011).

[25]L. Du, J. Umoh, H. Nikolov, S. Pollmann, T.-Y. Lee, and D. Holdsworth, "A quality assurance phantom for the performance evaluation of volumetric micro-CT systems", Phys. Med. Biol. **52**, 7087–7108 (2007).

[26]C. T. Badea, M. Drangova, D. W. Holdsworth, and G. A. Johnson, "In vivo small-animal imaging using micro-CT and digital subtraction angiography", Phys. Med. Biol. **53**, R319–50 (2008).

[27]C. T. Badea, L. W. Hedlund, M. De Lin, J. F. Boslego Mackel, and G. A. Johnson, "Tumor imaging in small animals with a combined micro-CT/micro-DSA system using iodinated conventional and blood pool contrast agents", Contrast Media Mol. Imaging **1**, 153–164 (2006).

[28]J.-R. Dai and Y.-M. Hu, "Intensity-modulation radiotherapy using independent collimators: an algorithm study", Med. Phys. **26**, 2562–2570 (1999).

[29]J. Anderson, R. Symonds-Tayler, and S. Webb, "Investigating the fundamentals of IMRT decomposition using ten simple collimator models", Phys. Med. Biol. **51**, 2225–2236 (2006).

[30]K. Thind, M. D. Jensen, E. Hegarty, A. P. Chen, H. Lim, F. Martinez-Santiesteban, J. Van Dyk, E. Wong, T. J. Scholl, and G. E. Santyr, "Mapping metabolic changes associated with early Radiation Induced Lung Injury post conformal radiotherapy using hyperpolarized (13)C-pyruvate Magnetic Resonance Spectroscopic Imaging", Radiother. Oncol. **110**, 317–322 (2014).

Appendix A

Film processing details

This appendix is adapted from the appendix of the research article, "Implementation and commissioning of an integrated micro-CT/RT system with computerized independent jaw collimation". Reprinted with permission from M. D. Jensen, W. T. Hrinivich, J. A. Jung, D. W. Holdsworth, M. Drangova, J. Chen and E. Wong, Medical Physics **40**, 081706 (2013).

© 2013 American Association of Physicists in Medicine

doi:10.1118/1.4812422

A.1 Film processing

Each film was scanned four times both before and after radiation exposure. In order to reduce noise from a scanner warm-up effect, only the last three film scans were averaged for analysis.[1,2] To get dark field pixel values, an opaque sheet was scanned after each set of unexposed and exposed film scans. The corrected net optical density, using the blue channel to account for film thickness,[3] was calculated as:

$$\begin{aligned} \mathrm{netOD_{corr}} &= \frac{\mathrm{OD_{exp,red}} - \mathrm{OD_{unexp,red}}}{\mathrm{OD_{unexp,blue}}} \\ &= \frac{\log_{10}\left(\frac{\mathrm{PV_{unexp,red}} - \mathrm{PV_{0,unexp,red}}}{\mathrm{PV_{exp,red}} - \mathrm{PV_{0,exp,red}}}\right)}{\log_{10}\left(\frac{2^{16}}{\mathrm{PV_{unexp,blue}} - \mathrm{PV_{0,unexp,blue}}}\right)}, \end{aligned} \tag{A.1}$$

where $OD_{exp,red}$, $OD_{unexp,red}$, and $OD_{unexp,blue}$ are the OD measured in the red colour channel and blue colour channel of the exposed and unexposed film. PV values are scanner pixel values measured in the red and blue colour channel of exposed and unexposed film. PV_0s are opaque film pixel values for red and blue channels after scanning a set of unexposed films and a set of exposed films.

To convert netOD to dose, eight 70 mm × 70 mm calibration films were prepared and placed horizontally, at the isocenter of the micro-CT, between two 70 mm × 70 mm × 10 mm solid water phantom blocks. An additional 2 mm of solid water was placed on top of the stack. The jaws were set to give a 50 mm × 50 mm field size. The first films were exposed with 433 pulses, approximately equal to 0.5 Gy. Each consecutive film was exposed with an additional 433 pulses, compared to the previous one. This was repeated to give 8 total films, ranging in dose from 0.5 Gy to 8 Gy, in steps of 0.5 Gy. Each film was scanned as stated above, and the center 20 × 20 pixel region was averaged to give a single netOD value for each calibration film. Dose per pulse, calculated from ion chamber measurements of identical geometry, was used to calculate the dose given to each film. The dose as a function of netOD,[1,2]

$$D^{\text{fit}} = a + b \cdot \text{netOD} + c \cdot \text{netOD}^n, \tag{A.2}$$

was fitted using ordinary linear regression. Different n values between 2 and 3 were tried to find the best fit parameters.[1]

A setting of n = 2.4 resulted in the best fit of the calibration films. At n = 2.4, the three coefficients were found to be a = 0, b = 3.43 ± 0.07, and c = 6.1 ± 0.2. The calibration curve is shown in figure A.1.

We used the method described by Devic et al.[1,2] to calculate the film dose error from the spatial pixel variation of the film sampling area and the uncertainty in the calibration curve fit.

The equation,

$$\sigma_{D_{\text{tot}}}(\%) = \frac{\sqrt{\text{netOD}^2 \cdot \sigma_b^2 + \text{netOD}^{2n} \cdot \sigma_c^2 + (b + n \cdot c \cdot \text{netOD}^{n-1} \cdot \sigma_{\text{netOD}}^2)}}{D_{\text{fit}}} \times 100, \qquad \text{(A.3)}$$

is derived by propagating the standard deviation from averaging the three scans through equation A.1. We found this method did not account for inter-film variability. We estimated the inter-film variability by measuring the standard error of three measurements of each of the 50 $\times$ 50 mm^2 and 40 $\times$ 40 mm^2 fields. The composite error is computed by adding the intra-film ($\sigma_{D_{tot}}$) and inter-film error in quadrature. The estimate of the inter-film variability is about 3%, as determined by repeated measurements. The intra-film variability is about 2%, and varies for each digitized film pixel.

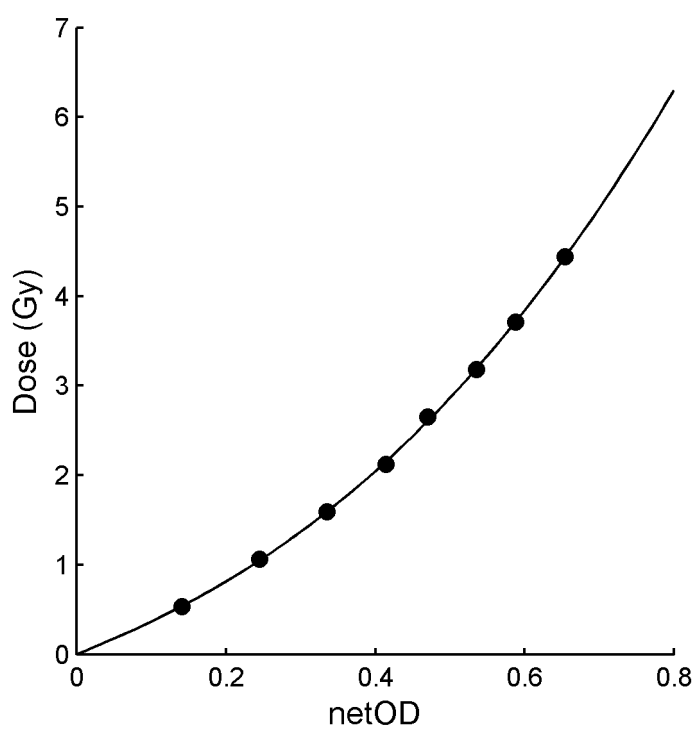

Figure A.1: EBT2 film calibration curve fit of film net optical density to dose. Size of marker indicates standard deviation of netOD values.

A.2 References

[1]S. Devic, J. Seuntjens, G. Hegyi, E. Podgorsak, C. Soares, A. Kirov, I. Ali, J. Williamson, and A. Elizondo, "Dosimetric properties of improved GafChromic films for seven different digitizers", Med. Phys. **31**, 2392–2401 (2004).

[2]S. Devic, J. Seuntjens, E. Sham, E. Podgorsak, C. Schmidtlein, A. Kirov, and C. Soares, "Precise radiochromic film dosimetry using a flat-bed document scanner", Med. Phys. **32**, 2245–2253 (2005).

[3]T. McCaw, J. Micka, and L. Dewerd, "Characterizing the marker-dye correction for Gafchromic EBT2 film: a comparison of three analysis methods", Med. Phys. **38**, 5771–5777 (2011).

Appendix B

Dual energy algorithms

This appendix briefly describes the previously published dual energy algorithms applied in chapters 3 and 4. The reader is encouraged to consult the primary references for a thorough description of the algorithms.

B.1 Theoretical effective atomic number

In chapter 3 the empirical power law effective atomic number (Z_{eff}) is defined as

$$Z_{eff} = \left(\sum_i a_i Z_i^n \right)^{\frac{1}{n}}, \tag{B.1}$$

where Z_i is the atomic number of the ith element in the mixture and a_i the fractional number of electrons belonging to the ith element in the mixture. The value for the parameter n was chosen as 3.5. This is the definition published by Johns and Cunningham.[1]

In chapter 4 we use the empirical effective atomic number (Z_{med}) as defined by Bourque et al..[2] Briefly, a lookup curve is constructed using the NIST XCOM database[3] to give the electron cross section for all the elements from the atomic number, averaged over a specific x-ray spectrum. Therefore the value of (Z_{med}) is dependent on the x-ray spectra. To find the effective atomic number (Z_{med}) of any material, one calculates the electron cross section of the material for the spectra of interest and uses the inverse of the atomic number to electron cross

section lookup curve function.

$$Z_{med} \equiv \hat{\sigma}_e^{-1}(\sigma_{e,med}) \tag{B.2}$$

B.2 Reduced Hounsfield unit

The Houndsfield unit is defined as

$$\mathrm{HU} = 1000\left(\frac{\mu}{\mu_w} - 1\right), \tag{B.3}$$

where μ is the linear attenuation coefficient of the material of interest, and μ_w the linear attenuation coefficient of water. The reduced Hounsfield unit is given by

$$\frac{\mu_j}{\mu_{jw}} = \frac{\mathrm{HU}_j}{1000} + 1, \tag{B.4}$$

where j indicates energy of the scan (low or high).

B.3 Spectral based DECT method

The image space spectrum method by Bazalova et. al was implemented.[4,5] This method was based on the work by Torikoshi et al. for monochromatic energy scans.[6] Additionally, the improvements by Landry et al. were implemented– specifically the calculation of the effective atomic number of water (Z_w) using the x-ray spectra and attenuation coefficient data..[7,8]

The linear attenuation coefficient μ_j, for an energy spectrum j, can be expressed as

$$\mu_j = \rho_e \sum_i \omega_{ji}[Z^4 F(E_{ji}, Z) + G(E_{ji}, Z)], \tag{B.5}$$

with ρ_e the electron density of the material, ω_{ji} the weight of energy i in the spectrum j, Z the effective atomic number and E_{ji} the photon energy.

The attenuation components are modelled with two empirically fit functions. The photoelectric component $\rho_e Z^4 F(E_{ji}, Z)$, and the combined coherent and incoherent component $\rho_e G(E_{ji}, Z)$. The functions $F(E, Z)$ and $G(E, Z)$ are produced by quadratic fits to the NIST XCOM database.[3] The effective atomic number (Z) of the material is found by solving

$$\begin{aligned} Z^4 - \Bigg\{ \Bigg(& \frac{\mu_2}{\mu_{2w}} \sum_i \omega_{2i} [Z_w^4 F(E_{2i}, Z_w) + G(E_{2i}, Z_w)] \sum_i \omega_{1i} G(E_{1i}, Z) \\ & - \frac{\mu_1}{\mu_{1w}} \sum_i \omega_{1i} [Z_w^4 F(E_{1i}, Z_w) + G(E_{1i}, Z_w)] \sum_i \omega_{2i} G(E_{2i}, Z) \Bigg) \Bigg/ \\ & \Bigg(\frac{\mu_1}{\mu_{1w}} \sum_i \omega_{1i} [Z_w^4 F(E_{1i}, Z_w) + F(E_{1i}, Z_w)] \sum_i \omega_{2i} F(E_{2i}, Z) \\ & - \frac{\mu_2}{\mu_{2w}} \sum_i \omega_{2i} [Z_w^4 F(E_{2i}, Z_w) + G(E_{2i}, Z_w)] \sum_i \omega_{1i} F(E_{1i}, Z) \Bigg) = 0 \end{aligned} \tag{B.6}$$

for each voxel. Equation B.6 was obtained by combining equations B.4 and B.5 at two energies. Using either the high or low energy scan (j = 1,2), the relative electron density is then calculated with

$$\rho_e / \rho_{e,w} = \frac{\mu_j}{\mu_{jw}} \frac{\sum_i \omega_{ji} [Z_w^4 F(E_{ji}, Z_w) + G(E_{ji}, Z_w)]}{\sum_i \omega_{ji} [Z^4 F(E_{ji}, Z) + G(E_{ji}, Z)]}. \tag{B.7}$$

For only in chapter 4, a linear correction was applied to the spectral method to reduce the error between measured effective atomic number (EAN) and theoretical Z_{med} values.

B.4 Empirical polynomial fit DECT method

We implemented the method published by Bourque et al.[2] Briefly, the dual energy ratio (DER) is computed for each voxel of the image pair. The dual energy ratio (Γ = DER) is defined as

$$\Gamma \equiv \frac{\mu_1}{\mu_2}, \tag{B.8}$$

with μ_1 and μ_2 the reduced Hounsfield units of the voxel pair from the low and high energy scans.

A polynomial is fit to relate the theoretical effective atomic number Z_{med} to the DER for all materials.

$$Z_{med} = \sum_{k=1}^{K} c_k \Gamma^{k-1} \tag{B.9}$$

Then another two polynomials, one for each energy scan, are fit to relate the theoretical relative electron density to the reduced HU and Z_{med}.

$$(\rho_e/\rho_{e,w})_j = \frac{\mu_j}{\sum_{m=1}^{M} b_{j,m} Z_{med}^{m-1}} \tag{B.10}$$

Both the high and low energy scans are used to compute two relative electron density maps which are equally weighted to create a final relative electron density map.

$$\rho_e/\rho_{e,w} = \frac{1}{2}\Big[(\rho_e\rho_{e,w})_1 + (\rho_e/\rho_{e,w})_2\Big] \tag{B.11}$$

B.5 References

[1]H. E. Johns and J. R. Cunningham, *The physics of radiology*, 4th ed. (Charles C Thomas, Springfield, IL, 1983), pp. 241–243.

[2]A. E. Bourque, J.-F. Carrier, and H. Bouchard, "A stoichiometric calibration method for dual energy computed tomography", Phys. Med. Biol. **59**, 2059–88 (2014).

[3]M. J. Berger, J. H. Hubbell, S. M. Seltzer, J. Chang, J. S. Coursey, R. Sukumar, D. S. Zucker, and K. Olsen, *XCOM: Photon Cross Section Database (Version 1.5)*, tech. rep. (National Institute of Standards and Technology, Gaithersburg, MD, 2010).

[4]M. Bazalova, J.-F. Carrier, L. Beaulieu, and F. Verhaegen, "Tissue segmentation in Monte Carlo treatment planning: a simulation study using dual-energy CT images", Radiother. Oncol. **86**, 93–98 (2008).

[5]M. Bazalova, J.-F. Carrier, L. Beaulieu, and F. Verhaegen, "Dual-energy CT-based material extraction for tissue segmentation in Monte Carlo dose calculations", Phys. Med. Biol. **53**, 2439–2456 (2008).

[6]M. Torikoshi, T. Tsunoo, M. Sasaki, M. Endo, Y. Noda, Y. Ohno, T. Kohno, K. Hyodo, K. Uesugi, and N. Yagi, "Electron density measurement with dual-energy x-ray CT using synchrotron radiation", Phys. Med. Biol. **48**, 673–85 (2003).

[7]G. Landry, P. V. Granton, B. Reniers, M. C. Ollers, L. Beaulieu, J. E. Wildberger, and F. Verhaegen, "Simulation study on potential accuracy gains from dual energy CT tissue segmentation for low-energy brachytherapy Monte Carlo dose calculations", Phys. Med. Biol. **56**, 6257–6278 (2011).

[8]G. Landry, B. Reniers, P. V. Granton, B. van Rooijen, L. Beaulieu, J. E. Wildberger, and F. Verhaegen, "Extracting atomic numbers and electron densities from a dual source dual energy CT scanner: experiments and a simulation model", Radiother. Oncol. **100**, 375–379 (2011).

Appendix C

Study of the IMRT interplay effect using 4DCT Monte Carlo dose calculation

This appendix is adapted from the research article "Study of the IMRT interplay effect using a 4DCT Monte Carlo dose calculation". Reprinted with permission from M. D. Jensen, A. Abdellatif, J. Chen and E. Wong, Physics in Medicine and Biology **57**, N89–99 (2012).

© 2012 Institute of Physics and Engineering in Medicine

doi: 10.1088/0031-9155/57/8/N89

C.1 Introduction

Respiratory motion has the potential to negatively impact radiation therapy treatments if the motion is not properly managed. This is especially true when more complex multileaf collimator (MLC) patterns are used, such as in integrated boosts with IMRT and VMAT, which are increasingly being deployed. These treatments can be susceptible to the interplay effect between motion of the anatomy from respiration and multileaf collimators. The interplay of the concurrent motion of the anatomy and multileaf collimator can lead to errors within the treatment field.[1–5]

Dose calculation with patient motion has previously been studied by Litzenberg et al.,[6] Oliver et al.,[7,8] and Waghorn et al.[9] using patient tracking information to move the beam isocentre relative to the patient to simulate motion. Litzenberg et al. used position information

from electromagnetically tracked implantable transponders, combined with a motion phantom, MLC controller log files and Monte Carlo dose calculation to investigate intra-fraction motion. Waghorn et al. modified the fluence maps in a treatment planning system by shifting them in the opposite direction of the patient motion, using respiratory traces. However, these previous studies did not employ four-dimensional computed tomography (4D CT).

With 4D CT, one allowed the possibility to incorporate tissue deformation into planning and simulation. One method of 4D dose calculation is to calculate the same plan on all phases of a 4D CT, and deform[10] back to a reference scan.[11,12] Flampouri et al.[13] and Huang T-C et al.[14] have combined this technique with Monte Carlo dose computations. However, this approach does not permit accounting for interplay effects, and assumes the motion effects will uniformly smear out over the course of many treatments.[3,5,15]

Several publications have used linear accelerator (linac) and multileaf collimator controller log files to recreate volumetric modulated arc therapy (VMAT) deliveries. Schreibmann et al.[16] and Haga et al.[17] used the log files to modify the original treatment plan, so that the verification dose calculation can be done in the original treatment planning system. Qian et al.[18] used a similar technique and combined it with cone-beam CT. Qian et al.[19] subsequently extended this technique to use the TrueBeam (Varian Medical Systems, Palo Alto, CA USA) system trajectory log files to add respiratory motion data to verify respiratory gated VMAT. Teke et al.[20] has combined log files with a Monte Carlo dose engine as a basis for a patient-specific VMAT QA system.

These previous studies have made use of selected data sources and techniques, such as linac log files, respiratory trace log files, 4D CT, and Monte Carlo dose engines in their dose computations. To the authors' knowledge, no previous studies combine all these data sources and techniques to build a delivery reconstruction simulator. By using motion data of both the patient and the linac recorded during treatment and performing Monte Carlo dose computations on 4D CT, we can simulate the delivered dose with less assumptions regarding machine performance or patient breathing and be able to examine the impact of making various simplifications.

In this paper, we extend the isocentre shifting method[7,8] to utilize 4D CT in addition to the linac log files and respiratory motion tracking information to reconstruct the dose delivered to a rigid phantom from a 3D step-and-shoot IMRT plan. Many publications have included deformable registration to warp the doses back to a base phase scan.[11–14,21] In this study, we have purposely omitted patient/phantom deformation to examine dose computations alone, without effects confounded by deformable dose warping. This approach cleanly separates 4DCT dose simulation and deformable registration, allowing independent verification, and integration in the future.

C.2 Methods

We began with a 3D step-and-shoot IMRT plan registered to one phase of a 4D CT. The plan was then delivered to a phantom, and the linac and respiratory log files were collected. Respiratory motion was initially modeled by moving the plan isocentre on the one phase of the 4D CT using the respiratory log file. This isocentre shifting method was previously validated with measurements.[7,8] To extend the method to 4DCT dose calculation, we replace the isocentre shift by picking the phase of 4D CT corresponding to the respiratory motion. Dose was computed using a Monte Carlo method with MLC positions during the delivery determined by the linac log files. The doses to the different respiratory phases were combined to give a total dose distribution.

First, we compared our 4DCT method to the isocentre shifting rigid phantom method, previously validated against measurements.[7,8] Secondly, we investigated the effect of the limited sampling of motion in 4DCT. The isocentre shifting method can finely sample the phantom motion, and the result is limited by the dose calculation grid resolution. However, 4D CT effectively limits the motion sampling to 10 positions. Thirdly, we examined two gating cases, which further reduce the sampled positions from 4D CT. Finally, we compared our time explicit motion simulations with time and position weighted average 4D dose calculations, using

either parameters from the linac log file or DICOM RT plan. The purpose of these comparisons is to find out the limitations of various approximations in 4D dose calculations, especially time and position averaged 4D-dose calculation methods available in some commercial treatment planning systems.

A respiratory motion phantom was scanned using 4D CT, and two step-and-shoot 3D IMRT plans were transferred to the CT images at the end-of-expiration (EOE) phase. The 3D IMRT plans were delivered to the moving phantom, both with and without gating. The respiratory trace and linac/MLC controller log files were collected from the deliveries of the 3D IMRT plans. The log files were synchronized in time and combined with the 4D CT to reconstruct the delivered dose using a Monte Carlo dose calculation engine.[22] This simulation reconstructs the time series of events during the treatment. Three methods of motion reconstruction were used: continuous shifting of the beam isocentre on the EOE phase, discrete shifting of the beam isocentre on the EOE phase and using the full 4D CT. These methods are named continuous isocentre shift, discrete isocentre shift and 4DCT. The 4DCT method is illustrated in figure C.1. Additionally, two simulations without the explicit time series of events were completed. Both methods simulate the full delivery of the 3D IMRT plan on each of the ten phases of the 4D CT; dose to each phase is weighted by 10% and they are added together to get a time and position averaged total dose. The difference between the two methods is that the first uses the linac log file for MLC positions and segment weights, while the second uses the MLC and segment weights from the RT plan file. These two methods are referred to as 4DCT Delivery Average and 4DCT Plan Average. All simulation methods were compared against the gold standard continuous isocentre shift method.

C.2.1 Phantom, contours, IMRT plan and 4DCT acquisition

A rigid respiratory motion phantom (QUASAR Respiratory Motion Phantom, Modus Medical Devices Inc., London, ON Canada) (figure C.2) was imaged using the 4D Thorax protocol on a Brilliance CT Big Bore Oncology scanner (Philips Healthcare, Andover, MA USA) equipped

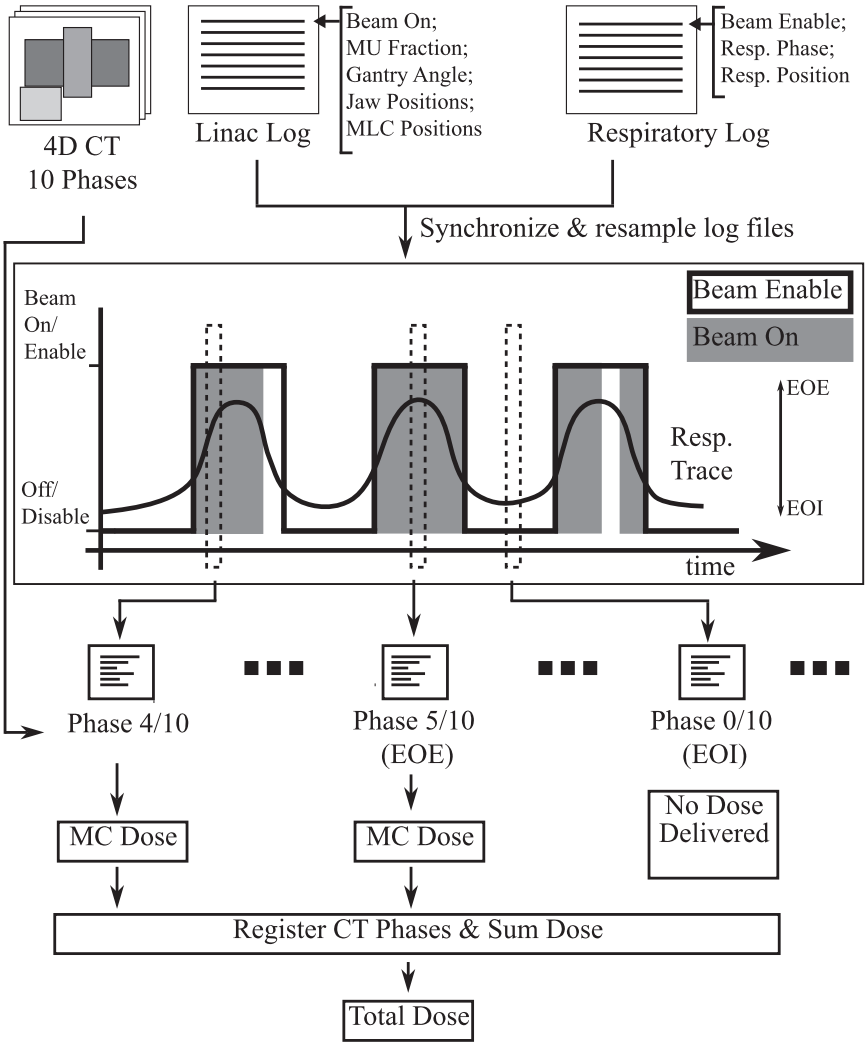

Figure C.1: Overview of the 4D CT with respiratory and MLC position data simulation. Gated delivery is shown. Linac and respiration log files are synchronized in time using the beam on and beam enable flags. The delivery is then divided into 400 ms samples (dashed boxes), containing linac state and patient respiratory information. Each of the samples is matched with the appropriate 4DCT phase image using the patient respiration phase information. Each time sample containing delivered MU is then simulated using the Monte Carlo dose computation. The series of dose matrices are then registered back to the base phase of the 4DCT scan, and summed to obtain the total dose. Areas of the beam enable/beam on graph where the gating window is open but no MU are delivered, are locations where the leaves are repositioning for the next IMRT segment.

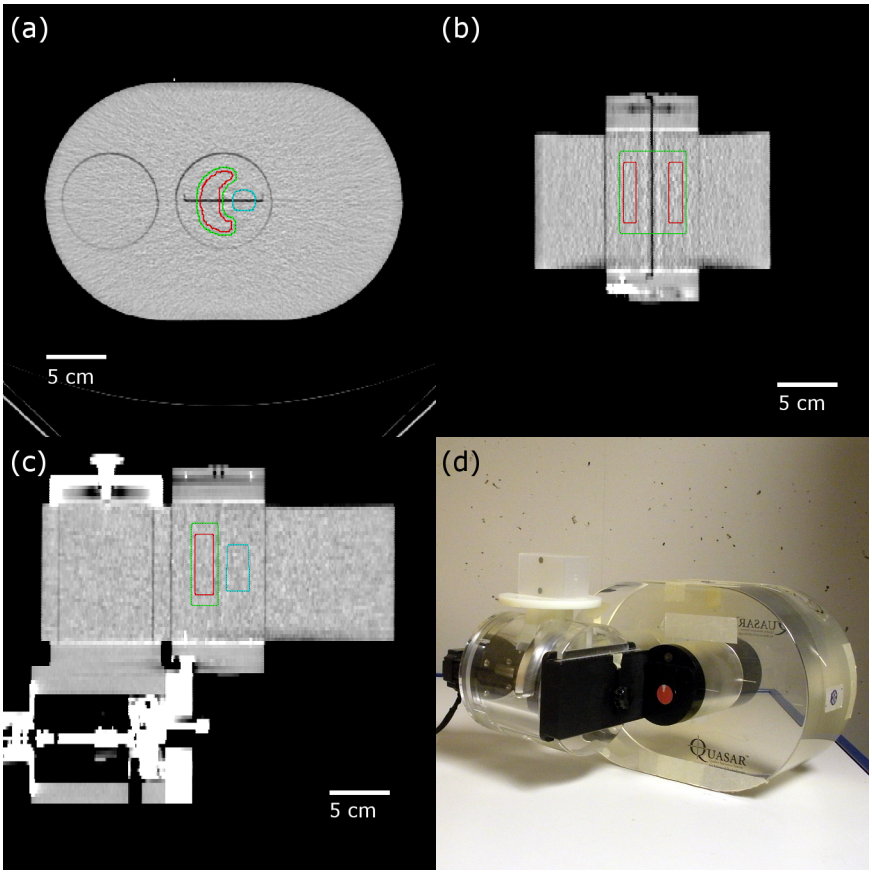

Figure C.2: End of Inhale (EOI) CT scan of 1D motion phantom in axial (a), sagittal (b) and coronal (c) view with contours for the concave target. Photograph of 1D motion phantom (d).

with a respiratory position management system (Varian Medical Systems, Palo Alto, CA USA). The thorax protocol produces 10 image sets equally spaced throughout the respiratory cycle. The phantom was programmed to move with regular sinusoidal motion, with amplitude of 2 cm (peak to peak) and period of 4 seconds. Two 3D IMRT step-and-shoot plans, the first for a concave target,[7,8] and the second a integrated boost plan (to fit into the moving part of the phantom, we used a prostate plan with a dominant intra-prostatic legion boost), were copied to the 4D CT end-of-expiration (EOE) scan using a treatment planning system (Pinnacle[3] v8.0m Philips Medical Systems, Fitsburg, WI, USA). The first concave target plan consisted of 5 beams using step-and-shoot delivery with 30 segments and 592 MU. The second integrated boost plan had 5 beams using step-and-shoot delivery with 50 segments and 553 MU.

C.2.2 Delivery of treatment

The IMRT plans were delivered to the respiratory phantom as described by Oliver et al.[8] The treatments were delivered using a linear accelerator (Clinac 21EX, Varian Medical Systems, Palo Alto CA USA) configured with a 120 leaf MLC and real time position (RPM) monitoring system. Each plan was delivered three times; no gating, 50% duty cycle gating and 25% duty cycle gating. There was no attempt to synchronize the start of the treatment with the respiratory motion for the ungated delivery.

C.2.3 Simulation of treatment

Five simulation types were performed in this work. The first three methods, continuous isocentre shift; discrete isocentre shift and 4DCT (figure C.1), reconstruct the delivery with explicit simulation of the motion of the phantom and linear accelerator in time. The log files from the experimental delivery were combined with the 4DCT scan to reconstruct the treatment time course in discrete time samples. These time samples were fed into a Monte Carlo dose calculation engine, and the resulting dose matrices summed. The last two methods, 4DCT plan average using planning segment weights and MLC positions and 4DCT delivery average using dynamic MLC log (dynalog) files for delivered segment weights and MLC positions, simulate the full delivery to each of the 10 phases of the 4D CT and produce a time and position averaged dose.

C.2.3.1 Log file processing

The IMRT delivery produces two dynamic MLC log files sampled at a frequency of 50 ms that record the motion of both leaf banks, the running fraction of MU output, and the beam on status. The RPM system logs the relative position of the IR reflector box, as well as beam-enable flags and current phase of the motion with a frequency of 33 ms.

Log file processing was performed with custom written software developed in MATLAB (The Mathworks Inc, Natick, MA, USA). The log files were synchronized in time by matching the beam on and beam enable flags (figure C.1). The logs were then divided into time step samples of 400 ms or less to be used for Monte Carlo dose calculations. Each Monte Carlo time sample contains the MU delivered, the positions of the leaves and jaws, the position of the phantom IR reflector and the current phase state of the phantom. A Monte Carlo time sample will be less than 400 ms, if the MUs for that segment have all been delivered before the end of a 400 ms time sample, or if a gating beam hold occurs within a 400 ms time sample. The Monte Carlo time sample phantom position is the average position during the time sample, while the Monte Carlo time sample phantom phase is the phase sampled at the middle of the time sample.

C.2.3.2 4DCT image phases

The RPM phase recorded in the Monte Carlo time sample was used to select the appropriate phase of the 4DCT for the dose calculation.

The 10 phases of the 4D CT were registered to each other by plotting a CT number profile though the moving cylinder. The position of the full width at half max for each profile was used to calculate the superior-inferior offset for each of the phases relative to a base phase. These offsets were used to combine the 10 dose grids corresponding to the 10 respiratory phases without the need of deformable registration software. Additionally, these offsets were used to perform the discrete isocentre shift calculation.

C.2.3.3 Monte Carlo dose calculations

The dose for each time sample was calculated using a fast Monte Carlo method (Numerix v1.12, Numerix LLC, New York, NY, USA) with 3 mm isotropic dose grid.[22] Each time sample simulation used 100,000 photon histories, with variance reduction performed on each sample.

C.2.4 Analysis

The image and dose data was visualized in the Computational Environment for Radiotherapy Research (CERR).[23] A dose region measuring 6.0 × 6.0 × 13.8 cm from the center of the moving portion of the phantom was used to compare six calculation methods. The gamma method,[24,25] extended to 3 dimensions, was used with agreement criteria of 2%, 2 mm. The dose distributions were interpolated to 0.2 mm isotropic resolution for the gamma analysis. The discrete isocentre shift, 4DCT, 4DCT delivery average and 4DCT plan average dose distributions were compared against the gold standard continuous isocentre shift method.

Gamma analysis is a well known metric to quantify the dose distribution differences and was chosen to compare the calculation methods. While gamma analysis has been recently criticized as a clinical QA tool,[10,26,27] we feel it appropriately meets the needs of this study.

C.3 Results

Coronal dose distributions, dose difference, and 3D gamma map planes for the concave target and integrated boost plan for the five simulation methods of the ungated motion cases are shown in figures C.3 and C.4. Table C.1 shows the 3D gamma analysis passing percentages and mean gamma values for all the simulations compared to the gold standard continuous isocentre shift method. The 3D gamma passing percentage analysis indicates that the discrete isocentre shift and 4DCT methods of simulation are equivalent to the previously validated continuous isocentre shift method, with greater than 99% of points passing the 2% 2 mm gamma threshold for both plans and for all gating conditions. For the time and position averaged simulations, the results are plan and gating dependent. The plan with concave target showed negligible disagreement with the gold standard continuous isocentre shift method. However, the integrated boost plan only had an 80% passing percentage for the 4DCT delivery and plan averaged simulations at 2%, 2 mm. Relaxing the gamma pass criteria to 3%, 3 mm improved the passing percentage to 93.6% for the 4DCT delivery average simulation, and 93.1% for the 4DCT plan

		Integrated boost plan		Concave target plan	
Gating	Simulation type	Pass per cent	Mean gamma	Pass per cent	Mean gamma
No gating	Discrete isocentre shift	100	0.19	100	0.17
	4DCT	100	0.20	100	0.18
	4DCT delivery average	80.7	0.54	99.2	0.23
	4DCT plan average	80.3	0.54	98.4	0.25
Gating 50%	Discrete isocentre shift	100	0.20	100	0.18
	4DCT	100	0.19	99.9	0.19
	4DCT delivery average	100	0.13	100	0.26
	4DCT plan average	99.4	0.21	99.7	0.28
Gating 25%	Discrete isocentre shift	100	0.12	100	0.11
	4DCT	100	0.11	100	0.13
	4DCT delivery average	100	0.12	100	0.11
	4DCT plan average	99.8	0.19	100	0.16

Table C.1: 3D Gamma analysis (2%, 2 mm) comparing 4D methods to gold standard continuous isocentre shift method.

average simulation. When gating was applied, this disagreement disappeared for the integrated boost plan, indicating gating reduced IMRT interplay effects significantly. The difference in gamma for the time and position average simulation doses, between the planned and actual leaf positions and segment weights, was less than 1% for all cases examined.

C.4 Discussion

Our study demonstrated that our 4DCT simulation using delivery log files is consistent with our previously validated isocentre shift method for the two cases examined with rigid 1D motion. Constraining the isocentre to ten positions of 4D CT did not noticeably impact the dose for the two cases examined.

This study showed the IMRT interplay effect can be significant for a single fraction of a 3D step-and-shoot IMRT plan. However, this is plan dependent, as the integrated boost plan was more sensitive to time averaging than the concave target plan. This work did not examine the effect of multiple fractions, and if a series of repeated time explicit simulations would converge

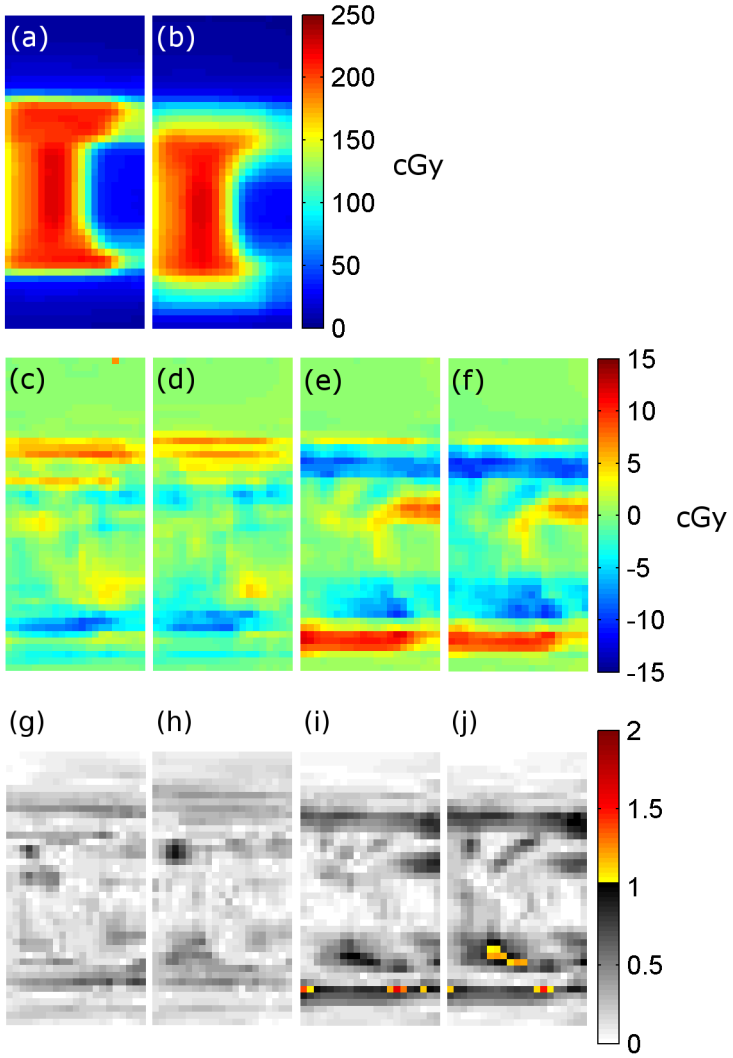

Figure C.3: Coronal plane dose distributions for the concave target plan: a) no motion and b) continuous isocentre shift. Coronal plane dose difference between: c) discrete isocentre shift; d) 4DCT; e) 4DCT delivery average; f) 4DCT plan average; and continuous isocentre shift. Coronal plane of 3D gamma map (2%, 2 mm) between: g) discrete isocentre shift; h) 4DCT; i) 4DCT delivery average; j) 4DCT plan average; and continuous isocentre shift.

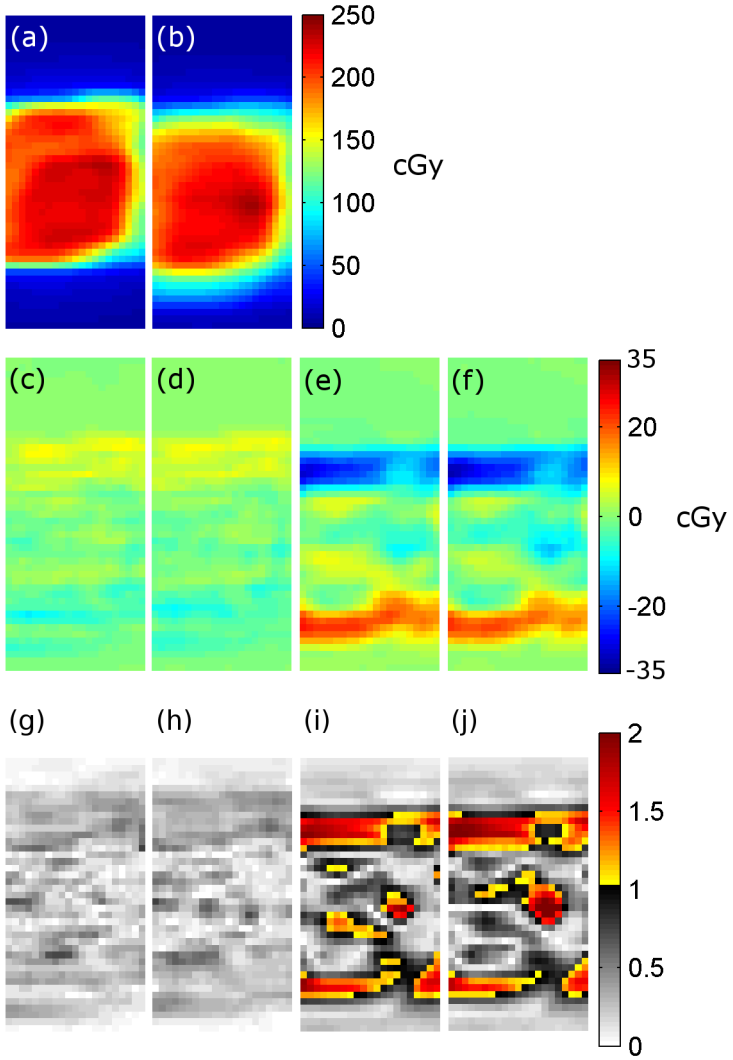

Figure C.4: Coronal plane dose distributions for the integrated boost plan: a) no motion and b) continuous isocentre shift. Coronal plane dose difference between: c) discrete isocentre shift; d) 4DCT; e) 4DCT delivery average; f) 4DCT plan average; and continuous isocentre shift. Coronal plane of 3D gamma map (2%, 2 mm) between: g) discrete isocentre shift; h) 4DCT; i) 4DCT delivery average; j) 4DCT plan average; and continuous isocentre shift.

to the time and position averaged simulation. Both a 50% and 25% gating window strongly reduced the interplay effect for the integrated boost plan.

This work only examined simplistic one-dimensional, rigid, sinusoidal motion. The results of this study cannot be blindly generalized to three-dimensional, deforming, and irregular motion. However, the 1D motion is a subset of 3D motion, and may be a reasonable approximation of some patients. With more complex motion, there is both the possibility of increased or suppressed interplay effects, and more study is needed. This simulation framework is not inherently restricted to one-dimensional motion. The addition of an advanced motion phantom and deformable registration to our simulation framework would allow the study of more complex motion.

This work illustrates how one may investigate the impact of different assumptions - with and without log files, using the same plan on all phases of 4DCT, etc. It demonstrated that our simulation framework is a useful tool to further study motion related effects. Combined with deformable registration, this technique could be used to reconstruct the dose delivered to patients.

The mean gamma was reported to give a metric of where the bulk of the gamma value population lies, and the proximity to the pass threshold. The mean gamma can differentiate the 100% passing rates of the 50% and 25% duty cycle gating simulations. Reducing the gating duty cycle from 50% to 25% resulted in approximately a 50% reduction in the mean gamma. Gamma analysis has come under scrutiny as a metric for examining the clinical impact of dose distribution changes.[10,26,27] However, in this work, we are using the gamma technique to only quantify the change in the dose distribution for different simulation techniques. We are not suggesting these results should be applied to clinical practice

C.5 Conclusion

We have developed a 4DCT Monte Carlo simulation method to account for IMRT interplay effects with respiratory motion. The method is consistent with our previously validated isocentre shift simulation work. Using linac log files, real-time position management log files and 4D CT, we showed that the IMRT interplay effect caused a single fraction dose to differ from the time and position averaged dose for a 3D IMRT integrated boost plan. This work provides a tool for studying the IMRT interplay effect.

C.6 References

[1]R. Berbeco, C. Pope, and S. Jiang, "Measurement of the interplay effect in lung IMRT treatment using EDR2 films", J. Appl. Clin. Med. Phys. **7**, 33–42 (2006).

[2]T. Bortfeld, S. Jiang, and E. Rietzel, "Effects of motion on the total dose distribution", Semin. Radiat. Oncol. **14**, 41–51 (2004).

[3]T. Bortfeld, K. Jokivarsi, M. Goitein, J. Kung, and S. Jiang, "Effects of intra-fraction motion on IMRT dose delivery: statistical analysis and simulation", Phys. Med. Biol. **47**, 2203–2220 (2002).

[4]L. Court, M. Wagar, D. Ionascu, R. Berbeco, and L. Chin, "Management of the interplay effect when using dynamic MLC sequences to treat moving targets", Med. Phys. **35**, 1926–1931 (2008).

[5]C. Yu, D. Jaffray, and J. Wong, "The effects of intra-fraction organ motion on the delivery of dynamic intensity modulation", Phys. Med. Biol. **43**, 91–104 (1998).

[6]D. Litzenberg, S. Hadley, N. Tyagi, J. Balter, R. Ten Haken, and I. Chetty, "Synchronized dynamic dose reconstruction", Med. Phys. **34**, 91–102 (2007).

[7]M. Oliver, A. Gladwish, R. Staruch, J. Craig, S. Gaede, J. Chen, and E. Wong, "Experimental measurements and Monte Carlo simulations for dosimetric evaluations of intrafraction motion for gated and ungated intensity modulated arc therapy deliveries", Phys. Med. Biol. **53**, 6419–6436 (2008).

[8]M. Oliver, R. Staruch, A. Gladwish, J. Craig, J. Chen, and E. Wong, "Monte Carlo dose calculation of segmental IMRT delivery to a moving phantom using dynamic MLC and gating log files.", Phys. Med. Biol. **53**, N187–196 (2008).

[9]B. Waghorn, A. Shah, W. Ngwa, S. Meeks, J. Moore, J. Siebers, and K. Langen, "A computational method for estimating the dosimetric effect of intra-fraction motion on step-and-shoot IMRT and compensator plans", Phys. Med. Biol. **55**, 4187–4202 (2010).

[10]J. Kruse, "On the insensitivity of single field planar dosimetry to IMRT inaccuracies", Med. Phys. **37**, 2516–2524 (2010).

[11]E. Ehler and W. Tomé, "Lung 4D-IMRT treatment planning: an evaluation of three methods applied to four-dimensional data sets", Radiother. Oncol. **88**, 319–325 (2008).

[12]Y. Vinogradskiy, P. Balter, D. Followill, P. Alvarez, R. White, and G. Starkschall, "Verification of four-dimensional photon dose calculations", Med. Phys. **36**, 3438–3447 (2009).

[13]S. Flampouri, S. Jiang, G. Sharp, J. Wolfgang, A. Patel, and N. Choi, "Estimation of the delivered patient dose in lung IMRT treatment based on deformable registration of 4D-CT data and Monte Carlo simulations", Phys. Med. Biol. **51**, 2763–2779 (2006).

[14]T.-C. Huang, J.-A. Liang, T. Dilling, T.-H. Wu, and G. Zhang, "Four-dimensional dosimetry validation and study in lung radiotherapy using deformable image registration and Monte Carlo techniques", Radiat. Oncol. **5**, 45 (2010).

[15]P. Keall, G. Mageras, J. Balter, R. Emery, K. Forster, S. Jiang, J. Kapatoes, D. Low, M. Murphy, B. Murray, C. Ramsey, M. Van Herk, S. Vedam, J. Wong, and E. Yorke, "The management of respiratory motion in radiation oncology report of AAPM Task Group 76", Med. Phys. **33**, 3874–3900 (2006).

[16]E. Schreibmann, A. Dhabaan, E. Elder, and T. Fox, "Patient-specific quality assurance method for VMAT treatment delivery", Med. Phys. **36**, 4530–4535 (2009).

[17]A. Haga, K. Nakagawa, K. Shiraishi, S. Itoh, A. Terahara, H. Yamashita, K. Ohtomo, S. Saegusa, T. Imae, K. Yoda, and R. Pellegrini, "Quality assurance of volumetric modulated arc therapy using Elekta Synergy", Acta. Oncol. **48**, 1193–1197 (2009).

[18]J. Qian, L. Lee, W. Liu, K. Chu, E. Mok, G. Luxton, Q.-T. Le, and L. Xing, "Dose reconstruction for volumetric modulated arc therapy (VMAT) using cone-beam CT and dynamic log files", Phys. Med. Biol. **55**, 3597–3610 (2010).

[19]J. Qian, L. Xing, W. Liu, and G. Luxton, "Dose verification for respiratory-gated volumetric modulated arc therapy", Phys. Med. Biol. **56**, 4827–4838 (2011).

[20]T. Teke, A. Bergman, W. Kwa, B. Gill, C. Duzenli, and I. Popescu, "Monte Carlo based, patient-specific RapidArc QA using linac log files", Med. Phys. **37**, 116–123 (2010).

[21]B. Guo, X. George Xu, and C. Shi, "Real time 4D IMRT treatment planning based on a dynamic virtual patient model: proof of concept", Med. Phys. **38**, 2639–2650 (2011).

[22]J. Craig, M. Oliver, A. Gladwish, M. Mulligan, J. Chen, and E. Wong, "Commissioning a fast Monte Carlo dose calculation algorithm for lung cancer treatment planning.", J. Appl. Clin. Med. Phys. **9**, 2702 (2008).

[23]J. Deasy, A. Blanco, and V. Clark, "CERR: a computational environment for radiotherapy research", Med. Phys. **30**, 979–985 (2003).

[24]D. Low, W. Harms, S. Mutic, and J. Purdy, "A technique for the quantitative evaluation of dose distributions", Med. Phys. **25**, 656–661 (1998).

[25]D. Low and J. Dempsey, "Evaluation of the gamma dose distribution comparison method", Med. Phys. **30**, 2455–2464 (2003).

[26]B. Nelms, H. Zhen, and W. Tomé, "Per-beam, planar IMRT QA passing rates do not predict clinically relevant patient dose errors", Med. Phys. **38**, 1037–1044 (2011).

[27]B. Waghorn, S. Meeks, and K. Langen, "Analyzing the impact of intrafraction motion: correlation of different dose metrics with changes in target $D_{95\%}$", Med. Phys. **38**, 4505–4511 (2011).

Appendix D

Permission to Reproduce Previously Published Materials

This thesis contains material from manuscripts that were previously published. The copyright(s) agreements for these publications are provided in this appendix.

ECopyright Form

Journal : Medical Physics
Manuscript # : 12-1590
Title : Implementation and commissioning of an integrated micro-CT/RT system with computerized independent jaw collimation
Authors : Michael Jensen, W. Hrinivich, Jongho Jung, David Holdsworth, Maria Drangova, Jeff Chen, and Eugene Wong
Agreement Date : October 20, 2012 1:30 GMT

Please read the Medical Physics Transfer of Copyright Agreement, select a copyright type and enter the name in the text box below to indicate your consent to that Agreement.

MEDICAL PHYSICS TRANSFER OF COPYRIGHT AGREEMENT

Copyright to the above-listed unpublished and original article and subsequent, if necessary, errata, and the abstract forming part thereof, submitted by the above author(s) (collectively, the "Article"), is hereby transferred to the American Association of Physicists in Medicine (AAPM) for the full term thereof throughout the world, subject to the Author Rights (as hereinafter defined) and to acceptance of the Article for publication in a journal of AAPM. This transfer of copyright includes all material to be published as part of the Article (in any medium), including but not limited to tables, figures, graphs, movies, and other multimedia files. AAPM shall have the right to register copyright to the Article in its name as claimant, whether separately or as part of the journal issue or other medium in which the Article is included.

The author(s), and in the case of a Work Made For Hire, as defined in the U.S. Copyright Act, 17 U.S.C. Â§ 101, the employer named below, shall have the following rights (the "Author Rights"):

1. All proprietary rights other than copyright, such as patent rights.

2. The nonexclusive right, after publication by AIP, to give permission to third parties to republish the Article or a translation thereof, or excerpts therefrom, without obtaining permission from AIP, provided the AIP-formatted version is not used for this purpose and provided the Article is not to be published in another conference proceedings or journal. If the AIP version is used, permission from AIP must be obtained.

3. The right, after publication by AIP, to use all or part of the Article without revision or modification, including the AIP-formatted version, in compilations or other publications of the author(s)' and/or the employer's own works, including the author(s)' and/or the employer's web home page, and to make copies of all or part of the Article for the author(s)' and/or the employer's use for lecture or classroom purposes.

4. The right to post and update the Article on e-print servers as long as files prepared and/or formatted by AIP or its vendors are not used for that purpose. Any such posting made or updated after acceptance of the Article for publication shall include a link to the online abstract in the AIP online article collection of the proceedings volume or to the proceedings volume home page.

5. If the Article was prepared under a U.S. Government contract, the government shall have the rights under the copyright to the extent required by the contract.

All copies of the Article made under any of the Author Rights shall include notice of the AIP copyright.

By signing this Agreement, the author(s), and in the case of a Work Made For Hire, the employer, jointly and severally represent and warrant that the Article is original with the author(s) and does not infringe any copyright or violate any other right of any third parties, and that the Article has not been published elsewhere, and is not being considered for publication elsewhere in any form, except as provided herein. If each author's signature does not appear below, the signing author(s) represent that they sign this Agreement as authorized agents for and on behalf of all the authors, and that this Agreement and authorization is made on behalf of all the authors. The signing author(s) (and, in the case of a Work Made For Hire, the signing employer) also represent and warrant that they have the full power to enter into this Agreement and to make the grants

contained herein. The Author agrees to indemnify and hold harmless AAPM from any loss, cost, damage or expense that may arise as a result of any breach of the representations or warranties set forth above

Please click to see the list of Government Institutions

Authors should select one of the following choices below:

◉ **Regular** - I represent and warrant that I am (i) the sole author; (ii) the authorized agent to sign on behalf of all of the authors; (iii) the authorized agent to sign on behalf of the commissioning person or organization: or (iv) the authorized agent to s ign on behalf of my employer;

○ **U.S. Government** - I represent and warrant that all the author(s) prepared this work as part of official duties with the U.S . Government and therefore the work is not subject to copyright;

○ **U.S. Government-funded** - I represent and warrant that this work was prepared in the scope of my employment at a laboratory that receives U.S. Government funding and that I am an authorized agent to sign on behalf of my employer;

○ **United Kingdom Crown Copyright** - The work is subject to Crown Copyright. I am submitting a license agreement for AIPs execution (To be uploaded as an Alternate Copyright Form during Submission or Revision Stages Only) ;

○ **Canadian Crown Copyright** - The work is subject to Crown Copyright. I represent and warrant that I have received authorization to publish the work from the Crown Copyright and Licensing Section of Government of Canada Publishing. I am submitting a license agreement for AIPs execution (To be uploaded as an Alternate Copyright Form during Submission or Revision stages only);

○ **Australian Crown Copyright** - The work is subject to Crown Copyright. I represent and warrant that I have received authorization to publish the work from the Australian Commonwealth Department or other agency responsible for the work. I am submitting a license agreement for AIPs execution. (To be uploaded as an Alternate Copyright Form during Submission or Revision Stages Only);

○ **Euratom** Agreement (For use by The European Atomic Energy Community organizations)`

☐ **Addendum or Alternate Copyright Form is being submitted.**

Acting in the above capacity, you agree that in consideration of acceptance of the work for publication, you do hereby assign and transfer to the American Institute of Physics all the rights and interest in and to the copyright rights of the electronically attached/submitted work as specified in the AIP Transfer of Copyright Agreement above, which you have read.

Please type your First and Last Name in the box to indicate your consent to the agreement Michael Jensen

Failure to provide assent to the Transfer of Copyright Agreement or to provide an appropriate form will mean that the American Institute of Physics will be unable to publish your paper. Send requests for further information to the Office of Rights and Permissions, American Institute of Physics, Suite 1NO1,2 Huntington Quadrangle, Melville, NY 11747- 4502, USA; Phone: 516-576-2268; Fax: 516-576-2450; Email: rights@aip.org.

Please review your selection and make any changes, if necessary, before acceptance.

☑ **I accept this form**

local_p_id: 103630

Ref: : PMB/414991/NOT/278731

Assignment of copyright - Institute of Physics and Engineering in Medicine

1. IOP Publishing Limited ("IOP") agrees, on behalf of the Institute of Physics and Engineering in Medicine ("IPEM"), to publish:

Manuscript Title: Study of the IMRT interplay effect using 4DCT Monte Carlo dose calculation ("**the Article**") written by

Names of all Authors: Michael Jensen, Ady Abdellatif, Jeff Chen, Eugene Wong ("**the Named Authors**") in the following journal Physics in Medicine and Biology ("**the Journal**")

2. Transfer of Copyright Agreement

2.1 On acceptance for publication the undersigned author(s) ("Author") of the Article assigns exclusively to IPEM the entire worldwide copyright in the Article (whether vested, contingent or future) for the full term and for all media and formats in all material published as part of the Article, which expression includes but is not limited to the text, abstract, tables, figures and graphs, but excludes any supplementary material.

2.2 If any of the Named Authors are Government employees, on acceptance for publication the Author shall grant IPEM a royalty free exclusive licence for the full term of copyright for all media and formats to do in relation to the Article all acts restricted by copyright worldwide.

2.3 On acceptance for publication the Author shall grant IPEM a royalty free non-exclusive licence for the full term of copyright for all media and formats to do in relation to any supplementary material deemed to be part the Article all acts restricted by copyright worldwide.

3. Author Rights

3.1 IPEM grants the Named Authors the rights specified in 3.2 and 3.3. All such rights must be exercised for non-commercial purposes, if possible should display citation information and IPEM's copyright notice, and for electronic use best efforts must be made to include a link to the on-line abstract in the Journal. Exercise of the rights in 3.3 additionally must not use the final published IOP format but the Named Author's own format (which may include amendments made following peer review).

3.2 The rights are:

3.2.1 To make copies of the Article (all or part) for teaching purposes;

3.2.2 To include the Article (all or part) in a research thesis or dissertation;

3.2.3 To make oral presentation of the Article (all or part) and to include a summary and/or highlights of it in papers distributed at such presentations or in conference proceedings; and

3.2.4 All proprietary rights other than copyright.

3.3 The additional rights are to:

3.3.1 Use the Article (all or part) without modification in personal compilations or publications of a Named Author's own works (provided not created by third party publisher);

3.3.2 Include the Article (all or part) on a Named Author's own personal web site;

3.3.3 Include the Article (all or part) on web sites of the Institution (including its repository) where a Named Author worked when research for the Article was carried out; and

3.3.4 No sooner than 12 months after publication to include the Article (all or part) on third party web sites including e-print servers, but not on other publisher's web sites.

Signature

In signing this Agreement the Author represents and warrants that the Article is the original work of the Named Authors, it has not been published previously in any form (other than as permitted under clause 3.2.2 which fact has been notified to IOP in writing), all Named Authors have participated sufficiently in the conception and writing of the Article, have received the final version of the Article, agree to its submission and take responsibility for it, and submission has been approved as necessary by the authorities at the establishment where the research was carried out.

The Author warrants that he/she signs this Agreement as authorised agent for all Named Authors and has the full power to enter into this Agreement and to make the grants it contains, that the Article has not been and will not be submitted to another publisher prior to withdrawal or rejection, it does not infringe any third party rights, it contains nothing libellous or unlawful, all factual statements are to the best of the Author's knowledge true or based on valid research conducted according to accepted norms, and all required permissions have been obtained in writing.

The Author acknowledges on behalf of all Named Authors that IOP as publisher may enforce the terms and conditions of this Agreement against the Named Authors.

All Named Authors assert their moral rights.

Author's signature.....[redacted].....**Date**...Feb. 27, 2012

Signature on behalf of Institution.....[redacted].....**Date**..Feb. 27, 2012

Note that if the Article was prepared as part of a Named Author's duties for their institution this Agreement must be signed by their institution as Author. Further, if there are several Named Authors it should be signed by one author in a representative capacity. If all Named Authors are employees of the US Government and the Article was prepared as part of their duties the Article is not eligible for copyright and one of the Named Authors should sign below to confirm this fact. If at least one of the Named Authors is not a US Government employee the above should be signed.

I ..... (print name.....) confirm that a Named Authors are employees of the US Government and the Article was prepared as part of their dutie and consequently the Article is not eligible for copyright.

Please return ALL of this form as soon as possible to IOP Publishing Ltd, Temple Circus, Temple Way, BRISTOL 6BE, UK. (Journal fax: +44 (0) 117 9200677)

ELSEVIER LICENSE
TERMS AND CONDITIONS

Jun 19, 2015

This is a License Agreement between Michael D Jensen ("You") and Elsevier ("Elsevier") provided by Copyright Clearance Center ("CCC"). The license consists of your order details, the terms and conditions provided by Elsevier, and the payment terms and conditions.

All payments must be made in full to CCC. For payment instructions, please see information listed at the bottom of this form.

Supplier	Elsevier Limited The Boulevard,Langford Lane Kidlington,Oxford,OX5 1GB,UK
Registered Company Number	1982084
Customer name	Michael D Jensen
Customer address	1151 Richmond Street
	London, ON N6A3K7
License number	3652710099847
License date	Jun 19, 2015
Licensed content publisher	Elsevier
Licensed content publication	International Journal of Radiation Oncology*Biology*Physics
Licensed content title	High-Resolution, Small Animal Radiation Research Platform With X-Ray Tomographic Guidance Capabilities
Licensed content author	John Wong,Elwood Armour,Peter Kazanzides,Iulian Iordachita,Erik Tryggestad,Hua Deng,Mohammad Matinfar,Christopher Kennedy,Zejian Liu,Timothy Chan,Owen Gray,Frank Verhaegen,Todd McNutt,Eric Ford,Theodore L. DeWeese
Licensed content date	1 August 2008
Licensed content volume number	71
Licensed content issue number	5
Number of pages	9
Start Page	1591
End Page	1599
Type of Use	reuse in a thesis/dissertation
Portion	figures/tables/illustrations
Number of figures/tables /illustrations	2
Format	both print and electronic
Are you the author of this Elsevier article?	No

Will you be translating?	No
Original figure numbers	figures 1,2
Title of your thesis/dissertation	Development of a small animal conformal irradiator with dual energy x-ray computed tomography imaging for kilovoltage dosimetry
Expected completion date	Sep 2015
Estimated size (number of pages)	180
Elsevier VAT number	GB 494 6272 12
Permissions price	0.00 CAD
VAT/Local Sales Tax	0.00 CAD / 0.00 GBP
Total	0.00 CAD
Terms and Conditions	

INTRODUCTION

1. The publisher for this copyrighted material is Elsevier. By clicking "accept" in connection with completing this licensing transaction, you agree that the following terms and conditions apply to this transaction (along with the Billing and Payment terms and conditions established by Copyright Clearance Center, Inc. ("CCC"), at the time that you opened your Rightslink account and that are available at any time at http://myaccount.copyright.com).

GENERAL TERMS

2. Elsevier hereby grants you permission to reproduce the aforementioned material subject to the terms and conditions indicated.

3. Acknowledgement: If any part of the material to be used (for example, figures) has appeared in our publication with credit or acknowledgement to another source, permission must also be sought from that source. If such permission is not obtained then that material may not be included in your publication/copies. Suitable acknowledgement to the source must be made, either as a footnote or in a reference list at the end of your publication, as follows:

"Reprinted from Publication title, Vol /edition number, Author(s), Title of article / title of chapter, Pages No., Copyright (Year), with permission from Elsevier [OR APPLICABLE SOCIETY COPYRIGHT OWNER]." Also Lancet special credit - "Reprinted from The Lancet, Vol. number, Author(s), Title of article, Pages No., Copyright (Year), with permission from Elsevier."

4. Reproduction of this material is confined to the purpose and/or media for which permission is hereby given.

5. Altering/Modifying Material: Not Permitted. However figures and illustrations may be altered/adapted minimally to serve your work. Any other abbreviations, additions, deletions and/or any other alterations shall be made only with prior written authorization of Elsevier

Ltd. (Please contact Elsevier at permissions@elsevier.com)

6. If the permission fee for the requested use of our material is waived in this instance, please be advised that your future requests for Elsevier materials may attract a fee.

7. Reservation of Rights: Publisher reserves all rights not specifically granted in the combination of (i) the license details provided by you and accepted in the course of this licensing transaction, (ii) these terms and conditions and (iii) CCC's Billing and Payment terms and conditions.

8. License Contingent Upon Payment: While you may exercise the rights licensed immediately upon issuance of the license at the end of the licensing process for the transaction, provided that you have disclosed complete and accurate details of your proposed use, no license is finally effective unless and until full payment is received from you (either by publisher or by CCC) as provided in CCC's Billing and Payment terms and conditions. If full payment is not received on a timely basis, then any license preliminarily granted shall be deemed automatically revoked and shall be void as if never granted. Further, in the event that you breach any of these terms and conditions or any of CCC's Billing and Payment terms and conditions, the license is automatically revoked and shall be void as if never granted. Use of materials as described in a revoked license, as well as any use of the materials beyond the scope of an unrevoked license, may constitute copyright infringement and publisher reserves the right to take any and all action to protect its copyright in the materials.

9. Warranties: Publisher makes no representations or warranties with respect to the licensed material.

10. Indemnity: You hereby indemnify and agree to hold harmless publisher and CCC, and their respective officers, directors, employees and agents, from and against any and all claims arising out of your use of the licensed material other than as specifically authorized pursuant to this license.

11. No Transfer of License: This license is personal to you and may not be sublicensed, assigned, or transferred by you to any other person without publisher's written permission.

12. No Amendment Except in Writing: This license may not be amended except in a writing signed by both parties (or, in the case of publisher, by CCC on publisher's behalf).

13. Objection to Contrary Terms: Publisher hereby objects to any terms contained in any purchase order, acknowledgment, check endorsement or other writing prepared by you, which terms are inconsistent with these terms and conditions or CCC's Billing and Payment terms and conditions. These terms and conditions, together with CCC's Billing and Payment terms and conditions (which are incorporated herein), comprise the entire agreement between you and publisher (and CCC) concerning this licensing transaction. In the event of any conflict between your obligations established by these terms and conditions and those established by CCC's Billing and Payment terms and conditions, these terms and conditions shall control.

14. Revocation: Elsevier or Copyright Clearance Center may deny the permissions described

in this License at their sole discretion, for any reason or no reason, with a full refund payable to you. Notice of such denial will be made using the contact information provided by you. Failure to receive such notice will not alter or invalidate the denial. In no event will Elsevier or Copyright Clearance Center be responsible or liable for any costs, expenses or damage incurred by you as a result of a denial of your permission request, other than a refund of the amount(s) paid by you to Elsevier and/or Copyright Clearance Center for denied permissions.

LIMITED LICENSE

The following terms and conditions apply only to specific license types:

15. **Translation**: This permission is granted for non-exclusive world **English** rights only unless your license was granted for translation rights. If you licensed translation rights you may only translate this content into the languages you requested. A professional translator must perform all translations and reproduce the content word for word preserving the integrity of the article. If this license is to re-use 1 or 2 figures then permission is granted for non-exclusive world rights in all languages.

16. **Posting licensed content on any Website**: The following terms and conditions apply as follows: Licensing material from an Elsevier journal: All content posted to the web site must maintain the copyright information line on the bottom of each image; A hyper-text must be included to the Homepage of the journal from which you are licensing at http://www.sciencedirect.com/science/journal/xxxxx or the Elsevier homepage for books at http://www.elsevier.com; Central Storage: This license does not include permission for a scanned version of the material to be stored in a central repository such as that provided by Heron/XanEdu.

Licensing material from an Elsevier book: A hyper-text link must be included to the Elsevier homepage at http://www.elsevier.com . All content posted to the web site must maintain the copyright information line on the bottom of each image.

Posting licensed content on Electronic reserve: In addition to the above the following clauses are applicable: The web site must be password-protected and made available only to bona fide students registered on a relevant course. This permission is granted for 1 year only. You may obtain a new license for future website posting.

17. **For journal authors:** the following clauses are applicable in addition to the above:

Preprints:

A preprint is an author's own write-up of research results and analysis, it has not been peer-reviewed, nor has it had any other value added to it by a publisher (such as formatting, copyright, technical enhancement etc.).

Authors can share their preprints anywhere at any time. Preprints should not be added to or enhanced in any way in order to appear more like, or to substitute for, the final versions of articles however authors can update their preprints on arXiv or RePEc with their Accepted

Author Manuscript (see below).

If accepted for publication, we encourage authors to link from the preprint to their formal publication via its DOI. Millions of researchers have access to the formal publications on ScienceDirect, and so links will help users to find, access, cite and use the best available version. Please note that Cell Press, The Lancet and some society-owned have different preprint policies. Information on these policies is available on the journal homepage.

Accepted Author Manuscripts: An accepted author manuscript is the manuscript of an article that has been accepted for publication and which typically includes author-incorporated changes suggested during submission, peer review and editor-author communications.

Authors can share their accepted author manuscript:

- immediately
    - via their non-commercial person homepage or blog
    - by updating a preprint in arXiv or RePEc with the accepted manuscript
    - via their research institute or institutional repository for internal institutional uses or as part of an invitation-only research collaboration work-group
    - directly by providing copies to their students or to research collaborators for their personal use
    - for private scholarly sharing as part of an invitation-only work group on commercial sites with which Elsevier has an agreement
- after the embargo period
    - via non-commercial hosting platforms such as their institutional repository
    - via commercial sites with which Elsevier has an agreement

In all cases accepted manuscripts should:

- link to the formal publication via its DOI
- bear a CC-BY-NC-ND license - this is easy to do
- if aggregated with other manuscripts, for example in a repository or other site, be shared in alignment with our hosting policy not be added to or enhanced in any way to appear more like, or to substitute for, the published journal article.

Published journal article (JPA): A published journal article (PJA) is the definitive final record of published research that appears or will appear in the journal and embodies all value-adding publishing activities including peer review co-ordination, copy-editing, formatting, (if relevant) pagination and online enrichment.

Policies for sharing publishing journal articles differ for subscription and gold open access articles:

Subscription Articles: If you are an author, please share a link to your article rather than the full-text. Millions of researchers have access to the formal publications on ScienceDirect, and so links will help your users to find, access, cite, and use the best available version.

Theses and dissertations which contain embedded PJAs as part of the formal submission can be posted publicly by the awarding institution with DOI links back to the formal publications on ScienceDirect.

If you are affiliated with a library that subscribes to ScienceDirect you have additional private sharing rights for others' research accessed under that agreement. This includes use for classroom teaching and internal training at the institution (including use in course packs and courseware programs), and inclusion of the article for grant funding purposes.

Gold Open Access Articles: May be shared according to the author-selected end-user license and should contain a CrossMark logo, the end user license, and a DOI link to the formal publication on ScienceDirect.

Please refer to Elsevier's posting policy for further information.

18. **For book authors** the following clauses are applicable in addition to the above: Authors are permitted to place a brief summary of their work online only. You are not allowed to download and post the published electronic version of your chapter, nor may you scan the printed edition to create an electronic version. **Posting to a repository:** Authors are permitted to post a summary of their chapter only in their institution's repository.

19. **Thesis/Dissertation**: If your license is for use in a thesis/dissertation your thesis may be submitted to your institution in either print or electronic form. Should your thesis be published commercially, please reapply for permission. These requirements include permission for the Library and Archives of Canada to supply single copies, on demand, of the complete thesis and include permission for Proquest/UMI to supply single copies, on demand, of the complete thesis. Should your thesis be published commercially, please reapply for permission. Theses and dissertations which contain embedded PJAs as part of the formal submission can be posted publicly by the awarding institution with DOI links back to the formal publications on ScienceDirect.

Elsevier Open Access Terms and Conditions

You can publish open access with Elsevier in hundreds of open access journals or in nearly 2000 established subscription journals that support open access publishing. Permitted third party re-use of these open access articles is defined by the author's choice of Creative Commons user license. See our open access license policy for more information.

Terms & Conditions applicable to all Open Access articles published with Elsevier:

Any reuse of the article must not represent the author as endorsing the adaptation of the article nor should the article be modified in such a way as to damage the author's honour or reputation. If any changes have been made, such changes must be clearly indicated.

The author(s) must be appropriately credited and we ask that you include the end user license and a DOI link to the formal publication on ScienceDirect.

If any part of the material to be used (for example, figures) has appeared in our publication with credit or acknowledgement to another source it is the responsibility of the user to ensure their reuse complies with the terms and conditions determined by the rights holder.

Additional Terms & Conditions applicable to each Creative Commons user license:

CC BY: The CC-BY license allows users to copy, to create extracts, abstracts and new works from the Article, to alter and revise the Article and to make commercial use of the Article (including reuse and/or resale of the Article by commercial entities), provided the user gives appropriate credit (with a link to the formal publication through the relevant DOI), provides a link to the license, indicates if changes were made and the licensor is not represented as endorsing the use made of the work. The full details of the license are available at http://creativecommons.org/licenses/by/4.0.

CC BY NC SA: The CC BY-NC-SA license allows users to copy, to create extracts, abstracts and new works from the Article, to alter and revise the Article, provided this is not done for commercial purposes, and that the user gives appropriate credit (with a link to the formal publication through the relevant DOI), provides a link to the license, indicates if changes were made and the licensor is not represented as endorsing the use made of the work. Further, any new works must be made available on the same conditions. The full details of the license are available at http://creativecommons.org/licenses/by-nc-sa/4.0.

CC BY NC ND: The CC BY-NC-ND license allows users to copy and distribute the Article, provided this is not done for commercial purposes and further does not permit distribution of the Article if it is changed or edited in any way, and provided the user gives appropriate credit (with a link to the formal publication through the relevant DOI), provides a link to the license, and that the licensor is not represented as endorsing the use made of the work. The full details of the license are available at http://creativecommons.org/licenses/by-nc-nd/4.0. Any commercial reuse of Open Access articles published with a CC BY NC SA or CC BY NC ND license requires permission from Elsevier and will be subject to a fee.

Commercial reuse includes:

- Associating advertising with the full text of the Article
- Charging fees for document delivery or access
- Article aggregation
- Systematic distribution via e-mail lists or share buttons

Posting or linking by commercial companies for use by customers of those companies.

20. **Other Conditions**:

v1.7

Questions? customercare@copyright.com or +1-855-239-3415 (toll free in the US) or +1-978-646-2777.

From: Zora Catterick [redacted] on behalf of Permissions <permissions@iop.org>
Sent: June-22-15 9:24 AM
To: [redacted]
Subject: Re: PLS Clear Permission Request - [757] PHYSICS IN MEDICINE & BIOLOGY (00319155)

Dear Michael Jensen,

Thank you for your request to reproduce IOP Publishing material in your thesis.

Regarding:

Figure 1 (Phys. Med. Biol. 54 (2009) 3727–3740)

We are happy to grant permission for the use you request on the terms set out below.

Conditions

Non-exclusive, non-transferrable, revocable, worldwide, permission to use the material in print and electronic form will be granted **subject to the following conditions:**

- Permission will be cancelled without notice if you fail to fulfil any of the conditions of this letter.

- You will make reasonable efforts to contact the author(s) to seek consent for your intended use. Contacting one author acting expressly as authorised agent for their co-authors is acceptable.

- You will reproduce the following prominently alongside the material:

  - the source of the material, including author, article title, title of journal, volume number, issue number (if relevant), page range (or first page if this is the only information available) and date of first publication. This information can be contained in a footnote or reference note; or

  - a link back to the article (via DOI); and

  - if practical and IN ALL CASES for works published under any of the Creative Commons licences the words "© Institute of Physics and Engineering in Medicine. Reproduced by permission of IOP Publishing. All rights reserved."

- The material will not, without the express permission of the author(s), be used in any way which, in the opinion of IOP Publishing, could distort or alter the author(s)' original intention(s) and meaning, be prejudicial to the honour or reputation of the author(s) and/or imply endorsement by the author(s) and/or IOP Publishing.

- Payment of £0 is received in full by IOP Publishing prior to use.

Special Conditions – For STM Signatories ONLY (as agreed as part of the STM Guidelines)

Any permissions granted for a particular edition will apply also to subsequent editions and for editions in other languages, provided such editions are for the work as a whole in situ and does not involve the separate exploitation of the permitted illustrations or excerpts.

If you have any questions, please feel free to contact our Permissions team at permissions@iop.org.

I should be grateful if you would acknowledge receipt of this email.

Kind regards,

Zora Catterick

Publishing Assistant

IOP Publishing

Please note: We do not usually provide signed permission forms as a separate attachment. Please print this email and provide it to your publisher as proof of permission.

From: [redacted]
To:
Cc:
Date: 19/06/2015 22:36
Subject: PLS Clear Permission Request - [757] PHYSICS IN MEDICINE & BIOLOGY (00319155)

Here is a permissions request for you. It has been generated by PLSclear, the Publishers Licensing Society's new permissions tool.

The tool ensures that

- you only receive requests for content you own, and that the requests go to the right people in your company
- you receive all the necessary information to grant requests (PLSclear uses a questionnaire that has been developed by some of the UK's leading rights specialists).

We hope this saves you time and makes managing the process easier.

If this is not one of your titles, you cannot grant permission or perhaps we have emailed the wrong contact, then please click the following link and tell us so that we can update our records: [Unable to process this request]

I am applying for permission for:

PHYSICS IN MEDICINE & BIOLOGY (00319155)	
A **illustration** extract	
content source:	**Online**
issue date:	**28/05/2009**
issue number:	**54**
issue URL:	**http://iopscience.iop.org/0031-9155/54/12/008/**
article title:	**Commissioning of a novel microCT/RT system for small animal conformal radiotherapy**
figure number & title / caption:	**Figure 1. The variable-aperture collimator in the microCT/RT system uses two disks with hexag dodecagonal shape**
position on page:	**top**
reproduction colour:	**Full Colour**

reproduction size:	**Half page**
positioning:	**inside or later pages**

To be used in:

A **Book, Journal, Magazine or Academic Paper...**	
The **Thesis** details are	
type of document:	**Doctoral Thesis**
publication title:	**Development of a small animal conformal irradiator with dual energy x-ray computed tomography imaging for kilovoltage dosimetry**
number of pages:	**180**
estimated publication date:	**Sept 2015**
other relevant Information:	**I am a University of Western Ontario graduate student completing my Doctoral thesis. My thesis will be available in full-text on the internet for reference, study and / or copy. Except in situations where a thesis is under embargo or restriction, the electronic version will be accessible through the Western Libraries web pages, the Library's web catalogue, and also through web search engines. I will also be granting Library and Archives Canada and ProQuest/UMI a non-exclusive license to reproduce, loan, distribute, or sell single copies of my thesis by any means and in any form or format. These rights will in no way restrict republication of the material in any other form by you or by others authorized by you. The material will be attributed through a citation including the DOI.**

Please respond directly to the person making the request. They have not received your company name or contact details.

Contact details are

Name:	**Michael Jensen**
Email:	[redacted]
Address:	**1151 Richmond Street N**
Town /City:	**London, Ontario, Canada**
Post Code:	**N6A 3K7**

Help us improve PLSclear: 5 quick questions

This email (and attachments) are confidential and intended for the addressee(s) only. If you are not the intended recipient please notify the sender, delete any copies and do not take action in reliance on it. Any views expressed are the author's and do not represent those of IOP, except where specifically stated. IOP takes reasonable precautions to protect against viruses but accepts no responsibility for loss or damage arising from virus infection. For the protection of IOP's systems and staff emails are scanned automatically.

IOP Publishing Limited Registered in England under Registration No 467514. Registered Office: Temple Circus, Bristol BS1 6HG England Vat No GB 461 6000 84.

Please consider the environment before printing this email

American Association of Physicists in Medicine
One Physics Ellipse
College Park, MD 20740-3846
(301) 209-3350
Fax (301) 209-0862
http://www.aapm.org

Office of the Executive Director
Angela R. Keyser
Phone: [redacted]
E-mail:

DATE OF REQUEST: 06/19/15

FROM:

Michael D. Jensen, PhD Candidate, Department of Medical Biophysics, Schulich School of Medicine & Dentistry, Western University, 1151 Richmond Street, London, Ontario, Canada, N6A 3K7

EMAIL ADDRESS: [redacted]

1. **Permission is granted to:**

   Figure 1. "Pictures of the micro-IGRT (X-Rad 225Cx) unit" from "Characterization of image quality and image-guidance performance of a preclinical microirradiator," by R. Clarkson, P. E. Lindsay, S. Ansell, G. Wilson, S. Jelveh, R. P. Hill and D. A. Jaffray. Med. Phys. 38(2) 845-856 (2011).

2. **Permission is requested to use the following material:**

   Michael D. Jensen

3. **For what purpose:**

   To include the figure in my thesis.

Authors seeking permission must also notify the first author of the article from which permission is being sought.

Permission is hereby granted: [redacted] June 24, 2015

Signature **Date**

Appendix E

Animal Ethics Approval

This thesis contains small animal experimental data. The ethics approval of the Animal Use Protocols (AUP) is provided in this appendix.

Western

AUP Number: 2012-039
PI Name: Wong, Eugene
AUP Title: A Pilot Study Of Targeted Irradiation In Rats
Approval Date: 03/28/2013

Official Notice of Animal Use Subcommittee (AUS) Approval: Your new Animal Use Protocol (AUP) entitled "A Pilot Study Of Targeted Irradiation In Rats" has been APPROVED by the Animal Use Subcommittee of the University Council on Animal Care. This approval, although valid for four years, and is subject to annual Protocol Renewal.2012-039::1

1. This AUP number must be indicated when ordering animals for this project.
2. Animals for other projects may not be ordered under this AUP number.
3. Purchases of animals other than through this system must be cleared through the ACVS office. Health certificates will be required.

The holder of this Animal Use Protocol is responsible to ensure that all associated safety components (biosafety, radiation safety, general laboratory safety) comply with institutional safety standards and have received all necessary approvals. Please consult directly with your institutional safety officers.

Submitted by: Copeman, Laura
on behalf of the Animal Use Subcommittee
University Council on Animal Care

Western

2009-080::5:

AUP Number: 2009-080
AUP Title: Non-Invasive Imaging of Metastasis: Detection, Monitoring and Intervention

Yearly Renewal Date: 11/01/2014

The YEARLY RENEWAL to Animal Use Protocol (AUP) 2009-080 has been approved, and will be approved for one year following the above review date.

1. This AUP number must be indicated when ordering animals for this project.
2. Animals for other projects may not be ordered under this AUP number.
3. Purchases of animals other than through this system must be cleared through the ACVS office. Health certificates will be required.

REQUIREMENTS/COMMENTS
Please ensure that individual(s) performing procedures on live animals, as described in this protocol, are familiar with the contents of this document.

The holder of this Animal Use Protocol is responsible to ensure that all associated safety components (biosafety, radiation safety, general laboratory safety) comply with institutional safety standards and have received all necessary approvals. Please consult directly with your institutional safety officers.

Submitted by: Kinchlea, Will D
on behalf of the Animal Use Subcommittee

Curriculum Vitae

Name:	Michael David Jensen
Post-Secondary Education and Degrees:	The University of Western Ontario London, ON 2008 B.Sc.
	The University of Western Ontario London, ON 2008–2015 Ph.D.
Honours and Awards:	Ontario Graduate Scholarship in Science and Technology 2010–2011
	Canadian Institute of Health Research Student Training Program (CIHR-STP) M.Sc. Award 2009–2010
	Schulich Graduate Scholarship 2008–2013
Related Work Experience:	Research Assistant The University of Western Ontario 2008–2015

Publications:

[1]G. Santyr, M. Fox, K. Thind, E. Hegarty, A. Ouriadov, M. Jensen, T. J. Scholl, J. Van Dyk, and E. Wong, "Anatomical, functional and metabolic imaging of radiation-induced lung injury using hyperpolarized MRI", NMR Biomed. **27**, 1515–24 (2014).

[2]K. Thind, M. D. Jensen, E. Hegarty, A. P. Chen, H. Lim, F. Martinez-Santiesteban, J. Van Dyk, E. Wong, T. J. Scholl, and G. E. Santyr, "Mapping metabolic changes associated with early Radiation Induced Lung Injury post conformal radiotherapy using hyperpolar-

ized (13)C-pyruvate Magnetic Resonance Spectroscopic Imaging", Radiother. Oncol. **110**, 317–322 (2014).

[3]M. D. Jensen, W. T. Hrinivich, J. A. Jung, D. W. Holdsworth, M. Drangova, J. Chen, and E. Wong, "Implementation and commissioning of an integrated micro-CT/RT system with computerized independent jaw collimation", Med. Phys. **40**, 081706 (2013).

[4]M. D. Jensen, A. Abdellatif, J. Chen, and E. Wong, "Study of the IMRT interplay effect using a 4DCT Monte Carlo dose calculation", Phys. Med. Biol. **57**, N89–99 (2012).

[5]A. Abdellatif, J. Craig, M. Jensen, M. Mulligan, H. Mosalaei, G. Bauman, J. Chen, and E. Wong, "Experimental assessments of intrafractional prostate motion on sequential and simultaneous boost to a dominant intraprostatic lesion", Med. Phys. **39**, 1505–17 (2012).

[6]M. Oliver, M. Jensen, J. Chen, and E. Wong, "Evaluation of optimization strategies and the effect of initial conditions on IMAT optimization using a leaf position optimization algorithm", Phys. Med. Biol. **54**, 3543–61 (2009).